

**EXPERIMENTAL INVESTIGATION AND CONSTITUTIVE
MODELING OF RANDOMLY ORIENTED ELECTROSPUN
NANOFIBROUS MEMBRANES**

WONG DANNEE

**FACULTY OF ENGINEERING
UNIVERSITY OF MALAYA
KUALA LUMPUR**

2018

**EXPERIMENTAL INVESTIGATION AND CONSTITUTIVE
MODELING OF RANDOMLY ORIENTED ELECTROSPUN
NANOFIBROUS MEMBRANES**

WONG DANNEE

**THESIS SUBMITTED IN FULFILMENT
OF THE REQUIREMENTS
FOR THE DEGREE OF DOCTOR OF PHILOSOPHY**

**FACULTY OF ENGINEERING
UNIVERSITY OF MALAYA
KUALA LUMPUR**

2018

UNIVERSITI MALAYA

ORIGINAL LITERARY WORK DECLARATION

Name of Candidate: Wong Dannee

Registration/Matrix No.: KHA140103

Name of Degree: The Degree of Doctor of Philosophy

Title of Project Paper/Research Report/Dissertation/Thesis ("this Work"): Experimental investigation and constitutive modeling of randomly oriented electrospun nanofibrous membranes

Field of Study: Materials Engineering

I do solemnly and sincerely declare that:

- (1) I am the sole author/writer of this Work;
- (2) This work is original;
- (3) Any use of any work in which copyright exists was done by way of fair dealing and for permitted purposes and any excerpt or extract from, or reference to or reproduction of any copyright work has been disclosed expressly and sufficiently and the title of the Work and its authorship have been acknowledged in this Work;
- (4) I do not have any actual knowledge nor do I ought reasonably to know that the making of this work constitutes an infringement of any copyright work;
- (5) I hereby assign all and every rights in the copyright to this Work to the University of Malaya ("UM"), who henceforth shall be owner of the copyright in this Work and that any reproduction or use in any form or by any means whatsoever is prohibited without the written consent of UM having been first had and obtained;
- (6) I am fully aware that if in the course of making this Work I have infringed any copyright whether intentionally or otherwise, I may be subject to legal action or any other action as may be determined by UM.

Candidate's Signature

Date

Subscribed and solemnly declared before,

Witness's Signature

Date

Name:

Designation:

EXPERIMENTAL INVESTIGATION AND CONSTITUTIVE MODELING OF RANDOMLY ORIENTED ELECTROSPUN NANOFIBROUS MEMBRANES

ABSTRACT

The recent advancement of nanotechnology has enabled the fabrication of nanofibers through a number of processing techniques. Among these, electrospinning offers a unique ability to produce nanofibrous membranes for different materials and of different assemblies or textures that make them suitable for various applications including filtration, tissue engineering, nanocomposites and textiles. In these applications, electrospun nanofibrous membranes are frequently subjected to complex stresses and strains which could lead to fiber failures. Therefore, the understanding of their mechanical properties becomes crucial in order to facilitate the design and performance evaluation of the materials. In view of probing the mechanical response of nanofibrous membranes, relevant experimental characterizations are conducted such as atomic force microscopy (AFM), nanoindentation, nanotensile tests or conventional tensile tests. These experimental techniques are often daunting, costly and time-consuming. If a robust and cost-effective alternative method in evaluating the mechanical properties of electrospun nanofibrous materials through numerical simulation can be established, the strong dependence on experimental works can therefore be significantly reduced. The present thesis focuses on the development of a simple constitutive model with reduced number of material parameters for the mechanical response of randomly oriented electrospun PVDF nanofibrous membranes. To this end, the thesis is divided into two parts. The first part focuses on the experimental aspects that include the fabrication of electrospun nanofibrous membranes using different sets of electrospinning parameters and the characterization of their surface morphology. Subsequently, samples obtained using the optimum set of parameters are chosen for further characterizations, i.e. physical evaluation of undeformed and deformed membranes, mechanical testing and fiber

orientation analysis. Three types of uniaxial mechanical tests are conducted: monotonic tensile tests, cyclic loading tests with increasing maximum strain and cyclic-relaxation tests. Results show that the material exhibits complex mechanical responses, which include finite strain, irreversible deformation, hysteresis and time-dependent response. Furthermore, fiber orientation analysis suggests that the material is initially isotropic in the plane (transversely isotropic) and the deformation-induced fiber re-orientation takes place. The second part of the thesis deals with the development of a constitutive model capturing the observed responses. Motivated by the experimental observation, the model development starts from the description of material response at fiber-scale in order to describe individual fiber response and irreversible inter-fiber interactions using hyperelastic and large strain elasto-plastic frameworks respectively. The macroscopic response of the membranes is subsequently obtained by integrating the fiber responses in all possible fiber orientations. The efficiency of the proposed model is assessed using experimental data. It is found that the model is qualitatively in good agreement with uniaxial monotonic and cyclic tensile loading tests. Two other deformation modes, i.e. equibiaxial extension and pure shear (planar extension) are simulated to further evaluate the model responses.

Keywords: Constitutive modeling, nanofiber, membrane, mechanical response, electros-
pinning

**PENYIASATAN EXPERIMEN DAN PEMODELAN KONSTITUTIF MEMBRAN
NANOFIBER DARI ELEKTROSPINNING YANG BERORIENTASI SECARA**

RAWAK

ABSTRAK

Kemajuan nanoteknologi kebelakangan ini membolehkan fabrikasi nanofiber melalui beberapa teknik pemrosesan. Di antara ini, elektrospinning menawarkan keupayaan unik untuk menghasilkan nanofiber membran daripada bahan-bahan yang berbeza dan perhimpunan atau tekstur yang berbeza yang menjadikannya sesuai untuk pelbagai aplikasi termasuk penapisan, kejuruteraan tisu, nanokomposit dan tekstil. Dalam semua aplikasi ini, membran nanofiber sering terdedah kepada tekanan dan ketegangan yang kompleks yang mungkin menyebabkan kegagalan serat. Oleh itu, pemahaman tentang sifat mekanikal membrane nanofiber adalah penting untuk memudahkan penilaian reka bentuk dan prestasi bahan. Untuk meninjau tindak balas mekanikal membran nanofiber, pengajian eksperimen yang berkaitan perlu dijalankan seperti mikroskop berkuat-kuasa atom, nanoindentasi, ujian nanotensile atau ujian tegangan konvensional. Teknik-teknik eksperimen ini selalunya kompleks, mahal dan memerlukan masa. Sekiranya kaedah alternatif yang teguh dan kos efektif dalam menilai sifat-sifat mekanik membran nanofiber melalui simulasi boleh ditubuhkan, kebergantungan terhadap eksperimen boleh dikurangkan dengan ketara. Tesis ini memberi tumpuan kepada penubuhan sebuah model konstitutif ringkas dengan mengurangkan bilangan parameter bahan untuk menyiasat tindak balas mekanikal membran nanofiber PVDF berorientasi secara rawak. Untuk tujuan ini, tesis ini dibahagikan kepada dua bahagian. Bahagian pertama memberi tumpuan kepada eksperimen-eksperimen yang merangkumi fabrikasi membran nanofiber dengan menggunakan set parameter elektrospinning yang berbeza dan juga pencirian morfologi permukaan bahan tersebut. Selepas itu, sampel yang dihasil

menggunakan set parameter optimum dipilih untuk pengkajian lanjut, iaitu penilaian fizikal membran sebelum dan selepas deformasi, ujian mekanikal dan analisis orientasi serat. Tiga jenis ujian mekanikal uniaxial dijalankan: ujian tegangan monotonik, ujian kitaran dengan peningkatan ketegangan maksimum dan ujian kitaran dengan relaksasi. Keputusan menunjukkan bahawa bahan mempamerkan tindak balas mekanikal yang kompleks, yang merangkumi ketegangan terhad, ubah bentuk tidak dapat dipulihkan, histeresis dan tindak balas yang bergantung kepada masa. Tambahan pula, analisis orientasi menunjukkan bahawa bahan adalah isotropik melintang pada permulaan dan reorientasi serat berlaku disebabkan oleh deformasi. Bahagian kedua tesis berkenaan dengan perkembangan model konstitutif yang meramal tindak balas membrane nanofiber yang diperhatikan dalam eksperimen. Daripada pemerhatian eksperimen, penubuhan model bermula dari penerangan tindak balas bahan pada skala serat untuk menggambarkan tindak balas serat individu dan interaksi antara serat yang tidak dapat dipulihkan dengan menggunakan rangka hiperelastik dan elasto-plastik ketegangan besar. Kemudian, tindak balas makroskopik membran diperolehi dengan mengintegrasikan tindak balas serat dalam semua orientasi serat yang berkemungkinan. Keberkesanan model tersebut dinilai dengan menggunakan data eksperimen. Adalah didapati bahawa model tersebut menunjukkan persetujuan yang baik secara kualitatif dengan ujian tegangan monotonik dan juga ujian kitaran dengan peningkatan ketegangan maksimum. Dua mod deformasi lain, iaitu lanjutan equibiaxial dan lanjutan pelan disimulasikan untuk menilai model tersebut dengan lebih mendalam.

Kata kunci: Model konstitutif, nanofiber, membran, tindak balas mekanikal, elektrospinning

ACKNOWLEDGEMENTS

Firstly, I would like to express the deepest appreciation to the Mechanical Department of Faculty of Engineering, University of Malaya for giving me the opportunity to conduct this project as a Ph.D. candidate in Materials Engineering. Next, I would like to thank my project supervisors, Assoc. Prof. Dr. Andri Andriyana and Assoc. Prof. Ir. Dr. Ang Bee Chin for their assisting with guidance, dedication, patience and continuous support throughout the project.

Besides, a sincere gratitude dedicated to Prof. Erwan Verron from Ecole Centrale de Nantes, France for his help and guidance on the constitutive modeling parts of the research works throughout my stay of eight months in Nantes, France.

Furthermore, a special thanks for my seniors, Dr. Ch'ng Shiau Ying and Dr. Loo Mei Sze for their helps and guidance in this project. In addition, I would also like to acknowledge with much appreciation the help from my colleague, Jacky Lee Jia Li for his kindness on information sharing and the method to deal with problems.

Lastly, many thanks to my family, colleagues and seniors who have helped by giving comments, suggestions and information about the ways to deal with different problems in this period.

TABLE OF CONTENTS

ORIGINAL LITERARY WORK DECLARATION	ii
ABSTRACT	iii
ABSTRAK	v
ACKNOWLEDGEMENTS	vii
TABLE OF CONTENTS	viii
LIST OF FIGURES	xi
LIST OF TABLES	xiv
LIST OF SYMBOLS AND ABBREVIATIONS	xv
CHAPTER 1: INTRODUCTION	1
1.1 Background and problem statement	1
1.2 Research objectives	3
1.3 Significance of research	4
1.4 Scope of work	4
1.5 Thesis organization	5
CHAPTER 2: LITERATURE REVIEW	6
2.1 Generality on polymer	6
2.2 Electrospinning	9
2.2.1 Introduction of electrospinning	9
2.2.2 Electrospinning theory	11
2.2.3 Effects of electrospinning parameters	14
2.2.3.1 Effects of polymer concentration	16
2.2.3.2 Effects of solvent selection	18
2.2.3.3 Effects of solution conductivity	20
2.2.3.4 Effects of applied voltage	20
2.2.3.5 Effects of feed rate	21
2.2.3.6 Effects of capillary-collector distance	22
2.2.3.7 Effects of ambient	23
2.3 Mechanical properties of electrospun nanofibrous membranes	24
2.3.1 Factors affecting the mechanical properties	24
2.3.2 Mechanical characterization of single electrospun fiber	27
2.3.3 Mechanical characterization of electrospun nanofibrous membranes	31
2.3.4 Poisson's ratio characterization	35
2.4 Constitutive modeling of electrospun nanofibrous membranes	37
2.4.1 Micromechanical model	39
2.4.2 Phenomenological model	41
2.4.3 Statistical model	45
2.4.4 Modeling software	46

2.5	Potential applications of electrospun nanofibrous membranes	47
2.6	Polyvinylidene fluoride (PVDF)	52
2.6.1	Introduction of PVDF	52
2.6.2	Electrospinning of PVDF	53
2.6.3	Mechanical characterization of electrospun PVDF membranes	55
2.6.4	Potential applications of electrospun PVDF nanofibrous membranes	57
2.7	Summary of literature review	59
CHAPTER 3: METHODOLOGY		60
3.1	Fabrication of PVDF membranes	60
3.1.1	Materials	61
3.1.2	Electrospinning machine	61
3.1.3	Preparation of PVDF polymer solution	62
3.1.4	Electrospinning of PVDF nanofibrous membranes	64
3.2	Characterization of electrospun PVDF nanofibrous membranes	66
3.2.1	Surface morphology analysis	66
3.2.2	Physical evaluation of undeformed and deformed membranes	68
3.2.2.1	Comparison of fiber diameter	68
3.2.2.2	Measurement of porosity	69
3.2.3	Mechanical characterization	70
3.2.3.1	Sample preparation for mechanical characterization	71
3.2.3.2	Monotonic tensile test	72
3.2.3.3	Cyclic loading test with increasing maximum strain	73
3.2.3.4	Cyclic-relaxation test	75
3.2.4	Investigation on volume change and Poisson's ratio	78
3.2.5	Fiber orientation analysis	81
3.3	Constitutive modeling	84
3.3.1	Characteristics of structures	84
3.3.2	Description of deformation and stress-strain response	85
CHAPTER 4: EXPERIMENTAL RESULTS AND DISCUSSION		90
4.1	Surface morphology analysis	90
4.1.1	Effects of applied voltage	93
4.1.2	Effects of polymer concentration	94
4.1.3	Choice of samples for mechanical characterization	96
4.2	Physical evaluation on undeformed and deformed membranes	97
4.2.1	Comparison of fiber diameter	97
4.2.2	Measurement of porosity	98
4.3	Mechanical testing	98
4.3.1	Monotonic tensile test	99
4.3.2	Cyclic loading test with increasing maximum strain	102
4.3.3	Cyclic-relaxation test	107
4.4	Volume change of electrospun PVDF membranes	109
4.5	Poisson's ratio of electrospun PVDF membranes	113
4.5.1	In-plane Poisson's ratio	114
4.5.2	Out-of-plane Poisson's ratio	115
4.6	Fiber orientation analysis	117

CHAPTER 5: MODELING RESULTS AND DISCUSSION	122
5.1 Derivation of the stress in fibers	122
5.2 Form of material functions	125
5.3 Special case of uniaxial extension of 2D membrane	129
5.4 Parametric studies	131
5.4.1 Elasticity (Branch A)	132
5.4.2 Elasto-plasticity (Branch B)	134
5.4.3 Macroscopic parameter, k	137
5.5 Influence of fiber orientation	138
5.6 Influence of number of integration points	139
5.7 Identification of material parameters	141
5.8 Simulation of other deformation modes	147
5.8.1 Equibiaxial extension	148
5.8.2 Pure shear	149
5.8.3 Effect of biaxiality	150
CHAPTER 6: CONCLUSION AND FUTURE WORKS	154
6.1 Conclusion	154
6.2 Suggestions for future works	156
REFERENCES	158
LIST OF PUBLICATIONS AND PAPERS PRESENTED	166

LIST OF FIGURES

Figure 2.1: Linear, branched and crosslinked polymers (Callister & Rethwisch, 2011).	7
Figure 2.2: Illustration of electrospinning setup. (Retrieved August 4, 2017, from http://ppl.ippt.gov.pl/18-few-words-about/17-electrospinning)	11
Figure 2.3: Formation of Taylor cone in electrospinning process (Kodolov et al., 2014).	12
Figure 2.4: Instabilities in the jet: (a) Rayleigh instability, (b) bending instability and (c) whipping instability (Kodolov et al., 2014).	13
Figure 2.5: Summary of electrospinning process.	15
Figure 2.6: Classification of electrospinning parameters.	15
Figure 2.7: Monomer of poly(vinylidene fluoride) (Retrieved January 2, 2018, from https://en.wikipedia.org/wiki/Polyvinylidene_fluoride)	52
Figure 3.1: Research methodology flowchart.	61
Figure 3.2: An electrospinning setup.	62
Figure 3.3: Schematic diagram of the electrospun PVDF nanofibrous membrane and dimension of the specimen	72
Figure 3.4: (a) Images and (b) schematic illustration of the gripping of specimen on tensile testing machine. Front view (left) and side view (right).	74
Figure 3.5: Loading profile for cyclic loading test with increasing maximum strain.	76
Figure 3.6: Loading profile for cyclic-relaxation test.	77
Figure 3.7: (a) Dimensions and axes of specimen, (b) illustration of specimen's measuring locations and gripping areas.	80
Figure 3.8: (a) Loading sequence for fiber orientation analysis and (b) illustration of deformation-induced fiber re-orientation.	83
Figure 3.9: Schematic illustration of electrospun nanofibrous membrane and orientation of a single fiber characterized by unit vector \mathbf{N} in the reference configuration.	86
Figure 4.1: SEM micrographs of electrospun PVDF membranes with different processing voltages. Polymer concentration: 13 wt.%. Original magnification: 1000 × (left) and 5000 × (right). (a) 10 kV, (b) 15 kV, (c) 20 kV.	91
Figure 4.2: SEM micrographs of electrospun PVDF membranes with different processing voltages. Polymer concentration: 15 wt.%. Original magnification: 1000 × (left) and 5000 × (right). (a) 10 kV, (b) 15 kV, (c) 20 kV.	92
Figure 4.3: Relationship between applied voltage and average fiber diameter, for 13 wt.% and 15 wt.% polymer concentrations.	95
Figure 4.4: Force-displacement curves for monotonic tensile tests.	100
Figure 4.5: Stress-strain curves for monotonic tensile tests (a) Original scale and (b) enlarged scale.	101
Figure 4.6: Stress-strain curve for cyclic loading test.	102
Figure 4.7: Stress-strain curve for cyclic loading test indicating inelastic strain and Young's modulus for each cycle.	103
Figure 4.8: Plot of inelastic strain ratio and Young's modulus ratio versus maximum nominal strain.	104
Figure 4.9: Cyclic loading stress-strain curve indicating the yield limit for each cycle.	106

Figure 4.10: Plot of inelastic flow stress versus inelastic strain.	106
Figure 4.11: Stress-strain curve for cyclic-relaxation test.	107
Figure 4.12: Buckling of specimens at the end of cyclic-relaxation tests.	108
Figure 4.13: Evolution of stress as a function of relaxation duration during the relaxation test.	109
Figure 4.14: Normalized stress as a function of relaxation duration during relaxation tests.	110
Figure 4.15: Plots of average volume ratio versus nominal strain for (a) PVDF10, (b) PVDF15 and (c) PVDF20.	111
Figure 4.16: Determination of the in-plane Poisson's ratio for electrospun (a) PVDF10, (b) PVDF15 and (c) PVDF20 samples.	114
Figure 4.17: Determination of the out-of-plane Poisson's ratio for electrospun (a) PVDF10, (b) PVDF15 and (c) PVDF20 samples.	116
Figure 4.18: Example of SEM images of different maximum strain levels subjected to fiber orientation analysis.	119
Figure 4.19: Fiber orientation distribution \pm standard error of mean for different applied maximum strain values.	120
Figure 4.20: Fiber orientation distribution curves for different applied maximum strain values.	120
Figure 4.21: Evolution of the component of fiber orientation tensor along tensile direction (A_{11}) as a function of inelastic strain.	121
Figure 5.1: Schematic illustration of the rheological model for interacting fibers.	123
Figure 5.2: Overview for the computation of mechanical response by using MATLAB software.	132
Figure 5.3: Loading profile for the simulation of one cycle, from $\lambda = 1$ to $\lambda = 1.05$.	134
Figure 5.4: Influence of the material parameters (a) K_f and (b) a on fiber stress at branch A.	135
Figure 5.5: Influence of the material parameters (a) E_f , (b) σ_f^y and (c) H_f on fiber stress at branch B.	136
Figure 5.6: Influence of material parameter k .	137
Figure 5.7: Fiber stretch, λ_f as a function of macroscopic stretch, λ for seven fiber orientations, i.e. 0° , 15° , 30° , 45° , 60° , 75° and 90° .	140
Figure 5.8: Micromechanical response in different orientations for the elastic behavior (Branch A).	140
Figure 5.9: Micromechanical response in different orientations for the inelastic behavior (Branch B).	141
Figure 5.10: Influence of number of integration points on the macroscopic stress-stretch curve: (a) 5 points, (b) 10 points, (c) 20 points and (d) 50 points.	142
Figure 5.11: Comparison of model prediction with experimental results of cyclic loading test with increasing maximum strain.	143
Figure 5.12: Comparison of model prediction with experimental results of uniaxial monotonic loading test.	144
Figure 5.13: Comparison of model prediction with experimental results of Young's modulus ratio.	145
Figure 5.14: Comparison of model prediction with experimental result of fiber orientation tensor along tensile direction, A_{11} .	147
Figure 5.15: Simulation of (a) monotonic and (b) cyclic loading with increasing maximum stretch for equibiaxial extension.	149

Figure 5.16: Simulation of (a) monotonic and (b) cyclic loading with increasing maximum stretch for planar extension.	151
Figure 5.17: (a) Effect of biaxiality at three different global stretch values ($\lambda = 1.1$, $\lambda = 1.2$ and $\lambda = 1.3$) and (b) evolution of orientation index with deformation.	152

University of Malaya

LIST OF TABLES

Table 2.1: Challenges faced and possible solutions for the mechanical characterization of single nanofibers.	28
Table 2.2: Summary on the testing methods for single fibers and electrospun structures.	34
Table 2.3: Summary on the modeling approaches for electrospun structures.	47
Table 3.1: Amount of PVDF, DMF and acetone used for the preparation of 13 wt.% and 15 wt.% PVDF polymer solution.	64
Table 3.2: Six samples of electrospun PVDF membranes with their corresponding parameters.	65
Table 4.1: Average fiber diameter and amount of beads for electrospun PVDF membranes.	93
Table 4.2: Average fiber diameter and pore diameter of undeformed and deformed conditions for P ₁₅ V ₂₀ sample.	98
Table 4.3: Mechanical properties of electrospun PVDF membrane.	100
Table 4.4: Inelastic deformation, inelastic strain ratio, Young's modulus and Young's modulus ratio corresponded to the maximum strains.	104
Table 4.5: Inelastic deformation, yield strength and inelastic flow stress.	105
Table 4.6: Initial thickness of three electrospun PVDF samples.	110
Table 4.7: Poisson's ratio of electrospun PVDF membranes, for three different membrane thicknesses.	117
Table 5.1: Summary of the material parameters at fiber scale.	129
Table 5.2: Values of material parameters used for simulation.	133
Table 5.3: Material parameters involved in the computation of macroscopic stress-stretch response of randomly oriented electrospun PVDF nanofibrous membrane.	143
Table 5.4: Young's modulus and Young's modulus ratio of simulated cyclic loading curve corresponded to the maximum strains.	145

LIST OF SYMBOLS AND ABBREVIATIONS

AFM	Atomic force microscope
PVDF	polyvinylidene fluoride
2D	two-dimensional
SEM	Scanning electron microscope
DMF	N,N-dimethylformamide
PS	polystyrene
PE	polyethylene
PVC	polyvinyl chloride
PP	polypropylene
ABS	acrylonitrile butadiene styrene
PC	polycarbonate
DCM	dichloromethane
DMAc	dimethylacetamide
NaCl	sodium chloride
PEO	polyethylene oxide
PCL	polycaprolactone
PLCL	poly(L-lactide-co- ϵ -caprolactone)
PLLA	poly(L-lactic) acid
PA 6(3)T	poly(trimethyl hexamethylene terephthalamide)
PSU	polysulfone
RVE	Representative volume element
PBT	poly(butylene terephthalate)
PA	polyamide
PEUUR	poly(esterurethane-urea)
FBC	fiber bundle cells
ECM	extracellular matrix
DCMD	direct contact membrane distillation
kV	kilovolts
wt %	weight percentage
DC	direct current
mA	milliampere
$^{\circ}\text{C}$	degree celsius
rpm	revolutions per minute
λ	macroscopic stretch
ϵ_i	maximum applied strain
ϵ_{in}	inelastic strain
A_0	fiber orientation tensor
A_{11}	fiber orientation tensor along stretching direction
ρ	normalized orientation distribution function
\mathbf{a}_0	referential orientation
ϵ_{max}	maximum strain
ϵ_p	inelastic strain
E	Young's modulus
E_o	initial Young's modulus
E_i	current Young's modulus
σ_y	yield strength
σ_{y_o}	initial yield strength
σ_{y_i}	current yield strength

V	volume
V_o	initial volume
W	strain energy function per unit volume in reference configuration
w	strain energy at fiber scale
$\Psi(\theta)$	probability distribution function
θ	orientation
λ_f^θ	fiber stretch
l	current fiber length
l_o	initial fiber length
\mathbf{F}	deformation gradient tensor
\mathbf{N}^θ	unit vector in reference configuration
\mathbf{P}	first Piola-Kirchhoff stress tensor
s_f^θ	nominal fiber stress
σ_f^θ	true fiber stress
β	orientation index
$\lambda_{f,e}^\theta$	elastic fiber stretch
$\lambda_{f,i}^\theta$	inelastic fiber stretch
K_f	fiber stiffness
a	shape control constant
σ_f^y	yield limit
E_f	material parameter akin to elastic modulus
H_f	material parameter akin to hardening modulus
k	in-plane Poisson's ratio
α	accumulated inelastic deformation
f	yield function
γ	consistency parameter
F	axial force
A_o	initial cross-section
B	biaxiality constant

CHAPTER 1: INTRODUCTION

1.1 Background and problem statement

Nowadays, the world is moving towards the trend of nanotechnology that involves the design and production of very small objects or artefacts, on the scale of 100 nm or less. This size is approximately 10,000 times smaller than the width of a human hair. In fact, nanomaterials are one of the main products of nanotechnology, which include nano-scale particles, fibers, tubes or rods. When bulk materials are reduced to the nano-scale dimensions, materials show different properties as compared to their bulk counterpart. Indeed, two significant effects dominate by going from the macro to nano-scale dimensions, i.e. quantum-size effect and surface area (Alagarasi, 2011). Quantum-size effect occurs due to the confinement of the electrons movement. This effect in turn influences the electrical, magnetic and optical properties of the materials. Nano-scale materials possess relatively larger surface areas as compared to the same mass of the materials in the bulk form. This characteristic greatly promotes the chemical reactivity as well as affecting the strength of the materials. Therefore, nanomaterials possess improved properties as compared to their bulk counterparts, such as high surface area to volume ratio, good mechanical strength and some unique physical and chemical properties. The fascination of nanomaterials from these unique characteristics provides a huge potential for interesting materials and novel applications, particularly in healthcare, environmental protection, textiles, electronics, cosmetics etc.

The advancement of technology in machineries and devices has enabled the extensive development of these nano-scale materials (Society & of Engineering, 2004). A number of fabrication techniques arise for the production of nanomaterials. Depending on the desired morphology, production technique varies from the bottom-up to the top-down approaches, where methods such as plasma arching, chemical vapor deposition, ball milling, melt pro-

cessing, electrospinning and etc. are commonly utilized (Alagarasi, 2011; Cao & Wang, 2004; Society & of Engineering, 2004). Focusing on the production of nanofibers, electrospinning technique arises as one of the prominent methods in the recent years due to a number of advantages such as the requirement of simple tools, versatility, cost-effectiveness and most importantly its consistency in obtaining nano-sized fibers (Baji et al., 2010; Pillay et al., 2013).

Electrospinning as a straightforward method for nanofiber fabrication utilizes a high voltage to produce ultra-fine fibers. This technique has been known for almost 100 years since it was patented in the year of 1934 (Zhao et al., 2005). A standard setup for electrospinning comprises of a syringe pump, a high voltage direct current supply, a grounded collector and a spinneret, which is usually attached to a syringe containing the desired polymer solution to be electrospun. When a sufficiently high voltage is applied to the polymer solution, electrostatic forces overcome its own surface tension, producing a charged jet which accelerates towards the electrically grounded collector. Solvent evaporation occurs on the accelerating jet which leads to the deposition of ultra-fine fibers on the grounded collector (Baji et al., 2010; Pillay et al., 2013). This technique enables the production of nanofibrous structures with novel physical properties such as high surface area to volume ratio, interconnected open pores, high porosity with narrow pore size distribution as well as its high water flux and permeability to gases.

Electrospinning offers a unique ability to produce continuous fibers from different materials and to tailor the assemblies or textures for different purposes. These highly desirable features lead to the in-depth investigations for a number of potential applications, such as in the filtration, distillation, separation, biomedical and drug delivery fields. In these applications, electrospun nanofibrous membranes are frequently subjected to complex stresses and strains which could lead to the failure of materials. Therefore, the understanding of the mechanical properties is crucial in order to facilitate the product design and performance

evaluation of the materials. Until now, the probing of mechanical response of electrospun nanofibrous structures relies heavily on the experimental characterizations, such as atomic force microscopy (AFM), nanoindentation, nanotensile testing or conventional tensile testing. These experimental techniques are often inconvenient, daunting, costly and time consuming. This in turn leads to an undesirable increase in the operating costs for the industries. Consequently, there is an urgent need for a robust and cost-effective alternative solution in order to reduce the dependency on the experimental works. For this purpose, a robust numerical tool can be developed for the prediction of the material performance during the service life. The numerical tool enables the simulation and prediction of simple and complex mechanical responses with ease. Therefore, the strong dependence on mechanical characterizations can be significantly reduced.

To address the above industrial challenges effectively, the present thesis focuses on the development of a simple constitutive model with reduced number of material parameters for the mechanical response of randomly oriented electrospun nanofibrous membranes. Polyvinylidene fluoride (PVDF) is chosen as the material of interest due to its outstanding properties including the excellent thermal and chemical stability against a wide range of harsh chemicals. To achieve its objective, the thesis is divided into two main parts, i.e. experimental part and constitutive modeling part. The outcomes of the thesis are expected to contribute to promoting a potentially significant amount of cost saving during new electrospun nanofibrous product design and development in Malaysia nanofiber industries.

1.2 Research objectives

The main goal of the thesis is to develop a robust numerical tool. In order to achieve the main goal, the three objectives of the thesis can be summarized as follow:

1. To fabricate PVDF nanofibrous membranes by using the electrospinning technique.

2. To investigate the surface morphology and mechanical response of electrospun nanofibrous membranes.
3. To propose a simple phenomenological model to capture the observed mechanical response of electrospun nanofibrous membranes.

1.3 Significance of research

The present study can be considered as a first step towards the development of a robust numerical tool for the prediction of in-service performance and durability of electrospun nano and micro fibrous structures. In fact, if a fast and cost-effective numerical tool can be established, the high dependence on costly and time consuming experimental methods can be significantly reduced. Thereby, reducing the design phase of new small device and promoting potentially significant amount of cost saving in highly competitive fiber related industries.

1.4 Scope of work

The present thesis focuses on the constitutive modeling of the mechanical response of randomly oriented electrospun nanofibrous membranes. Polyvinylidene fluoride (PVDF) is chosen as the material of interest for the fabrication of nanofibrous membranes through the method of electrospinning. Simple and complex mechanical tests are conducted to provide information on the mechanical responses of randomly oriented electrospun nanofibrous membranes, as well as to serve as important experimental results for the validation of the proposed model. Volume change, Poisson's ratio and fiber orientation of the structures are also investigated for a clearer insight. For the model development, the response of the structures is proposed at the fiber scale and extended to the macroscopic scale, through the use of affine motion. Non-linear elasticity and elasto-plasticity are adopted to describe the behaviors of the structures. Here, simulations are conducted by assuming that the randomly

oriented structures are initially isotropic in-the-plane. Finally, the efficiency of the proposed model is assessed through comparison with the experimental data.

1.5 Thesis organization

The thesis is organized as follows. Chapter 1 provides the general introduction and background of the research. The objectives of the research are also presented. Chapter 2 gives a brief literature review on the existing works relevant to the current research studies. The review provides an introduction on the electrospinning processing method, where the theory of electrospinning and effects of each electrospinning parameter are discussed. Moreover, the mechanical characterization tests and the constitutive modeling of electrospun membranes conducted in the past are reviewed. Subsequently, some potential applications of electrospun structures such as tissue engineering and drug delivery applications are also briefly discussed in this chapter. Chapter 3 describes the methodology of the research. First, experimental methods for the fabrication of electrospun nanofibrous membrane, surface morphology analysis, measurement of porosity, mechanical characterization and fiber orientation analysis are discussed in detailed. Subsequently, the development of a simple phenomenological model based on the existence of strain energy function is described. Chapter 4 and Chapter 5 present the results and discussions based on the experimental findings and modeling of the mechanical response respectively. Data obtained from the experimental and simulation works are plotted into tables and graphs for further analysis. The morphological structures, mechanical responses, fiber re-orientation and the performance of the proposed model are discussed. Finally, Chapter 6 summarizes the research works. Moreover, suggestions for future works are provided in view of improving the current works.

CHAPTER 2: LITERATURE REVIEW

In this chapter, a brief review on existing relevant works in literature are presented. This includes the basic theory of electrospinning, important electrospinning parameters, the mechanical responses, constitutive modeling and some potential applications of electrospun materials.

2.1 Generality on polymer

“Polymer” is a term derived from ancient Greek words, where “poly” means “many” while “mer” means parts. Generally, polymer refers to a large molecule made up of many smaller repeating units known as monomers that are covalently bonded (Staudinger, 1920). Polymeric materials are mainly composed of carbon and hydrogen. They have relatively low density, are extremely ductile and pliable. There are a number of ways to classify polymers, depending on the origin of polymers, polymer structures, mechanisms of polymerization, physical properties as well as their technological uses (Ebewele, 2000; Fried, 2014).

Among these, the most basic and distinct classification is based on the origin of polymers, i.e. natural and synthetic polymers (Ebewele, 2000). Natural polymers occur naturally in the environment such as wool, cellulose, natural rubber or in the body of organisms such as enzymes, proteins and nucleic acid. Meanwhile, synthetic polymers arise from the man-made polymerization process. Some commonly known synthetic polymers in our daily life include polystyrene (PS) for food containers, polyethylene (PE) for plastic bags, polyvinyl chloride (PVC) for pipes and wire insulators and many more.

The molecular structures of polymers can be linear, branched or cross-linked, depending on the polymerization conditions (Figure 2.1). Polymers can consist of amorphous or crystalline parts. In crystalline regions, molecules are arranged uniformly and packed; while in amorphous regions, molecules are loosely and randomly arranged. While poly-

mers can have a totally amorphous phase, there is no single polymer that is 100% crystalline (Chalmers & Meier, 2008). The degree of crystallinity was introduced in order to determine the fraction of uniformly arranged molecules in a polymer, i.e. the crystalline phase (Ehrenstein & Theriault, 2001).

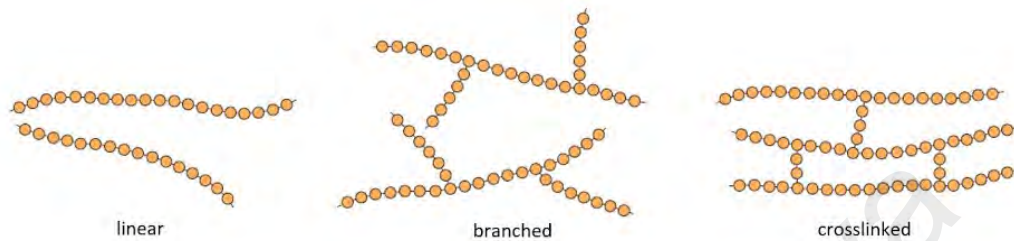


Figure 2.1: Linear, branched and crosslinked polymers (Callister & Rethwisch, 2011).

Subsequently, there are two main categories of solid polymers: thermoplastic polymers and thermosetting polymers. Thermoplastic polymers are soft when heated and harden when cooled, allowing them to be easily worked and molded for many applications. Some examples of thermoplastic polymers include polyvinyl chloride, polyethylene and nylon. However, unlike thermoplastics, thermosetting polymers become permanently hard during formation and do not soften upon heating. The covalent crosslinks in thermosets hold the chains together, resisting the chains motion even upon the application of heat. Therefore, thermosetting polymers are also called the network polymers (Chalmers & Meier, 2008). Some examples of thermosetting polymers include vulcanized rubber, phenolics and epoxies.

Apart from that, solid polymers can be further classified into plastics, elastomers and fibers, depending on the structure and alignment of the molecules. Fibers are linear polymers that are drawn into long filaments with very high length-to-diameter ratio (at least 100:1). Fibers possess high intermolecular forces that contribute to the high tensile strength and high elastic modulus, but with moderate deformability. Meanwhile, elastomers possess an irregular molecular structure, weak intermolecular forces and flexible polymer chains. Elastomers are amorphous polymers that are highly elastic and therefore can be easily de-

formed to extremely high strain and recover rapidly upon the removal of applied stress. Elastomers are usually thermosetting polymers that require vulcanization (formation of cross-links), but may also be thermoplastic polymers. Finally, the molecular arrangement of plastics falls between fibers and elastomers, where plastics can be amorphous or semi-crystalline. Plastics possess structural rigidity under the application of load. However, there are sometimes blurred demarcation between plastics and fibers, since some materials can exist in both forms, depending on the choice of processing method (Ebewele, 2000).

Over the years, polymers have gained increasing importance due to their wide range of properties as well as their endless possibilities to create materials of the desired features and quality. Throughout the decades, polymers have been penetrating into our daily life, influencing the way we live in such a secret manner. We are enjoying the products that were derived from polymeric materials every single day, from simple human needs such as food, clothing and household products to the greater applications such as components in electrical or electronics, transportations and biomedical industries, without even aware that polymers are playing important roles in these applications. Lately, polymers have been divided accordingly on the basis of their functions into three groups: commodity polymers, engineering polymers and specialty polymers. Commodity polymers are the polymers that commonly used in daily life that do not require high precision and mechanical properties. These polymers are used in high volume and are of low cost, for the products such as plastic bags, containers and a variety of household products. Some examples of commodity polymers include polystyrene (PS), polyethylene (PE), polypropylene (PP), polyvinyl chloride (PVC) and etc. Engineering polymers are polymers that require high precision and mechanical properties, for the usage in engineering parts such as bearings, gears and auto parts. These polymers are produced in lower quantities and are usually expensive. Nowadays, engineering polymers are gradually replacing the conventional materials such as wood or metal owing to their superior properties and the flexibilities in manufacturing

processes. Some examples of engineering polymers include acrylonitrile butadiene styrene (ABS), polycarbonates (PC), polyamides (nylons) and etc. Specialty polymers refer to polymers that are tailor-made with special properties or characteristics for specific applications. Conducting polymers, biodegradable polymers, biomedical polymers and polymer composites fall into this category (Ashraf, n.d.).

Generally, polymers provide a good alternative to the conventional materials due to their lower cost, superior properties as well as the flexibilities to tailor different desired properties. It is undeniable that polymers have made our life easier and better. Therefore, the existence of polymers as well as the hard works of the scientist should not be taken for granted but should be highly appreciated.

2.2 Electrospinning

In this section, the introduction of electrospinning, electrospinning theory and the effects of electrospinning parameters will be discussed in detail.

2.2.1 Introduction of electrospinning

Electrospinning has received a great attention due to its ability to consistently produce polymeric fibers in the diameter range of 5 to 500 nm. This processing technique for fiber production has been known for almost 100 years since it was patented in 1934 (Zhao et al., 2005). Yet, interest on this processing method can still be seen from the tremendous works done by the researchers from all over the world. A number of advantages contribute to the rapid emergence of electrospinning as a powerful method for nanofibrous membrane fabrication such as the requirement of simple toolings, versatility, cost-effectiveness and most importantly its ability to produce very fine fibers down to nanometer sizes. Moreover, some added advantages such as the high surface to volume ratio, high porosity and interconnected porous network altogether contribute to the importance of electrospinning which differentiate it from other membrane fabrication methods (Baji et al., 2010). According

to Pillay et al. (2013), the electrospinning method of production results in an increase of the fiber length and a decrease in the fiber diameter compared to other membrane fabrication methods. It is reported that the interaction between the applied electrostatic field of attraction and the repulsion of surface charges contributed to these features which make electrospinning preferable over other fabrication methods (Pillay et al., 2013).

The electrospinning processing method is originated from an established processing method called electrospraying. Electrospraying applies the same mechanism as electrospinning, where a jet is accelerated from the needle tip to the collector which possesses opposite charges. However in electrospraying, the low viscosity of the solution used causes the jet to break up during its trajectory which results in the polymer droplets formation instead of fibers (Pillay et al., 2013). When the viscosity of the solution is increased, the greater viscoelastic forces prevent the jet from breaking up. The continuous jet is then deposited on the grounded collector as nanofibers, and this finally constitutes to electrospinning.

Even though this method appears to be simple and straightforward, there are still plenty of unconfirmed circumstances on the techniques and the effects of processing parameters on the structural, morphology as well as the mechanical properties of the nanofibrous membrane produced. The major challenge of electrospinning lies on the optimization of parameters in order to obtain the desired membrane properties and morphologies. Therefore, the optimization of electrospinning parameters is widely investigated in order to produce ideal electrospun materials suitable for implementation in various applications. The manipulation of various parameters such as polymer concentration, amount of solvent used, feed rate, voltage, and capillary-collector distance have been studied and discussed by a number of researchers in order to obtain defect-free materials with the smallest fiber diameter possible.

2.2.2 Electrospinning theory

A standard setup for electrospinning comprises of a syringe pump, a high voltage direct current supply, a grounded collector and a spinneret, which is usually attached to a syringe or a pipette containing the desired polymer solution to be electrospun (Figure 2.2). For the electrospinning process, one terminal of the high voltage supply is connected to the

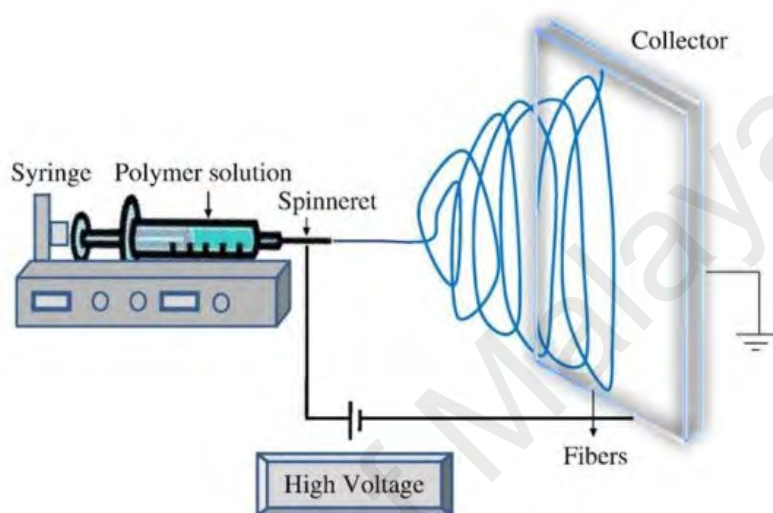


Figure 2.2: Illustration of electrospinning setup. (Retrieved August 4, 2017, from <http://ppl.ippt.gov.pl/18-few-words-about/17-electrospinning>)

spinneret while another terminal will be connected to the electrically grounded collector. The syringe pump allows the setting of the desired feed rate and it functions by pushing the syringe forward so that the polymer solution will be ejected at the tip of the spinneret.

There are four essential regions in the electrospinning process, i.e. formation of Taylor cone, steady jet region, instability region and lastly the base region (Kodolov et al., 2014; Haghi et al., 2017).

Initially, a droplet of polymer solution or polymer melt is formed at the tip of the needle. The electric field is applied to the needle tip, causing the polymer droplet to be electrically charged. As the applied voltage increases, the shape of the droplet transforms gradually from hemispherical into a conical shape due to the repulsive forces between charges. This conical shape is known as the “Taylor cone” (see Figure 2.3) and it functions as the initiating surface for the formation of jet (Kodolov et al., 2014; Haghi et al., 2017). In de-

tail, the Taylor cone was first described by Sir Geoffrey Taylor in 1964 in his research work “Disintegration of water droplets in an electric field”. The initial work of Taylor focused on the behavior of water droplets when subjected to strong electric field (Taylor, 1964). His works contributed significantly to the theory of electrospinning which benefited the later generation.

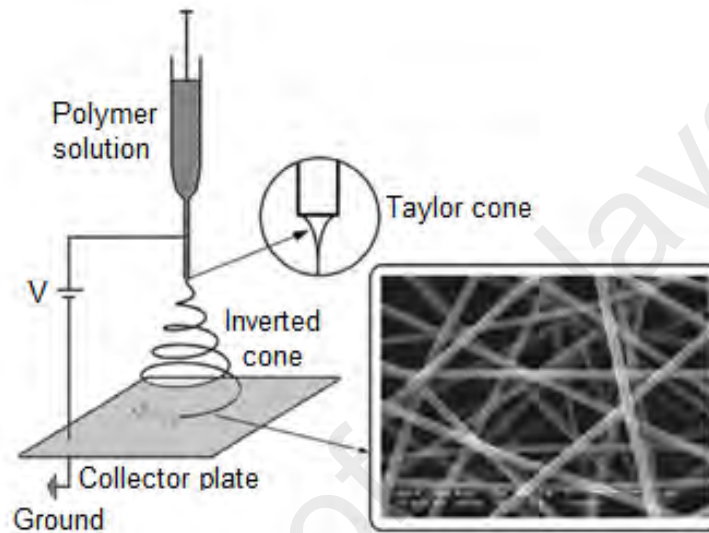


Figure 2.3: Formation of Taylor cone in electrospinning process (Kodolov et al., 2014).

When the applied electric field reaches a critical voltage, the repelling forces of the surface charges overcome the surface tension and viscous forces of the droplet, causing jet ejection from the rounded tip of the Taylor cone. The ejection of jet signifies the beginning of an electrospinning process (Taylor, 1964, 1969). At this stage, the jet starts thinning in a straight and steady manner with time (Haghi et al., 2017).

Following this, the thinning of jet proceeds into the instability region of the electrospinning process. This region can be further divided into three types of instabilities, i.e. Rayleigh instability (axisymmetric), bending instability (axisymmetric) and whipping instability (non-axisymmetric) as shown in Figure 2.4 (Derch et al., 2004; Kodolov et al., 2014; Haghi et al., 2017). Rayleigh instability is dominated by surface tension, and is commonly observed under low electric field strength or when the polymer solution is below an optimum viscosity. The surface tension force causes the breaking up of jet and eventually

leads to beaded fiber morphology (Kodolov et al., 2014; Baji et al., 2010).

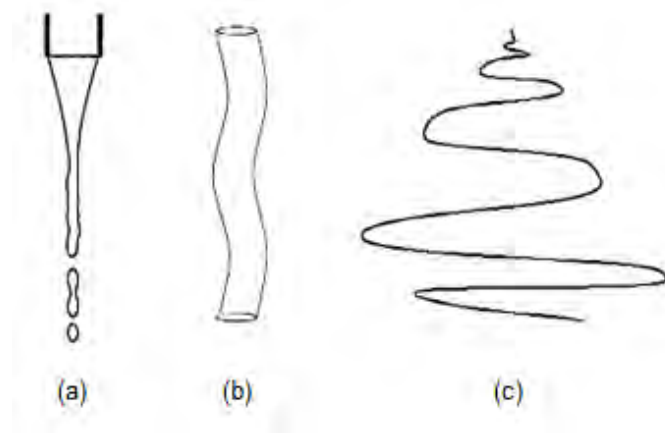


Figure 2.4: Instabilities in the jet: (a) Rayleigh instability, (b) bending instability and (c) whipping instability (Kodolov et al., 2014).

At higher electric field strength, the Rayleigh instability is suppressed while bending and whipping instabilities dominate. For both types of instabilities, excess charges in the jet bring about the repulsion of charges which further promote the thinning and elongation of the jet. Bending instability produces oscillations in the diameter of the jet, in the axial direction (Kodolov et al., 2014).

At much higher electric field strength with sufficient charge density in the jet, the axisymmetric instabilities (Rayleigh and bending) are suppressed while the non-axisymmetric instability (whipping) is promoted. Whipping instability produces further bending and stretching forces on the jet, resulting in high degree of jet elongation which further reducing the jet diameter from micrometers to nanometers (Haghi et al., 2017).

Finally, as the charged jet travels towards the collector, solvent evaporation occurs and the elongation and thinning of charged jet continue until solidification takes place. Nanofibers are deposited onto the electrically-grounded collector.

In summary, during electrospinning, the syringe containing the polymer solution will be constantly pushed forward following the desired feed rate that is set onto the machine. A high voltage is applied at the needle tip of the syringe where the solution is consistently ejected. The setup is set such that the needle tip of the syringe is oppositely charged relative

to the grounded collector. In the presence of a sufficiently high electric field, the polymer solution ejected at the needle tip will be elongated and distorted into a cone shape, which is known as the “Taylor Cone” (Pillay et al., 2013; Zhao et al., 2005). Critical electric field strength is essential for the formation of the ultra-thin fibers. At an applied voltage which is lower than the critical value, the surface tension of the polymer solution prevents the breaking of the solution as well as the ejection of polymer jet. Increasing the intensity of the electric field until the critical value induces sufficient charges on the liquid surface which repel each other and create shear stresses that overcome the surface tension (Baji et al., 2010). Finally, a jet of polymer solution is ejected and accelerated towards the collector with opposite charges. Solvent is evaporated during the travel which leads to the deposition of ultra-fine fibers on the grounded collector. The process of electrospinning is summarized and shown in Figure 2.5.

2.2.3 Effects of electrospinning parameters

According to Li and Wang (2013), working parameters for electrospinning are divided into three groups, i.e. solution parameters, process parameters and lastly the ambient parameters (see Figure 2.6). Solution parameters include the polymer concentration and molecular weight, as well as the viscosity, surface tension and conductivity of the polymer solution. Meanwhile, processing parameters include the voltage, feed rate, type of collector used and the distance from needle tip to collector. Lastly, ambient parameters include all the surrounding influences such as temperature and relative humidity. Nanofibrous membranes with desired morphologies and diameters can be successfully fabricated by properly controlling each of these parameters.

Pillay et al. (2013) reviewed the effect of processing variables, which include the applied voltage, feed rate for electrospinning, polymer concentration or the solution viscosity,

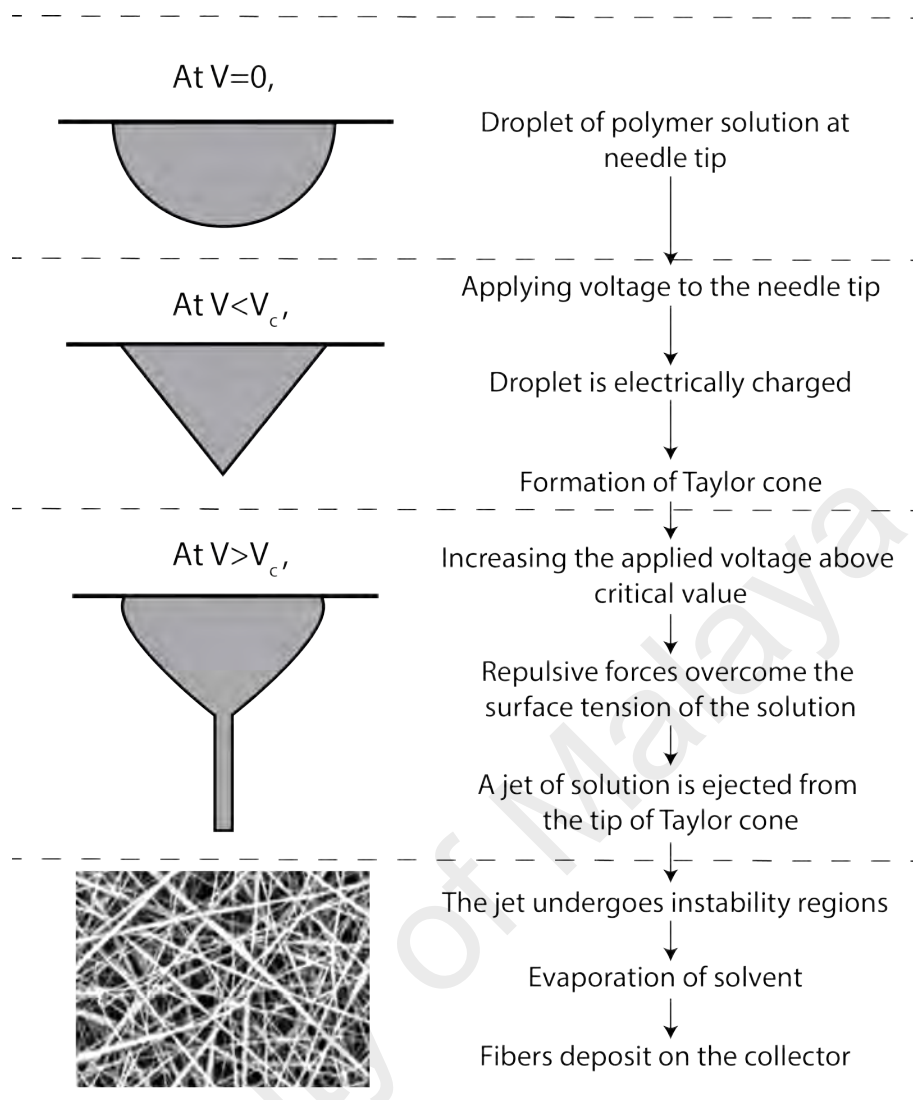


Figure 2.5: Summary of electrospinning process.

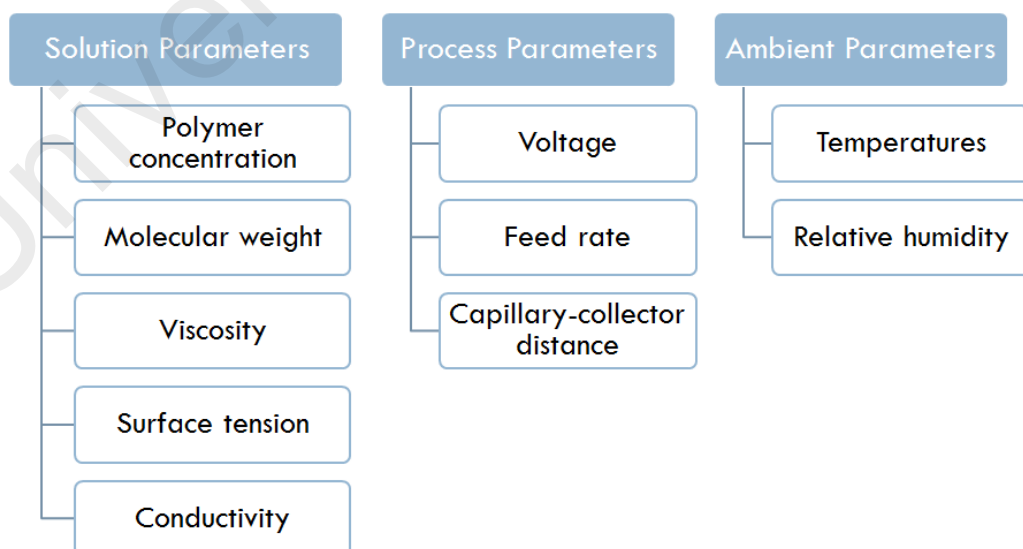


Figure 2.6: Classification of electrospinning parameters.

solvent selection, solution conductivity and the distance between needle tip and grounded collector on the results of electrospinning. In Zhao et al. (2005), the preparation of PVDF membranes was done by varying the amount of solvent, the polymer concentration and also the capillary-to-collector distance. Through a series of experimental works, the first two parameters are said to be the main influences affecting the properties of the electrospun PVDF membranes. In S. H. Tan et al. (2005), the effects of processing parameters were also studied and a processing map was produced which summarized the parameter effects on the electrospun fibers morphology. Subsequently, it was deduced that the polymer concentration, polymer's molecular weight and the electrical conductivity of the polymer solution were the most prominent parameters affecting the morphology of the electrospun nanofibrous membrane.

2.2.3.1 Effects of polymer concentration

Polymer concentration or the weight percentage of polymer used for the electrospinning solution plays a major role on the morphology of the electrospun nanofibrous membrane. Normally, the diameter of the electrospun fiber increases with increasing polymer concentration, and this phenomenon has been reported in a number of literatures, i.e. Beachley and Wen (2009) and Pillay et al. (2013).

According to Li and Wang (2013), there are four critical concentrations which should be noted when preparing the solution for electrospinning. A very low concentration of polymer will produce nano-particles instead of nanofibers due to the low viscosity and high surface tension of the solution, which causes electrospray. When the concentration is slightly increased, a mixture of fibers and beads will be produced. Meanwhile, a concentration which is too high will produce helix-shaped microribbons instead of fibers. Hence, smooth nanofibers can only be obtained when appropriate concentration of the polymer is utilized.

Optimum polymer concentration and solution viscosity are needed in order to produce the desired smooth, beads free nanofibers. At lower polymeric concentration, the charged jet fragmented into droplets instead of fibers because the viscoelastic forces are too low to overcome the repulsive forces of charge in the jet of solution. Increasing the polymer concentration increases the viscosity of the polymer solution as well. At this point, the higher viscoelastic forces improve the entanglement between polymeric chains and hence preventing the fragmentation of the fiber jet. Smooth nanofibers with little or no bead defects can be produced if other processing parameters are kept optimum. However, a further increase of the concentration beyond the critical limit will produce highly viscous solution for nanofiber formation, and the solution will be dehydrated at the tip of the capillary (Doshi & Reneker, 1993; Greiner & Wendorff, 2007; Meechaisue et al., 2006; Venugopal et al., 2004).

Deitzel et al. (2001) and Zong et al. (2002) observed irregular morphologies of nanofibers with bundles and junctions at lower polymer concentration. Increasing the polymer concentration in the optimum range decreases the irregularities, bundles and junctions due to the reason that adequate drying can be easily achieved at higher polymer concentration. Meanwhile, Zhao et al. (2005) tested on a few polymer concentrations in order to determine the trend of increasing polymer concentration on the morphology of the fibers produced. It was observed that a low polymer concentration of 10% produced a large number of beaded fibers. As the polymer concentration increases from 10% to 15%, the number of beads decreases until they become not visible at 15% polymer concentration. However, further increase in the polymer concentration did not produce better results. Instead, it hinders the formation of ultrafine fibers due to the highly viscous condition of the polymer solution.

Overall, it can be summarized that viscosity and surface tension are essential in determining the effective range of polymer concentrations to produce the desired smooth, defect free nanofibers (Pillay et al., 2013).

2.2.3.2 *Effects of solvent selection*

According to Pillay et al. (2013), there are two important considerations when selecting the suitable solvent for a particular polymer, i.e. the polymer solubility in the solvent and the boiling point of the solvent, which indicating its volatility. Volatile solvent is always preferable due to its higher evaporation rate which facilitates complete drying of nanofibers upon reaching the collector. Nevertheless, solvents with too high or too low volatilities should be avoided, since highly volatile solvents could clog the capillary tip due to the rapid solvent evaporation while solvents with very low volatility will form nanofibers with flat ribbon-like morphology due to the incomplete drying during deposition of fibers onto the collector.

A blend of two solvents with different boiling points was introduced into the electrospinning process where it was experimentally shown that the desired porosity and topographies can be achieved when the optimum proportion of two solvents are used as a co-solvent (Cozza et al., 2013; K. Hwang et al., 2011; Jang et al., 2011; Liao et al., 2013; Zhao et al., 2005). Megelski et al. (2002) found that smoother polystyrene nanofibers with desired pore density can be produced when tetrahydrofuran (THF) and dimethylformamide (DMF) are combined in the correct ratio. While in Meechaisue et al. (2006), the combination of dichloromethane (DCM) and methanol produced desired smooth nanofibers as compared to the use of DCM alone.

It was also found that the composition of the two solvents plays an important role in determining the morphology of the electrospun PVDF membrane. The purpose of using two different solvents was due to the difference in the vapour pressure where a mixture of both facilitates the formation of nanofibers. DMF and DMAc (dimethylacetamide) are the common solvents for the fabrication of PVDF nanofibrous membrane. However, the use of DMF or DMAc alone induces difficulty in producing the desirable ultrafine fibers. It

was found that the problem could be solved through the addition of Acetone to DMF or DMAc (Zhao et al., 2005; Gopal et al., 2006). In this case, Acetone has a higher vapour pressure than DMF or DMAc and the addition of acetone weakens the PVDF-DMF/DMAc interactions. This condition produces a polymer solution with higher vapour pressure and promotes better solvent evaporation due to the weakened interactions. Thus, the addition of an appropriate amount of acetone promotes better surface morphology with fewer beads which is desirable for real life applications (Cozza et al., 2013).

In Zhao et al. (2005), DMF and Acetone were used to dissolve PVDF powder. It was mentioned that the prominent characteristics of DMF such as its strong polarity, high electron donating index, dielectric constant and dipole moment contributed to the production of ultra-fine nanofibrous membranes. However, the high boiling point of DMF which is around 153 °C corresponds to a low volatility of the solvent hinders the generation of ultrafine fibers during the electrospinning process. This encourages the use of acetone as the second solvent in Zhao et al. (2005) owing to its lower boiling point, i.e. 56.2 °C and eventually a higher volatility.

Overall, DMF and acetone were mixed with a few ratios which produce different fiber morphologies. It was found that a more uniform morphology with fewer numbers of beads could be obtained through the addition of the second solvent acetone. Meanwhile, it is understood that different polymers require different types of solvents, where there is nothing as the best solvent for all polymers. As in the case of Son et al. (2004) and Yang et al. (2004), three to four solvents were investigated in order to obtain the nanofibers with desired morphologies. Hence, the morphology of nanofiber can be regulated by properly choosing solvents or the combination of solvents.

2.2.3.3 *Effects of solution conductivity*

An increase in solution conductivity leads to a substantial decrease in nanofiber diameter produced by electrospinning (Pillay et al., 2013). This is because the polymer solution of higher conductivity has a greater charge carrying capacity, which causes the fiber jet to exhibit a greater tensile force when voltage is applied during electrospinning.

Fong et al. (1999) and Zong et al. (2002) in their studies investigated the effect of adding salts to the diameter and the morphology of nanofiber produced. It was observed that upon the addition of salts such as sodium chloride (NaCl) into the polymer solution, smooth, uniform and bead-free nanofibers with smaller diameter were produced as compared to the nanofibers that were electrospun from polymer solutions without salt. It was explained in Fong et al. (1999) that the addition of NaCl salts increased the net charge density of the solution, which in turn increased the conductivity of the solution, causing a greater elastic force within the jet resulting in the formation of smoother and thinner nanofibers.

It was also reported by Beachley and Wen (2009) that fibers with reduced beads were produced with the addition of salts to the polymer solution. It was mentioned that this method improved the conductivity of the solution meanwhile increased the surface charge density of the solution jet. Besides, Zong et al. (2002) investigated the effect of different type of salts on the outcome of the electrospinning. It was deduced that the nanofiber diameters were correlated with the radii of ions added, where an ion with smaller radius producing a nanofiber of smaller diameter. Later, it was explained that ions with smaller radii possessing a higher charge density which gave rise to a greater elongation forces during electrospinning.

2.2.3.4 *Effects of applied voltage*

For the electrospinning process, there are always a critical value and an optimum range of applied voltage for every polymer solution, which highly depends on the polymer-solvent

system. When the applied voltage is above or below the critical value, the electric field that is stronger or weaker will result in beaded morphologies or even an inhibition of the jet initiation (Pillay et al., 2013).

In Sill and von Recum (2008), it was observed that the nanofiber diameter can be affected by the manipulation of the applied voltage. Nanofiber diameter tends to decrease when the voltage is increased beyond the critical voltage but then increased again after a definite point. According to Pillay et al. (2013), the initial decrease in the nanofiber diameter in Sill and von Recum (2008) was due to the higher degree of jet stretching correlated to an increase in the charge repulsion due to the increased voltage. Whereas in Deitzel et al. (2001), it was reported that defect free nanofibers were obtained when the jet was initiated from the apex of the Taylor Cone. It was also reported that the bead defects increased as the applied voltage increased. Deitzel et al. (2001) tested four ranges of voltages which brought four different observations on the jet ejection of the poly(ethylene oxide) solution. For a transition of low to high voltage, the jet was observed to be ejected from the apex of Taylor Cone, from the Taylor Cone but at the bottom of solution droplet, from the Taylor Cone at the capillary tip and from the inside of the capillary tip. Apparently, this contributed to the differences in morphologies. The last observation possesses the highest number of beaded nanofibers. Similar results reported by Zong et al. (2002) that minimal beads defects was noted when the jet originated from the tip of Taylor Cone.

2.2.3.5 Effects of feed rate

Flow rate or feed rate is one of the important parameters which is categorized as one of the process parameters in Li and Wang (2013). It is more recommended to use a lower feed rate for electrospinning so that the polymer solution will have sufficient polarizing and drying time prior reaching the collector. In the case where a high flow rate is used, beaded fibers with thicker diameter will usually be obtained instead of the desired smooth fibers

with thinner diameter. However, according to Beachley and Wen (2009), feed rate does not significantly affect fiber diameter and the overall uniformity of the fibrous membrane produced. It was mentioned that when the feed rate is sufficient for fibers forming, higher feed rate will only provide more polymer solution than needed, which form as excess solution at the needle tip.

In some cases where high applied voltage is desired, the volume of polymer drop that forms the Taylor Cone decreases due to the increased applied voltage (Deitzel et al., 2001). Subsequently, the decrease in volume of the polymer drop causes the following jet to be ejected from the inside of the capillary tip which causes the increase in beads formation. In order to maintain the shape of Taylor Cone and to reduce beads formation, a minimum feed rate is critically needed to constantly replace the solution that is being ejected to form nanofibers (Pillay et al., 2013).

Diameter and pore size were observed to increase when the flow rate was increased (Megelski et al., 2002). However, when flow rate became too high than it was needed, more beads were observed and flattened ribbon-like nanofibers appeared. Both phenomena happened owing to the incomplete drying of the nanofibers upon reaching the collector. Meanwhile in Zong et al. (2002), it was observed that lowering the feed rate of electrospinning decreased the nanofiber diameter and also bead defects, which is another phenomenon that concurs with Megelski et al. (2002).

2.2.3.6 Effects of capillary-collector distance

Another concern which is often kept constant in the electrospinning process is the distance between the collector and the needle tip. It is understood that the distance of the collector to the needle tip reflecting the distance where the polymer solution gets to solidify by the evaporation of the solvent (Li & Wang, 2013). A shorter distance leads to a shorter time for the solvent to evaporate, but when the distance is too long, bead fibers

might be obtained. However, it was demonstrated in X. Yuan et al. (2004) that slightly longer distance helps in obtaining a thinner fiber diameter which is more preferable by all the researchers. Despite that, Zhao et al. (2005) mentioned in their paper that the capillary-collector distance plays a less significant effect on the electrospinning of PVDF nanofibrous membranes. Three different distances, i.e. 10 cm, 15 cm and 20 cm were tested and the results show no visible difference between the images taken by SEM.

Although some of the above works mentioned that the distance between capillary and collector influences the size and morphology of the electrospun nanofibers, still the effect is less distinct as compared to the other processing parameters. Nevertheless, an optimum distance between capillary and collector is always desired where a shorter or longer distance might enhance beads formation or the occurrence of eletrospraying. Smaller distances might cause incomplete drying of the nanofibers where the solvent does not have sufficient time to evaporate upon reaching the collector, and this produces ribbon flat-like structure nanofibers which are not desirable (Pillay et al., 2013).

2.2.3.7 *Effects of ambient*

Evaporation rate and solidification are the two important factors that affect the fibers diameter of the electrospun membrane. Meanwhile, the rate of solvent evaporation and solidification process are controlled by the relative humidity of the surrounding. The increase in humidity decreases the rate of solvent evaporation which consequently slows down the solidification process, allowing a longer time for fiber elongation and thus forming thinner fibers. However, as the relative humidity increases above a critical value, beads are seen to be formed on the thin fibers, which is undesirable in most of the cases. The formation of beaded fibers above critical relative humidity is caused by the capillary instability before the jet solidified (Tripatanasuwan et al., 2007).

Cozza et al. (2013) found that the surrounding airflow and relative humidity affect the

electrospinning products. It was observed that a higher airflow contributed to homogeneous and bead-free nanofibrous membranes as compared to that of lower airflow. Meanwhile, increasing relative humidity was found to increase the uniformity of the nanofiber diameters until the optimum value was reached. Hence, these findings indicate the importance of ambient effects on the morphology of the end products which were always neglected in electrospinning.

2.3 Mechanical properties of electrospun nanofibrous membranes

Most of the investigations for electrospun membranes have been focused on the manipulation of chemical content and physical properties, in order to produce materials with good functionalities for various purposes. As mentioned in the previous sections, the electrospinning parameters affecting the physical properties of the resulting membranes have been extensively studied for various types of polymers. Nevertheless, the mechanical properties of the desired materials are often neglected or merely discussed in brief. The extensive usage of polymer nanofibers for a wide range of applications such as filtration, tissue engineering etc. required high sustainability of the nanofibers due to the continuous stresses and strains encountered during their service lifetime. Thus, the understanding of the mechanical properties of electrospun materials is particularly important especially under the cases of complex loading conditions, in order to facilitate in the material design and allow the prediction of the materials performance over the service duration. However, the difficulties in specimen handling and low deformation load measurement often obstruct the idea of conducting mechanical testing on the electrospun nanofibrous membrane. This resulted in the lack of knowledge on the mechanical aspect of electrospun fibers.

2.3.1 Factors affecting the mechanical properties

According to Baji et al. (2010), electrospun nanofibrous materials possess unusual mechanical properties which are significantly different from their bulk counterpart. These dif-

ferences are attributed to the electrospinning process. Subsequently, Baji et al. (2010) listed four factors that influence the mechanical properties of electrospun membranes: (1) fiber structural morphology, (2) geometrical arrangement of fibers, (3) individual fiber properties and (4) interactions between fibers.

The structural morphology mentioned previously refers to the morphologies at the molecular and fiber scales. During the electrospinning process, changes of structural formation take place at the molecular scale which affect the crystallinity of the resulting electrospun membranes. It is understood that the amorphous regions impart elastomeric properties while the crystalline regions provide dimensional stability to the molecular structure. Consequently, the molecular arrangement in the fibers determines the degree of crystallinity and thus influences the macroscale mechanical properties of the electrospun materials. Apart from that, Curgul et al. (2007) proposed that the single electrospun fiber can be differentiated into skin and core regions with different morphologies, in which the core region possesses bulk-like structure. Subsequently, the deformation mechanism is determined by the orientation of the amorphous chains in the supramolecular region of the fibers. Relating the understanding to the effect of fiber diameter on tensile strength, the effect of skin region dominates as the fiber diameter decreases due to the diminishing core region and which leads to a higher proportion of skin region. Therefore, the tensile strength of a single fiber is improved when the fiber diameter decreases due to the higher proportion of the skin region which dominates the mechanism of deformation.

The collector type affects the tensile properties of the electrospun materials in an indirect way, i.e. the morphology of the electrospun membrane is determined by the type of collector used. In electrospinning, the use of a stationary collector produces randomly oriented fibers while aligned fibers are fabricated utilizing rotational collectors. Subsequently, randomly oriented and aligned fibrous mat give rise to different mechanical properties even though the same precursor materials are used for the fabrication. According to Baji et

al. (2010), the mechanical deformation highly depends on the degree of fiber alignment. This is because during tensile loading, only the fibers which are oriented in parallel to the loading direction will be subjected to the stretching force while those fibers that are perpendicular to the loading direction will less likely to experience a loading force. Besides, it is also mentioned that the randomly oriented fibrous materials consist of higher porosity as compared to the aligned fibrous materials. Consequently, the overall tensile strength and modulus of randomly oriented electrospun materials is lower than that of the aligned electrospun materials.

Furthermore, the fiber diameter plays an important role in determining the tensile properties of the material. As mentioned earlier, a fiber exhibits improved tensile properties when the proportion of the supramolecular structures or the skin regions is comparable with the overall size of the fiber. Therefore, increasing the fiber size decreases its tensile strength and modulus (Baji et al., 2010). In Wong et al. (2008), the effect of fiber diameter on the tensile properties of electrospun poly(ϵ -caprolactone) was investigated. From the observation of the graph of tensile strength and tensile modulus versus fiber diameter, a critical value for fiber diameter existed where an abrupt improvement of the mechanical performance can be seen as the fiber diameter went below this value. It was mentioned that the improved tensile properties in finer diameter fibers could probably due to the more ordered arrangement of molecular chains that leads to higher crystallinity as well as due to the densely packed lamellar and fibrillary structures. Subsequently, the highly oriented structures provide a higher resistance to the applied tensile force during mechanical deformation, resulting in higher tensile strength and modulus of the material.

Recently, more researchers have shown interest on the mechanical behavior of the electrospun nanofibers through the characterization of the stress-strain behaviors of the material. Generally, the experimental works can be divided into two categories: (1) mechanical characterization of single electrospun fiber and (2) mechanical characterization of

macroscale electrospun membrane.

2.3.2 Mechanical characterization of single electrospun fiber

The tensile behavior of single electrospun fibers constitutes the fundamental knowledge for the understanding of the macroscale mechanical response of the electrospun membranes. However, the experimental works are often daunting and costly due to the extremely small size and delicacy of a single fiber which require the use of high precision devices.

The commercial mechanical testing systems used in the past are unsuitable for the mechanical characterization of single nanofibers, due to some challenges faced. With the improvement in technology, some of these problems could be solved. Table 2.1 summarized the challenges faced and possible solutions for the mechanical characterization of single nanofibers (E. P. S. Tan & Lim, 2006).

Therefore, new mechanical characterization techniques are needed in order to probe the mechanical properties of a single nanofiber. E. P. S. Tan and Lim (2006) mentioned three common types of mechanical characterizations for nanofibers, i.e. tensile test, bend test and indentation test done at the nanoscale.

Tensile tests of single nanofibers can be achieved through several methods, by utilizing atomic force microscope (AFM), nano tensile tester and other novel techniques (E. P. S. Tan & Lim, 2006). Among these, AFM appears to be the most prominent characterization technique due to the accuracy and sensitivity of the device. Lately, a few researchers investigated the nanoscale mechanical properties of polymers by means of AFM (Boffito et al., 2015; K. Y. Hwang et al., 2010; Mathew et al., 2005; E. P. S. Tan, Goh, et al., 2005).

In tensile testing using AFM, a single fiber was attached to the upper and lower AFM tips by means of electron beam. The upper AFM tip was on a rigid cantilever connecting the actuator and the nanomaterial, in order to apply the tensile load to the material; while the lower AFM tip was on a soft cantilever that acted as a force transducer to detect the

Table 2.1: Challenges faced and possible solutions for the mechanical characterization of single nanofibers.

Challenges faced	Possible solutions
<p>1. Difficulty in handling ultrafine fibers</p> <ul style="list-style-type: none"> • Damage may be induced on the delicate fibers during specimen handling. 	<p>Custom made or commercial micro-manipulation system</p> <ul style="list-style-type: none"> • These systems can be used for moving fibers and for attaching the fiber ends to grips or fixtures.
<p>2. Mode of observation</p> <ul style="list-style-type: none"> • Scanning electron microscope (SEM) or Transmission electron microscope (TEM) is needed for observation due to the size of fibers which is in the nanometer range. • However, non-conductive samples such as polymer nanofibers can be damaged by the used of electron beam in these SEM or TEM. 	<p>Coating of specimens</p> <ul style="list-style-type: none"> • Gold or platinum coating can be coated on the desired specimens before sending for SEM or TEM analysis. • Coating provides conductivity to the specimens meanwhile prevents the specimens from being damaged by the electron beam during SEM or TEM analysis.
<p>3. Accuracy and sensitivity of force transducer</p> <ul style="list-style-type: none"> • The load resolution of the mechanical testing system may go up to 5000 kN which could not accurately reflect the force requires to break the materials. 	<p>Use of smaller load cell</p> <ul style="list-style-type: none"> • Smaller load cell are more common nowadays which can go down to load resolution of 50 nN. • These load cell can accurately capture the force requires to break the single nanofiber, which is usually in the nano Newton range.
<p>4. Sample preparation</p> <ul style="list-style-type: none"> • It is very difficult to isolate one single nanofiber from an electrospun membrane for the purpose of mechanical characterization due to the extremely small fiber size. 	<p>Reduce electrospinning duration</p> <ul style="list-style-type: none"> • Electrospinning can be conducted for a very short duration with the collection of fabricated fibers on a tailor-made frame in order to ease the separation of nano-sized fibers.

tensile load applied on the material. By driving the upper cantilever upwards, the lower cantilever was bent upward by a certain distance, and the material was stretched due to the force exerted on it through the AFM tips. Subsequently, the applied force and the resulting strain can be computed and plotted to determine the mechanical behavior of the material (Yu et al., 2000). This technique was employed by Yu et al. (2000) on the investigation of the strength and breaking mechanism of carbon nanotubes, while a similar experiment was conducted on electrospun polyethylene oxide (PEO) nanofibers by E. P. S. Tan, Goh, et al. (2005).

Meanwhile, tensile testing using commercial nano tensile testers is more straightforward as compared to AFM. This technique was presented by E. P. S. Tan, Ng, and Lim (2005) where electrospun polycaprolactone (PCL) nanofibers collected on a rectangular cardboard frame were tested by mounting the cardboard on the nano tensile tester. In this work, nanofibers of different diameters were tested and results showed that nanofibers with smaller diameter possess higher strength but lower ductility. Besides, a nano tensile tester was also utilized in the works of Inai et al. (2005) and Wong et al. (2008) on the investigation of single nanofiber properties of poly(L-lactic acid) (PLLA) and PCL respectively. One disadvantage of using nano tensile tester is the absence of an observation system that obstruct the investigation on the mechanism of deformation and mode of failure.

Some other novel techniques for tensile testing of single fibers were also proposed, such as incorporating in situ tensile device in SEM or TEM chamber, and by mounting a nanoindenter on an AFM system. Such techniques provide promising results but daunting works need to be done prior to the tensile testing.

Apart from the tensile test, the three-point bend test is one of the common bend tests conducted for the case of single nanofibers. In this method, a nanofiber is deposited on a substrate with groove, such that the fiber is suspended over the groove for the purpose of the bend test. Normally, an AFM tip will be used for the application of small deflection at

the midspan of the specimen. Consequently, information on the degree of deflection gives rise to the mechanical properties of the material such as Young's modulus and fracture strength. This technique was employed by E. P. S. Tan and Lim (2004) in order to probe the mechanical properties of PLLA nanofibers.

Meanwhile for the indentation test of nanofibers, the sample preparation is much more convenient as compared to the previous characterization techniques. In this technique, samples can be prepared by simply adhering the nanofibers on a hard and flat substrate. Subsequently, the elastic modulus of the materials can be predicted based on the applied load and contact radius of the indenter tip. For elastic-plastic nano-indentation, Wang et al. (2004) performed nano-indentation on electrospun silk fibers by utilizing the AFM tip. Similarly, E. P. S. Tan and Lim (2005) conducted elastic nano-indentation on electrospun PLLA nanofibers. One disadvantage of nano-indentation which limits the studies on this technique is the difficulty in probing the curved surface of the nanofiber.

K. Y. Hwang et al. (2010) proposed a new "hooking" method using AFM cantilever in a SEM to characterize the mechanical properties of polymer nanofibers. In this method, a single polymer nanofiber is positioned such that it is suspended over a trench in a substrate. Then, AFM cantilever is hooked onto the midspan of the fiber and the fiber is elongated until failure. Subsequently, the stress applied can be determined through the deflection of AFM cantilever, while the fiber strain can be measured through the observation of cantilever motion by using the SEM. With this method, polyamide (Nylon 6) nanofibers with different diameters were investigated. The results indicated that fibers with smaller diameter possessed greater tensile strength. Consequently, K. Y. Hwang et al. (2010) attributed this to the higher degree of crystallinity and molecular orientation in smaller diameter fiber.

2.3.3 Mechanical characterization of electrospun nanofibrous membranes

When single electrospun nanofibers combined as a whole structure, a membrane is formed which possesses different mechanical properties as compared to the single nanofiber. The mechanical strength of the electrospun nanofibrous membrane is not merely the summation of strength of all single nanofibers, instead, some other factors arise when nanofibers are combined. Recall the four factors that influence the mechanical properties of electrospun membranes (Baji et al., 2010): (1) fiber structural morphology, (2) geometrical arrangement of fibers, (3) individual fiber properties and (4) interaction between fibers; fiber structural morphology and individual fiber properties are the material characteristics to be probed at the fiber scale. Subsequently, the arrangement of the fibers and the interaction between the fibers need to be taken into consideration when probing the mechanical properties of the electrospun membranes at the macroscopic scale.

In Huang et al. (2004), tensile tests were conducted for electrospun gelatin mat fabricated from gelatin concentrations 5 wt% to 12.5 wt%. It was found that increasing the gelatin concentration did not directly affect the mechanical performance of the material, instead the specimen fabricated from 7.5 wt% concentration possessed the highest tensile modulus and ultimate tensile strength among all. Huang et al. (2004) later proposed that the finer fiber diameter in 7.5 wt% concentration electrospun mat promoted a stronger cohesive force that gave rise to a better mechanical performance. Although 5 wt% gelatin concentration produced even finer fibers than 7 wt% concentration, the presence of tremendous amount of beads might have reduce the cohesion between the fibers and thus reducing the strength of the overall structure. In general, the combine effect of fiber diameter and presence of bead defects affects the overall mechanical performance where fine fiber size and bead free are always the desired criteria.

Dupaix and Hosmer (2010) conducted a number of uniaxial cyclic loading tests on

electrospun polycaprolactone (PCL) materials, where the effects of cyclic loading, alignment of fibers, experimental temperature and moisture were investigated. Cyclic loading was conducted on randomly oriented electrospun membranes as well as on longitudinally and circumferentially aligned membranes. Comparing the experimental results of longitudinally and circumferentially aligned samples, no significant difference was observed on the stress-strain relationship on altering the orientation of fibers. However, by comparing the mechanical responses of the aligned samples with the randomly oriented samples, the aligned samples displayed weaker failure stresses as well as the elongations at failure. These results were unexpected and did not coincide with the previous finding of Nerurkar et al. (2007) where longitudinally aligned materials were reported to possess higher stress at failure since the material was deformed in the direction of fiber alignment. Subsequently, the author attributed this phenomenon to the slow mandrel speed during the electrospinning process in which the fibers produced might not be highly aligned. Therefore, the cyclic loading results for aligned samples in the work of Dupaix and Hosmer (2010) may not be accurate and further correction will be needed for the discussion and comparison of aligned and non-aligned fibrous membranes.

On top of that, Molnar et al. (2012) conducted a number of tensile tests on polyamide-6 (PA-6) electrospun nanofibrous mats. The electrospun mats were cut into stripe-shaped samples and adhered to the paper frames for easy handling. Subsequently, uniaxial tensile tests were conducted and the average stress and strain were calculated from all the results obtained. Generally, the average stress-strain curve obtained had a different fracture trend as compared to the original stress-strain curves. This is because the average stress and strain values were obtained by adding point by point, where the author neglected the fact that there were large deviations for the strains at fracture for all the samples. Nevertheless, the average stress-strain curve was adopted for later modeling purpose because Molnar et al. (2012) believed that the average curve carried more complete information than only one

single curve.

Later, Mannarino and Rutledge (2012) investigated the mechanical properties of electrospun poly(trimethyl hexamethylene terephthalamide) (PA 6(3)T) mats before and after subjected to post treatment. In this work, post-spin thermal annealing was adopted to modify the initial properties of the electrospun PA 6(3)T nanofiber mats by placing the specimens into the oven for a duration of 2 hours at different temperatures, i.e. 130°C, 140°C, 150°C, 160°C and 170°C. Subsequently, uniaxial tensile tests were conducted on both treated and untreated specimens in order to investigate the effect of thermal treatment on the mechanical properties of the materials. Generally, it was observed that the yield stress, Young's modulus and wear resistance were improved through thermal treatment and increased as the applied temperature increased. From the morphological standpoint, thermal annealing changed the surface morphology of the electrospun materials, where an increase in annealing temperature led to the increase in inter-fiber fusion followed by the decrease in porosity. Therefore, it was believed that the increase in fiber junctions with annealing temperatures contributed to the improvement on the mechanical properties. Even though annealing at higher temperatures resulted in some improvement on the mechanical aspects, the loss of the original fiber morphology and porosity was undesirable for the purpose of real-life applications. Overall, the mechanical performance of the electrospun materials can be modestly improved without significant change in the fiber morphology by thermal annealing close to the relevant glass transition temperature. Concern has to be taken on maintaining the required fiber morphology for application purposes meanwhile ensuring a durable and robust performance in the service lifetime of the electrospun materials.

Besides, Choong et al. (2013) suggested that the electrospun materials are highly compressible due to their low relative density together with the flexible and small diameter fibers. It was claimed that the understanding on the compressive response of electrospun materials is critical, particularly for the applications where materials are constantly sub-

jected to high pressure operations such as the filtration application. Therefore, Choong et al. (2013) conducted uniaxial compression tests on electrospun bisphenol-A-polysulfone (PSU) and poly(trimethyl hexamethylene terephthalamide) (PA 6(3)T) mats thermally annealed at different temperatures, i.e. temperatures below and above the glass transition temperature of the two polymers. It was suggested that the mechanism of compression is mainly due to the fiber slippage, which occurs more readily in electrospun mats where fibers are not highly welded at inter-fiber junctions. The fiber slippage was described similarly to the dislocation motion in crystal where fibers can be reorganized during fiber slippage, forming stiffer and more compact structure, which is similar to the work hardening in metals. Subsequently, it was observed that thermal annealing at higher temperature increased the amount of welds at inter-fiber junctions similarly to the case reported in Mannarino and Rutledge (2012), which prevented fiber slippage in the electrospun materials.

A summary on the testing methods for single fibers and electrospun structures is presented in Table 2.2 for a better overview on the type of tests conducted in the literatures.

Table 2.2: Summary on the testing methods for single fibers and electrospun structures.

	Testing methods	Literatures
Single fibers	Atomic force microscopy (AFM)	Boffito et al., 2015; K. Y. Hwang et al., 2010; Mathew et al., 2005; E. P. S. Tan, Goh, et al., 2005; Yu et al., 2000
	Nano tensile tester	E. P. S. Tan, Ng, and Lim, 2005; Inai et al., 2005; Wong et al., 2008
	Nano-indentation	Wang et al., 2004; E. P. S. Tan and Lim, 2005
	Three point bend test	E. P. S. Tan and Lim, 2004
Electrospun structures	Uniaxial tensile test	Huang et al., 2004; Nerurkar et al., 2007; Molnar et al., 2012; Mannarino and Rutledge, 2012
	Uniaxial cyclic loading	Dupaix and Hosmer, 2010
	Uniaxial compression test	Choong et al., 2013

2.3.4 Poisson's ratio characterization

Poisson's ratio is commonly known as the ratio of transverse strain to axial strain, and it is one of the fundamental material properties that plays a significant role in structural design of products. Poisson's ratios of conventional isotropic bulk materials such as metals, elastomers, ceramics and composites have been thoroughly investigated, and their Poisson's ratio values are known to be in the range of 0 to 0.5. However, there are still many other classes of materials which possess different structural assemblies, such as woven and nonwoven fabrics. These materials, or more precisely known as structures, possess peculiar magnitude of Poisson's ratio which might be very distinctive from the conventional materials (De Jong, 1977).

The experimental and theoretical analyses of the Poisson's ratio of nonwoven fabrics were discussed in a few works (De Jong, 1977; Leaf & Kandil, 1980; Bais-Singh & Goswami, 1995; Sun et al., 2005). De Jong (1977) investigated the Poisson's ratio of woven fabric with different types of yarn, percentage of crimp as well as different types of weave, on the extension from two different directions (warp and weft directions). Results showed that the Poisson's ratio in both warp and weft directions were usually greater than unity. Subsequently, an equation was employed to determine the average Poisson's ratio of incompressible and inextensible yarns, by considering the crimps of yarns, degree of set and yarn extensibility. However, the overall theoretical values of Poisson's ratio computed were lower than the experimental values obtained. Later, Leaf and Kandil (1980) deduced an equation for fabric's initial Poisson's ratio by adopting the concept of incompressible and inextensible yarns, as in De Jong (1977).

Instead of purely predicting the values of Poisson's ratio, Bais-Singh and Goswami (1995) utilized the Poisson's ratio determined in predicting the mechanical response of spun-bonded nonwoven fabrics. The Poisson's ratio of spun-bonded nonwovens were first

determined through two different methods, i.e. uniaxial and biaxial tests. Subsequently, the results obtained were utilized in the theoretical prediction of fabric tensile properties. Generally, it was found that Poisson's ratio from biaxial tests predicted closer mechanical response to the experimental results.

More recently, Sun et al. (2005) developed a mechanical model for extensible yarns in order to predict the Poisson's ratio of the structure. The interactions between warp and weft yarns were considered during a theoretical analysis, and the results were further validated by comparing with the experimental data from Bao et al. (1997). It was found that the theoretical values of Poisson's ratio range approximately from 0.38 to 0.533 while the experimental values range from 0.2 to 0.57. The theoretical results were found to compare favorably with the experimental results from Bao et al. (1997). Besides, parametric studies were also conducted where parameters such as pick spacing ratio, yarn diameter ratio and yarn Young's modulus ratio were investigated by looking at the significance of their effect on the Poisson's ratio. It was observed that pick spacing ratio and yarn diameter ratio possess greater effects on the Poisson's ratio, as compared to the yarn Young's modulus ratio.

Apart from these, some other works investigating the in-plane Poisson's ratio of paper were also found in the literatures. Schulgasser (1983) suggested that the in-plane Poisson's ratio of paper made from chemical pulps is close to $1/3$. For this purpose, Schulgasser (1983) analyzed the Göttsching-Baumgarten Technique (Baumgarten & Göttsching, 1973) which was believed to be inaccurate, and proposed that minor modifications can be performed to make the technique a reliable and valuable one for the measurement of in-plane Poisson's ratio of very thin materials. Lately, Szewczyk (2008) determined the in-plane Poisson's ratio of paper by utilizing the propagation velocity measurement of ultrasonic waves. It was mentioned that measurement errors could be reduced through the use of this method.

Materials such as fabrics and papers were discussed since they share similar fundamental structures as the structure of interest, i.e. electrospun membranes. While the information on Poisson's ratio for most bulk materials is more or less established, the opposite is observed for structures such as composites and fabric membranes. The flexibilities of structures to be tailor-made open up the possibilities on their mechanical properties, including the magnitude of Poisson's ratio. However, the Poisson's ratio of electrospun membranes remains a myth to the researchers despite the numerous potential applications of electrospun membranes. This contributes to the difficulty in structural designing as there is a lack of information of the structures. To the best of our knowledge, there is still no investigation on the Poisson's ratio of electrospun membranes. Therefore, it is particularly important to have a better understanding on the Poisson's effect of the structures in order to have a deeper insight into its mechanical properties as well as to facilitate the development of a constitutive model.

2.4 Constitutive modeling of electrospun nanofibrous membranes

From the previous section, it is clear that the understanding of the mechanical response of electrospun nanofibrous membranes is crucial in order to facilitate the product design for various applications, as well as for the performance evaluation of these products during their service lifetime. However, until now, evaluation of the mechanical response still rely heavily on experimental characterizations, which are often daunting, costly and time consuming. Therefore, there is an urgent need for an alternative solution to reduce the dependency on the experiments. If a robust and cost-effective alternative method in evaluating the mechanical properties of electrospun nanofibrous materials through numerical simulation can be established, the strong dependence on experimental works can therefore be significantly reduced. Subsequently, the constitutive modeling of the mechanical response of electrospun nanofibrous membranes serves as the first step towards the path of

designing a robust numerical tool.

Generally, there are three main approaches for the constitutive modeling of materials. The first approach is known as the fundamental or micromechanics approach, which started by describing the microstructural behavior of the materials. Materials are assumed to be homogeneous and continuous at the macroscopic scale, and the macroscopic model can be obtained via averaging techniques, either analytically, or numerically with the use of a Representative Volume Element (RVE). The second approach is the phenomenological approach, where the macroscopic model is derived based on the observed phenomena from preliminary tests. Subsequently, calibration procedures are conducted to optimize the predictive capability of the model, mainly by comparison with experimental results or with micromechanical predictions on the appropriate RVE. This approach is more commonly used since the detailed description of the microstructures is not compulsory. The third approach which is the statistical approach is the least utilized and least fundamental approach. It is not so common and usually utilized for specific loading and environmental conditions (Runesson et al., 2006).

Even though a number of constitutive models were formulated for fabric materials (Jearanaisilawong, 2008; King et al., 2005; Nadler et al., 2006; Raina & Linder, 2014; Ridruejo et al., 2012; Shim et al., 1995), the modeling of electrospun nanofibrous membranes is still uncommon in the field of research. Often the demarcation of the approaches are blurred for the constitutive modeling of electrospun membranes because the microstructural morphology of the electrospun membranes can be easily assessed and understood, but the micro-mechanism of deformation is still difficult to be justified. Therefore, for the constitutive modeling of electrospun membranes, the phenomenological approach with appropriate description of the microstructures is often utilized, where it is often termed as “microstructurally-motivated model”. Among few attempts to model the mechanical behavior of electrospun nanofibrous membranes are discussed in the following sections.

2.4.1 Micromechanical model

Dupaix and Hosmer (2010) attempted to model the mechanical behavior of electrospun PCL by adopting the 8-chain rubber elasticity model by Arruda and Boyce (1993). The 8-chain model includes the assumptions of incompressibility, isotropy and hyperelasticity particularly for the description of rubber materials behavior. Dupaix and Hosmer (2010) realized that these assumptions do not ideally represent the behaviors of electrospun PCL due to three observations from the experiments: (1) electrospun PCL is not fully isotropic, (2) electrospun PCL is of high porosity and might be compressible, and (3) the time-dependent response observed cannot be reflected through this model. However, considering the simplicity of the model with only two material parameters, the 8-chain model was employed with slight modification to account for accumulated damage behavior observed from the experiments. Subsequently, the model was used to predict the cyclic loading responses of the electrospun PCL materials. Further comparison of the model with experimental data showed considerably good agreement at low strain regime, but a large deviation was observed in the regime of higher strains, where further improvement is needed to overcome the limitation of the model.

A micromechanical model was constructed by B. Yuan et al. (2011) to predict the elastic modulus of electrospun scaffold. The electrospun scaffold was assumed to be made of long straight fibers of uniform length and diameter, and only the individual segments between fiber crossings were considered for the deformation of the scaffold. Subsequently, fiber segments were categorized into long and short fiber segments, where during the deformation of scaffold, long fiber segments experienced stretching and bending deformation, while stretching and shearing deformation occurred on short fiber segments. Following this, B. Yuan et al. (2011) considered three parameters for the computation of overall elastic modulus of the electrospun scaffold, i.e. fiber orientation, fiber diameter and fiber concen-

tration. The model was established for 2-dimensional scaffold with oriented fibers, and the elastic modulus for two perpendicular directions could be computed through the proposed equations. However, comparison of the model prediction with published experimental data showed minor errors even though the general data trend could be captured. Further improvement needs to be done in order to improve the accuracy of the model as well as to extend the implication of the model so that the overall mechanical response of the electrospun scaffold can as well be predicted.

Lately, Wan et al. (2015) exploited the tensile relationship between individual nanofiber and the electrospun nanofibrous mat. For this purpose, a fiber geometry model was proposed employing a nonwoven unit cell. Through analysis, Wan et al. (2015) found that the tensile strength of an electrospun mat was determined by the ratio of width to length of the specimen, the mat porosity and the tensile strength of single nanofiber. The effects of porosity and width to length ratio on the resulting tensile strength of electrospun mat were simulated using the proposed model. Results suggested that increasing mat porosity as well as decreasing the width to length ratio decreased the tensile strength of electrospun mat due to the decreased fraction of nanofibers that are involved in resisting the tensile loading. Besides, the tensile strength of an individual nanofiber can also be easily predicted using the proposed model, provided that the width to length ratio and the mat porosity are known. Subsequently, real case experimental data was adopted for the prediction of the tensile strength of an individual fiber, and analysis results showed good agreement with the reported conclusion from the experimental work. Despite the good agreement shown, Wan et al. (2015) neglected the interaction between fibers in this work, which is also an important aspect that dictates the tensile strength of the electrospun mat.

2.4.2 Phenomenological model

De Vita et al. (2006) proposed a structural three-dimensional constitutive law for electrospun poly(butylene terephthalate) (PBT) nanofiber mats. In this work, the microstructural characteristic was taken into consideration for the computation of the macroscale mechanical properties of the electrospun structures. The model formulation was based on a few assumptions: (1) mechanical response of nanofibers mat is determined by the response of individual fiber, (2) inelastic behavior of the mat is due to the gradual failure of linear elastic fibers, (3) all fibers are straight and oriented along loading direction and (4) deformation of nanofibers mat is homogeneous, isochoric and axysymmetric. Subsequently, the model formulation followed the classical hyperelastic theory where strain energy function was adopted to compute the stress tensor. The strain energy function of the overall mat was assumed to be the summation of strain energies of the individual fibers, and stress-strain relation for individual fiber was proposed with three material parameters to be determined from curve fitting. Following this, model fitting with experimental data was conducted, and good agreement was obtained between the theoretical model and experimental results. In general, the model is potentially suitable for the prediction of the mechanical response of electrospun PBT mats, however, only the simplest uniaxial monotonic loading condition was successfully simulated and thus further validation of the model is required.

Silberstein et al. (2012) formulated a micromechanically-based constitutive model to capture the elastic-plastic behavior of randomly oriented electrospun mats. The model was constructed for two-dimensional non-woven network by taking into consideration the deformation mechanism of individual fibers, the fiber geometry and the connectivity of network. Along this, a triangulated network structure was adopted as the representative volume element (RVE); a double layer structure with one layer 30° off another was constructed and found to be sufficient to predict the macroscopic mechanical response of the electrospun

structure. The macroscopic constitutive model was developed based on the classical thermodynamic or strain energy framework, where the strain energy function per unit reference volume was defined as a function of deformation gradient tensor and other internal variables. Besides, the strain energy of the electrospun structure was assumed to be the summation of strain energies of the RVE members, similar to the practice in De Vita et al. (2006). Following this, the macroscopic nominal stress response is computed as the derivative of the strain energy function with respect to the deformation gradient tensor. At the fiber scale, Silberstein et al. (2012) proposed two different models, where: (1) fibers are straight initially and along deformation, and (2) fibers possess small initial curvature and subject to bending and stretching during axial loading. The implications of the two models were visualized through the RVE response of two triangulated layers under uniaxial extension. It was found that the second model which allowed bending of fibers enabled more significant transverse contraction of electrospun structure and the re-alignment of off-axis fibers towards the loading direction, which served as the important deformation mechanisms as observed through the SEM. Comparison was again conducted on the two models by simulating the true stress-strain responses of the full specimen and compared against the experimental data of electrospun polyamide mats. Again, it was found that the model with fiber bending was able to capture well the stress-strain response of the electrospun polyamide mat, while the model without fiber bending tended to overestimate the yield stress as well as underpredicted the post-yield strain hardening. Subsequently, the double-layer RVE-curved fiber model was employed for the simulation of the cyclic loading response and compared with experimental data, and good agreement was observed. In general, the constitutive model proposed possesses good predictive capability on the mechanical response of electrospun polyamide. It was also believed that the model is transferable to other electrospun or non-woven materials.

The unique microstructural characteristic of electrospun scaffold serves a potential

structure for the tissue engineering application, particularly for cell proliferation and growth. Along this, electrospun tubular scaffold is one of the interested structure replicating the helical organization in native arteries. Recently, Hu (2015) attempted to model the biaxial deformation of electrospun tubular scaffold with the use of hyperelastic constitutive equations. Electrospun tubular scaffolds were made by stacking two electrospun mats with same fiber orientation in an opposite manner to form an axisymmetric membrane, followed by wrapping the membrane around a mandrel to form the desired tubular shape. The author considered tubular scaffold of moderately and highly aligned fibers with different off-axis angles (30° , 45° and 60°), resulting in a total of six specimen types. In this work, two different types of models were considered: (1) phenomenological model and (2) structurally-motivated model. For the former case, strain energy function was adopted from Fung (1990); whereas for the latter case, the macroscopic strain energy function was taken as the summation of strain energies of individual fibers (similar with previously reported works of De Vita et al. (2006) and Silberstein et al. (2012)). Furthermore, for structurally motivated model, two forms of responses (linear and nonlinear) for individual fibers were utilized to determine the effect of each on the macroscopic mechanical behavior of the scaffold. Subsequently, a Neo-Hookean strain energy function was added to both (linear and nonlinear strain energy functions) for further investigations. Additionally, the structurally-motivated model with nonlinear response and Neo-Hookean strain energy functions was further amended to prescribe the dispersion of fiber orientation. Overall, a total of six different models were employed, with one phenomenological model and five structurally-motivated models. All these models were fitted to the experimental biaxial stress-stretch data of electrospun polycaprolactone (PCL) from the six specimen type mentioned earlier. In general, the phenomenological model from Fung (1990) produced the best fitting results among all. However, the author considered the importance of physical significance and suggested that the structurally-motivated model was more suitable and will provide

greater advantage for the scaffold design. For this purpose, the predictive capability of the structurally-motivated model has to be further improved for higher accuracy or reproducibility.

Despite the insufficient information on the modeling of electrospun structures, some similar works that can serve as references were found for different types of materials, i.e. for fiber-reinforced composites by Planas et al. (2007) and for nonwoven geotextiles by Ridruejo et al. (2012). Both of the works were initiated from the mechanical behaviors at the fiber scale and extended to the macroscopic responses by means of the representative element technique. For the case of randomly oriented electrospun structures, fibers were said to deform accordingly to their orientations with respect to the specimen's loading axis. Thus, fibers from different orientations undergo different magnitudes of deformation when uniaxial tensile loading was applied at the macroscopic scale. This assumption of fiber re-orientation was also applied in both Planas et al. (2007) and Ridruejo et al. (2012). Planas et al. (2007) utilized a unit sphere to compute the stress from the distribution of microfibrils, and the developed continuum model for fiber-reinforced material was further implemented for the modeling of biological silk fibers. The proposed model was able to capture the uniaxial monotonic tensile behaviors and the degree of orientation of spider silk fibers with different initial alignments. Whereas in Ridruejo et al. (2012), the two-dimensional mechanical behavior of nonwoven mats was modeled by assuming an in-plane mechanical deformation. In this work, a square planar region was adopted as the reference configuration and fiber orientation was assumed to vary only in the plane. In addition to the elastic-plastic behavior as in Planas et al. (2007), damage was also included in the constitutive model of Ridruejo et al. (2012) to capture the progressive drops of the stress level in the macroscopic mechanical behavior of polypropylene nonwoven felt. The model was said to accurately reproduce the main deformation as well as the fracture and damage mechanisms of the nonwoven fabrics.

2.4.3 Statistical model

The relationship between fiber assembly and the macroscopic mechanical behavior of the electrospun structures was explored by Rizvi et al. (2012). A theoretical model was developed based on a few assumptions: (1) most of the fibers were curved in their initial states, (2) there was no fusion between fibers (no inter-fiber junction), (3) inter-fiber friction is negligibly small and (4) only fibers that span the entire fibrous structure longitudinally can bear the applied tensile load. Subsequently, the mechanism of deformation was proposed such that during the elongation of the electrospun structures, the curved fiber was first straighten and then followed by the resistance of the straighten fiber to the applied tensile load, until the fracture of the fiber. Therefore, at any specific strain level, the mechanical strength of the electrospun structures was provided only by a fraction of fibers that were straighten and stretched. Along this, Rizvi et al. (2012) classified fibers into two main categories: (1) load-bearing fibers (straight fibers) and (2) non-load bearing fibers (curved intact fibers and broken fibers). Eventually, the total resistance force of the electrospun structure can be computed through the summation of resisting forces from all load-bearing fibers, which also depended on the total number of fibers that span the entire fibrous structure longitudinally. Subsequently, comparison between the proposed model and experimental results was conducted, where qualitatively good agreement was observed. Besides, parametric studies were also conducted to have a deeper insight into the significance of each material parameter. Even though the proposed model was well explained by Rizvi et al. (2012), this work did not take into consideration the re-orientation of the fibers along the direction of the applied stress, which might later contribute to the mechanical strength of the fibrous structure, once the fibers are re-oriented along the tensile direction.

2.4.4 Modeling software

Molnar et al. (2012) modeled the tensile behavior of an electrospun PA-6 nanofibrous mat and estimated the tensile strength of a single PA-6 nanofiber through the modeling results, by using the FiberSpace software. In this work, the theory of fiber bundle cells (FBC) was adopted where it was proposed that different types of FBCs existed in the mat structure, such as the slipping fibers, oblique fibers and straight fibers which gave rise to different deformation mechanism of the electrospun mat. The proposed model was fitted with an average stress-strain curve obtained through averaging a number of experimental data, and good agreement was shown through the curve fitting. Moreover, the fraction of each bundle type was also computed and it was found that the fraction of slipping fibers was the highest, followed by oblique fibers and lastly straight fibers. Therefore, Molnar et al. (2012) suggested that the breaking of inter-fiber bonds and slippage of fibers dominated the deformation mechanisms in electrospun PA-6 mat. Finally, the theoretical tensile strength of single PA-6 nanofiber was determined from the modeling results, suggesting a value of 48% higher than that of the bulk material. This value was validated by comparing with the experimental results obtained in K. Y. Hwang et al. (2010) through the use of AFM. Consequently, Molnar et al. (2012) postulated that the tensile properties of single nanofibers can be computed even in the absence of costly device, e.g. AFM.

Generally, most of the constitutive models proposed for electrospun structures belong to the category of structurally-motivated models where the microstructure of the electrospun membrane is considered for the model formulation. Unlike purely phenomenological models, structurally-motivated models possess physical significance which is more useful for material design in real-life applications. However, most of the existing models for electrospun membranes examined only the predictive capability on basic mechanical responses such as uniaxial monotonic loading (except for Silberstein et al. (2012) and Hu (2015)).

More complex mechanical responses should be taken into consideration in order to produce a comprehensive constitutive model that is capable to predict not only simple but also complex mechanical responses such as a series of loading and unloadings or biaxial deformations, that are more likely to represent the conditions in real-life applications. A summary on the modeling approaches is presented in Table 2.3.

Table 2.3: Summary on the modeling approaches for electrospun structures.

Approaches	Prediction of...	Literatures
Micromechanical model	Uniaxial cyclic loading	Dupaix and Hosmer (2010)
	Elastic modulus	B. Yuan et al. (2011)
	Tensile strength of individual nanofibers	Wan et al. (2015)
Phenomenological model	Uniaxial monotonic loading	De Vita et al. (2006); Silberstein et al. (2012)
	Uniaxial cyclic loading	Silberstein et al. (2012)
	Biaxial loading	Hu et al. (2015)
Statistical model	Uniaxial monotonic loading	Rizvi et al. (2012)
Modeling software (FiberSpace)	Uniaxial monotonic loading	Molnar et al. (2012)

2.5 Potential applications of electrospun nanofibrous membranes

The rapid emergence of nanotechnology has driven the worldwide interest towards the fabrication of the nanomaterials as well as to apply those materials for real life applications, due to their improved properties as compared to their bulk counterparts. Among these, nanofibrous membranes or nanofibrous mats are widely investigated owing to their novel physical properties such as high surface area to volume ratio, high porosity with narrow pore size distribution, interconnected open pores as well as its high water flux and permeability to gases. Subsequently, these highly desirable features of electrospun nanofibrous membranes

promote investigations for a number of potential applications, such as filtration, distillation, separation, textiles, tissue engineering and drug delivery fields.

The outstanding properties of electrospun membranes such as high surface area to volume ratio, low air resistance, low density and its physically and chemically modifying flexibility provide exceptional advantages for the application of filtration. One of the biggest advantages of using electrospun membranes is that the physical properties of the membrane such as the fiber diameters and pore sizes could be easily modified during fabrication to adapt for different types of filtration purposes. Furthermore, the ultrathin fibers in the nano-scale improve the surface adhesion properties due to the increase in fibers' surface area which further increase the efficiency of capturing the filtration particles as compared to the use of larger size fibers. Until now, electrospun nanofibrous membranes have been widely investigated for air cleaning in clean rooms as well as aerosol filtrations for industrial purposes. It is known that the aerosol particles are filtered through the electrostatic attractions between the filter and the aerosol particles. Thus, the existence of static charges in the electrospun materials that are developed during the electrospinning process improves the efficiency of the filtration when electrospun membranes are utilized as aerosol filters (Baji et al., 2010). Moreover, electrospun membranes have a longer filter life due to their nanofiber efficiency layer and surface loading characteristics which greatly reduce the cost of operation for industrial usages. Further improvement of electrospun materials for filtration applications is possible through the use of chemically selective materials and to induce permanent charges on the electrospun materials, e.g. through corona polarization or triboelectric polarization methods (Greiner & Wendorff, 2007).

The use of electrospun nanofibers in textile industry has been widely studied especially for the protective clothing systems. Indeed, the fabricated nanofibers can be used in combination with conventional textile materials in order to improve the overall properties of the products. Generally, the addition of nanofibers to the traditional textiles aims

to improve the air resistance, thermal insulation, water vapour permeability or the barrier performance of the materials towards unwanted particles. Nanofiber nonwovens possess reduced pore dimensions with increased inner surface area as compared to the conventional nonwovens. These properties allow for better air or wind resistance which in turn contribute to an improved thermal insulation. According to Greiner and Wendorff (2007), the airflow resistance increases by three orders of magnitude for nanofiber nonwovens in comparison to the conventional textiles. The improved thermal insulation is mainly due to the decreased pore sizes which limit the diffusion of air molecules into the materials. Lately, the health hazards in agriculture becomes an emerging issue where people realizes the needs of protecting the agricultural workers from harmful particles due to the unsanitary conditions, pesticides and many others. S. Lee and Obendorf (2007) focused on the investigation of an electrospun nanofiber web as liquid penetration barriers in protective clothing for agricultural workers. They studied the incorporation of different densities of the electrospun nanofiber web into a layered fabric system and assessed the protection and comfort performances of the whole material. It was found that the barrier performance was greatly improved even though only a very thin layer of nanofiber web was incorporated. Besides, the air permeability was found to decrease with increasing nanofiber web density, but still the overall comfort performance is better than many current protective clothing materials which are highly impermeable to air.

Apart from that, electrospun nanofibrous materials possess potential usages in biomedical applications, particularly for tissue engineering, wound dressing and drug delivery. The biocompatible ultrafine fibers produced by electrospinning have gain increasing attention for the tissue engineering applications. Subsequently, the flexibility in controlling the scaffold properties in the electrospinning process extends the possible usages of the nanofibrous membranes for different tissue applications, including vascular, cartilage, bone, neural, skin tissues, lung tissues and etc. (Greiner & Wendorff, 2007; Sill & von Recum,

2008). The characteristics of electrospun nanofibrous membranes such as high surface area to volume ratio and high porosity make the materials highly suitable to be used as scaffolds or mimicking the function of the extracellular matrix (ECM) for the seeding of stem cells or human body cells. Basically, the function of the engineering scaffolds or matrices is to facilitate the anchorage, migration and proliferation of the cells in order to reproduce the three-dimensional structure of the desired tissue (Greiner & Wendorff, 2007). Experimental studies suggest that the fiber architecture affects greatly on the growth of the cells, in which the degree of porosity and pore dimensions of the membranes play significant roles for the cell proliferation and the formation of three-dimensional tissues. Besides, the biocompatibility of a material is said to be improved with decreasing fiber diameter (Holzwarth & Ma, 2011). All these properties can be easily controlled through the use of electrospun membranes. Another advantage of using electrospun nanofibrous membranes for tissue engineering is that highly aligned fibers can be fabricated for applications that require anisotropic properties, such as the seeding of musculoskeletal tissues and annulus fibrosus of the intervertebral disc (Nerurkar et al., 2007). In this case, the cells grow following the orientation of the fibers and it was reported that the production of tissue is greater when oriented scaffolds or matrices are employed (C. H. Lee et al., 2005). Moreover, highly oriented membranes provide sufficient mechanical strength when the cultured tissues are desired for load-bearing function. Therefore, the investigation of the mechanical properties of the electrospun materials is always crucial as mentioned earlier.

Meanwhile, electrospun materials for wound dressing or wound healing have been investigated since the last decade. For this purpose, biodegradable polymers are often utilized to produce a thin layer of nanofibers for covering the wound. It was found that such nanofibrous layer provides sufficient pores for liquid and gas exchange but at the meantime preventing the entering of bacteria due to the confined pore dimensions. Electrospun mats was found to adhere very well on the moist wounds and facilitate the healing process as com-

pared to the conventional wound treatment (Venugopal & Ramakrishna, 2005). Moreover, appropriate drugs can be incorporated into the fibers during electrospinning and released into the wounds for antiseptics and antibiotics effects for wound healing purpose. Some promising materials for wound dressing or wound healing include polyurethane, collagen, silk fibroin, poly(ϵ -caprolactone) and polylactic acid (Greiner & Wendorff, 2007).

Another important potential biomedical application of electrospun materials is the drug delivery for living organisms. A number of drugs can be delivered through the use of electrospun materials, such as antibiotics, anticancer drugs, anti-inflammatory drugs, proteins and DNA. Various methods were proposed for the drugs loading: coating, embedding or encapsulating in order to control the drug release kinetics in the human body (Pillay et al., 2013; Sill & von Recum, 2008). Generally, the desired drugs can be dissolved into the polymer solution to be electrospun or the two solutions (polymer solution and drug solution) can be blended for the electrospinning process in the case where the drugs are insoluble in the polymer solvent. Besides, another approach of drug loading is through the immersion of electrospun membrane into the drug solutions so that the drug particles can be absorbed into the nanofibers by diffusion (Pillay et al., 2013). Subsequently, drugs release from the nanofibers to the body through the diffusion mechanism or the degradation of biodegradable nanofibers. Indeed, biodegradable materials are preferable since no explanation is needed. However, due to the complexity of the drug release mechanisms, special attention is needed when tailoring the incorporated dose of drugs as well as the release and degradation rates, in order to avoid excessive dose dumping which causes toxicity in the human body (Sill & von Recum, 2008). In general, by understanding the diffusion and degradation mechanisms of the drugs and the nanofibers respectively, the drug release kinetics could be modulated by manipulating the properties of the nanofibers such as the fiber diameters, pore distributions, fiber alignment, fiber densities etc. (Pillay et al., 2013).

2.6 Polyvinylidene fluoride (PVDF)

In this work, PVDF is chosen as the material of interest for the fabrication of electrospun nanofibrous membranes. Therefore, this section aims to discuss thoroughly on the general characteristics of PVDF, the electrospinning of PVDF, as well as the mechanical characterization and potential applications of electrospun PVDF membranes.

2.6.1 Introduction of PVDF

Over the years, PVDF has been widely studied due to its outstanding properties which are suitable for a wide range of applications. PVDF is a pure thermoplastic fluoropolymer formed by the polymerization of 1,1-difluoroethylene. The alternating CH₂ and CF₂ groups in PVDF contribute to its polarity which results in its selective solubility and good electrical properties (Figure 2.7). PVDF has a density of 1.78 g/cm³, a melting point of around 177 °C and a glass transition temperature of about -35 °C. The degree of crystallinity of PVDF ranges between 35% and 75% (Liu et al., 2011). PVDF is easily dissolved in common organic solvents, which makes its use preferable over other polymeric materials.

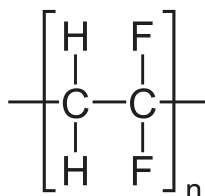


Figure 2.7: Monomer of poly(vinylidene fluoride) (Retrieved January 2, 2018, from https://en.wikipedia.org/wiki/Polyvinylidene_fluoride)

The excellent thermal stability of PVDF is one of its outstanding properties which makes PVDF a popular polymer for the industry. According to Liu et al. (2011), fluorine atoms on the polymer chain possess high electronegativity which contribute to the high dissociation energy of carbon-fluorine bond, providing high stability to the material.

Besides of its excellent thermal stability, PVDF membranes have an excellent chemical stability against a wide range of harsh chemicals such as acids, strong oxidants and many

organic solvents (Benzinger et al., 1980). This characteristic contributes to its popularity in many industrial applications where the material is frequently exposed to strong acidic or alkaline solution, or subjected to regular chemical cleaning.

Due to its superior properties, PVDF has been widely used in many engineering applications such as wastewater treatment, gas separation, membrane distillation, pollutants removal, separators for rechargeable batteries, etc. PVDF is also a suitable candidate in biomedical and bio-separation applications due to its biocompatibility (Liu et al., 2011). Owing to its high mechanical, thermal and chemical stabilities, Choi et al. (2004) and K. Hwang et al. (2011) made PVDF as the desired candidate for their research in the application of battery separators.

2.6.2 Electrospinning of PVDF

The electrospinning of PVDF membranes has been thoroughly investigated in the recent years. Most emphasizes were given on the influences of the electrospinning parameters on the resulting morphology of the PVDF nanofibrous membranes (Cozza et al., 2013; Gao et al., 2006; Liao et al., 2013; Zhao et al., 2005). As mentioned earlier, optimization of electrospinning parameters is important in order to produce desired nanofibers with smallest fiber diameter possible and free from beads.

Zhao et al. (2005) investigated the effects of polymer concentration, amount of solvent and the capillary-collector distance on the morphology of the fabricated PVDF nanofibrous membranes. In this work, a co-solvent (N,N-dimethylformamide (DMF) and acetone) was used with DMF as the main solvent to dissolve the PVDF polymer. Subsequently, the polymer solution properties such as viscosity, surface tension and conductivity were also measured. It was found that the addition of acetone promoted the formation of uniform ultrafine fibers as compared with the use of DMF as solvent alone. Besides, the amount of beads and beaded-fibers were found to decrease when the polymer concentration was

increased to an appropriate level. Meanwhile, no visible difference was observed when changing the capillary-collector distance from 10 cm to 15 cm and to 20 cm. However, the 15 cm distance was said to produce the most uniform fiber morphology among the three despite the differences were insignificant. As a summary, by using the optimum parameters of 15 wt% PVDF polymer with 8:2 ratio of DMF to acetone at the applied voltage of 5 kV, flow rate of 0.3 ml/h and capillary-collector distance of 15 cm, uniform fiber morphology with nano-sized fibers of the PVDF electrospun nanofibrous membrane can be obtained.

Gao et al. (2006) investigated the relationship between the applied voltage and average fiber diameter with other electrospinning parameters kept constant. It was found that finer fibers could be obtained by increasing the applied voltage for electrospinning. The formation of finer fibers was due to the increased electric field that brought about the stretching and acceleration of the polymer jets. Later, Chanunpanich et al. (2008) utilized a different main solvent as compared to Zhao et al. (2005) and Gao et al. (2006) for dissolving the PVDF powder. N,N-dimethylacetamide (DMAc) and acetone in the ratio of 3:7 was adopted for the preparation of the PVDF polymer solution. In this work, applied voltage, flow rate and capillary-collector distance were manipulated to determine the effects of these electrospinning parameters on the produced fibers. It was reported that no significant change in the fiber diameters were observed by changing the processing conditions, instead the diameters distribution was affected. Higher voltage, capillary-collector distance and flow rate were said to result in narrow fiber diameters distribution.

Until now, most of the works focus on the main parameters such as polymer concentration, solvent selection, applied voltage, flow rate and capillary-collector distance. The ambient parameters such as humidity, airflow and surrounding temperature were usually neglected due to the difficulty in manipulation. Cozza et al. (2013) assessed the influence of polymer concentration, solvent mixture, applied voltage as well as the airflow and relative humidity of the surrounding environment on the nanofibers morphology. As

usual, increasing polymer concentration was found to decrease the amount of bead defects, while optimum voltage and flow rate were highly dependent on the polymer system used. Subsequently, it was demonstrated that the two ambient parameters that were always neglected play important roles in determining the final morphology of the electrospun nanofibers. Higher airflow with proper solvent promoted homogeneous and defect-free nanofibers, while increasing relative humidity increased the uniformity of the nanofibers. Finally, Cozza et al. (2013) suggested that the optimum parameters for the electrospinning of PVDF nanofibrous membranes are 15 wt% PVDF polymer concentration, DMF/acetone of ratio 7 to 3, applied voltage of 20 kV, flow rate of 0.003 mL/min, airflow of 3.5 L/min and the relative humidity of 50%.

2.6.3 Mechanical characterization of electrospun PVDF membranes

Due to the difficulty in specimen handling and the fragility of the electrospun materials, only a few studies were conducted on the basic mechanical properties of electrospun PVDF nanofibrous membranes, such as tensile strength, elastic modulus and elongation at fracture that are commonly obtained through simple monotonic uniaxial tensile tests (Choi et al., 2004; Gao et al., 2006; K. Hwang et al., 2011; Zhao et al., 2005).

Choi et al. (2004) investigated the tensile strength of electrospun PVDF membranes before and after thermal treatment. The tensile strength, tensile modulus and elongation at break were improved significantly by the thermal treatment. It was explained that the thermal treatment led to a thicker fiber diameter, an increase in crystallinity and to the formation of interfiber bonds. Subsequently, larger fiber diameter promoted better tensile strength and higher elongation before break, higher crystallinity improved the tensile modulus of the material, while increased in interfiber bonds improved the rigidity of the whole material and leads to a change in shape of the stress-strain curve as compared to the untreated sample.

Later, Zhao et al. (2005) produced highly aligned PVDF nanofibrous membranes through

electrospinning and investigated the tensile properties of the membranes in two different directions, i.e. the revolving direction (direction of fiber alignment) and the cross direction (direction perpendicular to the fiber alignment). Monotonic uniaxial tensile tests suggested that no significant difference in the tensile behaviors between the revolving direction and the cross direction. Zhao et al. (2005) then summarized that there is no relationship between the tensile properties and the fiber orientation for the highly oriented electrospun PVDF nanofibrous membrane. However, this finding contradicted with the common theory that the electrospun membranes are always stronger in the fiber direction due to the ability of the fibers to resist stretching, since nothing holds the fibers together in the perpendicular direction (Nerurkar et al., 2007).

Besides, Gao et al. (2006) conducted monotonic uniaxial tensile tests for three different types of electrospun PVDF specimens, i.e. untreated electrospun PVDF membranes, thermally treated electrospun PVDF membranes and cast PVDF membranes and the tensile properties were compared and discussed. It was observed that cast PVDF membrane has the highest tensile strength but least ductile with lowest elongation at break. Meanwhile, the thermally treated electrospun PVDF membrane has much better tensile properties with higher tensile strength and modulus but lower elongation at break as compared to the untreated electrospun PVDF specimens. This finding coincides with that of Choi et al. (2004) where thermal treatment was said to improve the tensile properties of the materials. Gao et al. (2006) mentioned two factors that contributed to the lower tensile strength of untreated electrospun PVDF membrane: (1) the absent of interfiber bonds and (2) its lower density which is only one-third of the casting PVDF membrane. Besides, it was examined that electrospun PVDF membranes with smaller average fiber diameter exhibited better tensile strength and modulus, and similar phenomena were also reported later in Wong et al. (2008) and Baji et al. (2010).

In recent years, K. Hwang et al. (2011) investigated the PVDF nanofibrous membranes

for the use as secondary battery separators. Thus, the tensile strength of electrospun PVDF nanofiber separators was compared with the commercial polyethylene (PE) separator and a PVDF film prepared through phase inversion method. Tensile tests demonstrated that the PVDF nanofiber separators exhibited better tensile properties than the PVDF film separators, while in terms of elongation, all PVDF nanofiber separators showed higher values than that of commercial PE as well as PVDF film. Subsequently, it was summarized that electrospun PVDF nanofiber material served as potential candidate for replacing the commercial PE as battery separators due to its outstanding mechanical properties.

Until now, most of the research works focused only on the basic mechanical properties of the electrospun membranes, such as tensile strength, elastic modulus and elongation at fracture, which are commonly obtained through monotonic uniaxial tensile tests. Therefore, the understanding of the material's mechanical behavior under more complex loading conditions is crucial and more experimental works have to be conducted in order to have a clearer idea on the deformation mechanisms of the electrospun nanofibrous materials.

2.6.4 Potential applications of electrospun PVDF nanofibrous membranes

Over the years, electrospun PVDF nanofibrous membranes have been widely investigated for the use as secondary battery separators as well as for the filtration applications. The excellent thermal stability and chemical resistance of PVDF makes it highly suitable for these applications (Choi et al., 2004; Gao et al., 2006; K. Hwang et al., 2011).

Choi et al. (2004) studied the use of electrospun PVDF nanofibrous membranes as polymer electrolyte or separator. The PVDF nanofiber mat was fabricated and thermally treated to improve the physical properties of the material. Subsequently, a PE layer was introduced onto the surface of the PVDF nanofiber mat for the nanofiber mat to function as a separator with shutter. Apart from that, Gao et al. (2006) also investigated the applicability of electrospun PVDF nanofibrous membranes as separator for rechargeable lithium metal

cells. It was found that electrospun PVDF mats possessed better affinity to the lithium metal and thus retaining the electrolyte ability and promoted lower inter-resistance in the cells. Moreover, the electrospun PVDF mat was showed to possess better cycling ability and charge-discharge performance with only little loss of capacity when comparison was made with the commercial separator (polypropylene separator). This statement was again verified in K. Hwang et al. (2011) where PVDF nanofiber separators were said to exhibit excellent cyclic fading and discharge rates.

Besides, the electrospun PVDF materials also work well for filtration and distillation applications. Gopal et al. (2006) investigated the potential of electrospun PVDF membranes for filtration application, particularly for micro-particle separation. A simple model was developed employing polystyrene (PS) as the particles to be separated. The electrospun PVDF membranes were said to have a great potential in filtrating micro-particles in the range of 5 to 10 μm without damaging the PVDF membranes. Further findings suggested that the electrospun PVDF membranes were able to filter more than 90% of the unwanted PS particles from the solution.

The application of electrospun PVDF membranes for direct contact membrane distillation was studied by Liao et al. (2013). Electrospun PVDF membranes were fabricated using different sets of material parameters in order to obtain a most suitable fiber morphology for the purpose of membrane distillation application. Thermal treatment was imposed on some of the electrospun PVDF membranes and the membrane distillation performance was evaluated on both treated and untreated samples. It was found that the heat-press treatment greatly enhanced the permeation flux, reducing the pore wetting and porosity of the membranes. Moreover, comparison with the commercial PVDF membranes showed better water permeation flux, suggesting the great potential of electrospun PVDF membranes for the direct contact membrane distillation (DCMD) applications (Liao et al., 2013).

2.7 Summary of literature review

Generally, the investigations of electrospun structures have been highly focused on the manipulation of chemical content and physical properties, in order to produce structures with good functionalities for various purposes. Thus, the fabrication of electrospun structures is more or less established, where structures of desired properties can be tailor-made through the manipulation of electrospinning parameters. Nevertheless, the mechanical responses and constitutive modeling of electrospun structures are still fresh to be explored.

From the literatures, most of the mechanical characterization for electrospun structures focused only on the investigation of basic mechanical properties, and complex mechanical responses are often neglected. Additionally, there is no information found on the Poisson's ratio of electrospun structures, despite the importance of this properties for structural or product design. Moreover, in constitutive modeling, most of the existing models for electrospun membranes examined only the predictive capability of the basic mechanical response such as uniaxial monotonic loading, with less concern to complex mechanical responses that are more likely to represent the conditions in real-life applications. All these remarks will be addressed in the present work in order to have a more comprehensive investigation as well as to fully understand the behaviors of electrospun structures.

CHAPTER 3: METHODOLOGY

Generally, the present work is divided into two main parts, i.e. experimental part and constitutive modeling part. The first part of the work emphasizes on the mechanical characterization and fiber orientation analysis of the electrospun nanofibrous membranes. For this purpose, electrospun nanofibrous membranes are fabricated by manipulating two different electrospinning parameters, i.e. polymer concentration and applied voltage. Subsequently, the surface morphologies of the fabricated membranes are analyzed in order to choose one representative sample with the most desired morphology for further characterizations, i.e. mechanical characterization and fiber orientation analysis.

The second part of the work focuses on the development of a constitutive model that is able to predict the mechanical responses of the electrospun nanofibrous membranes, based on the observations from experimental findings. The corresponding constitutive equations are derived based on the hyperelastic theory commonly employed for the case of elastomeric materials. Following this, the efficiency of the proposed model will be assessed using experimental data obtained from the first part of the work. Finally, the predictive capability of the model will be further evaluated through the simulation of other deformation modes. A flowchart summarizing the research flow is presented in Figure 3.1.

3.1 Fabrication of PVDF membranes

The fabrication of PVDF membranes is important in order to provide appropriate structures for a series of characterizations. The results from characterizations will be useful for the constitutive modeling of the mechanical responses of electrospun nanofibrous membranes.

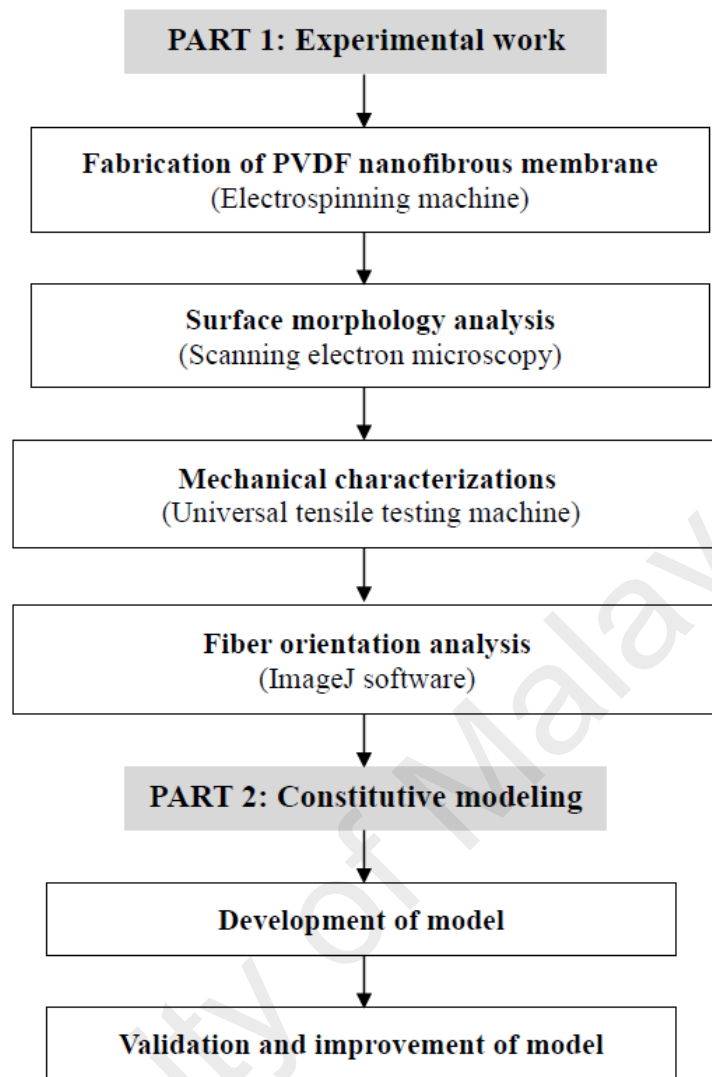


Figure 3.1: Research methodology flowchart.

3.1.1 Materials

Polyvinylidene fluoride (PVDF) powder from Sigma Aldrich with an average molecular weight of 534,000 g/mol was utilized as the precursor material for the electrospun membrane fabrication. Meanwhile, a co-solvent system was adopted where N,N-dimethylformamide (DMF) from Ajax Finechem Pty. Ltd. and acetone from R&M Chemicals were utilized in an appropriate proportion for the preparation of the PVDF polymer solution.

3.1.2 Electrospinning machine

In this research, the electrospinning machine plays a major role for the fabrication of PVDF nanofibrous membranes. In general, a high voltage is applied on the polymer

solution to produce continuously a charged jet of fibers which are deposited on a stationary electrically grounded collector. The electrospinning machine allows the manipulation of the electrospinning parameters such as voltage, feed rate, capillary-collector distance, as well as the revolution per minute when a rotating collector is in used. These parameters are the key factors in determining the final morphology of the electrospun nanofibrous membrane. For this research, the Electroris labscale electrospinning unit was employed for the electrospinning processes. An electrospinning setup is shown in Figure 3.2 for the purpose of illustration.



Figure 3.2: An electrospinning setup.

3.1.3 Preparation of PVDF polymer solution

For the fabrication of PVDF nanofibrous membranes, only two experimental parameters were manipulated, i.e. PVDF polymer concentration and the applied voltage during electrospinning. Two different PVDF polymer concentrations were adopted, i.e. 13 and 15 weight percentages (wt.%) while three different applied voltages were investigated for each polymeric concentrations, i.e. 10 kV, 15 kV and 20 kV. Other electrospinning parameters including solvents ratio, capillary-collector distance and feed rate were kept constant for all the fabrication processes. Solvents ratio for DMF: Acetone was fixed at 7:3, while a capillary-collector distance of 15 cm and feed rate of 0.5 ml/h were employed for the en-

tire investigation. Subsequently, the PVDF polymer solutions were prepared through the following steps:

1. Firstly, PVDF powder, DMF and acetone of desired amount were calculated and measured by means of an electronic weighing balance. On the basis of 10 g polymer solution, the calculated amount of each of the chemicals were tabulated in Table 3.1.
2. Next, the PVDF polymer solution was prepared by mixing the PVDF powder and DMF solvent in a boiling flask. The mixture was stirred on a digital hotplate stirrer at the speed of 600 rpm and temperature of 70 °C. The temperature was kept around halves of the boiling point of DMF to avoid solvent evaporation meanwhile providing a heating effect that facilitated the dissolution process. Moreover, the mixture was subjected to continuous stirring for 24 hours, to ensure the complete dissolution of PVDF powder in DMF solvent.
3. Later, acetone was added to the PVDF-DMF mixture and the solution was stirred again for another 24 hours at 600 rpm, but with a lower temperature of 25 °C.
4. The PVDF polymer solution was subsequently inserted into a 10 ml syringe to prepare for the electrospinning process.
5. Process 1 – 4 were repeated for the preparation of PVDF polymer solutions of different concentrations.

Remark 1. *Adopted from Cozza et al. (2013), this technique of solution preparation that requires long term stirring processes ensures polymer and solvents to be incorporated thoroughly.*

Table 3.1: Amount of PVDF, DMF and acetone used for the preparation of 13 wt.% and 15 wt.% PVDF polymer solution.

Weight percentage of PVDF	13 wt.%	15 wt.%
Amount of PVDF (g)	1.3	1.5
Amount of DMF (g)	6.09	5.95
Amount of Acetone (g)	2.61	2.55

3.1.4 Electrospinning of PVDF nanofibrous membranes

Generally, two electrospinning parameters, i.e. polymer concentrations and applied voltage were varied for the fabrication of PVDF nanofibrous membranes. All other parameters were kept constant for the entire fabrication processes. The electrospinning of PVDF nanofibrous membranes was conducted as follows:

1. PVDF polymer solution was inserted into a 10 ml syringe which acted as the solution reservoir. The syringe was positioned upside down, allowing air bubbles to be collected and removed through the tip of the syringe.
2. A stainless steel needle was cut short (10 mm) and attached to the syringe as the capillary tip.
3. The syringe containing PVDF polymer solution was subsequently inserted onto the syringe pump of the electrospinning machine.
4. The metallic capillary was then connected to the high voltage power supply, which can generate DC voltage up to 35 kV.
5. A piece of aluminium foil was attached to the stationary grounded collector for fiber deposition, meanwhile allowing the easy removal of the nanofibrous membrane for further characterization tests.
6. Then, the desired parameters for the electrospinning process were set onto the electrospinning machine, with the following values for the parameters:

- a) Feed rate: 0.5 ml/h
 - b) Capillary-to-collector distance: 150 mm
 - c) Electrospinning duration: 10 hours
7. The electrospinning process was started by pressing the “Run” button and the voltage of 10 kV was immediately adjusted.
8. Steps 1 – 7 were repeated with voltages of 15 kV and 20 kV.
9. Subsequently, steps 1 – 8 were repeated by utilizing the polymer solutions with different polymer concentration.

Overall, six samples of PVDF membranes were fabricated utilizing different sets of material parameters, and the samples were labeled according to their corresponding weight percentages and voltages, as tabulated in Table 3.2.

Table 3.2: Six samples of electrospun PVDF membranes with their corresponding parameters.

Sample	Polymer concentration (wt.%)	Voltage (kV)	Ratio of DMF : Acetone	Feed rate (ml/h)	Capillary-collector distance (mm)
P ₁₃ V ₁₀	13	10	7:3	0.5	150
P ₁₃ V ₁₅	13	15	7:3	0.5	150
P ₁₃ V ₂₀	13	20	7:3	0.5	150
P ₁₅ V ₁₀	15	10	7:3	0.5	150
P ₁₅ V ₁₅	15	15	7:3	0.5	150
P ₁₅ V ₂₀	15	20	7:3	0.5	150

Remark 2. From the work of Cozza et al. (2013), 15 wt.% and 20 kV were found to be the optimum polymer concentration and voltage that produced uniform and defect-free PVDF nanofibrous membranes. By using these as references, one additional value of polymer

concentration, i.e. 13 wt.% and two other values of voltage, i.e. 10 kV and 15 kV are adopted for further investigations.

Remark 3. *The use of acetone as a co-solvent promoted better solvent evaporation during the electrospinning process due to its higher vapour pressure, which further reduced the chances of bead formation and agglomeration of fibers.*

Remark 4. *Electrospinning was conducted for a duration of 10 hours for each of the samples to obtain a considerable membrane thickness for further characterization tests.*

Remark 5. *The focus of this work is the proposal of novel experimental methods for the mechanical characterization and the constitutive modeling of electrospun PVDF nanofibrous membranes. In order to achieve this, fabrication of electrospun membranes is essential to provide appropriate materials for mechanical characterization (Section 3.2.3) and fiber orientation analysis (Section 3.2.5). However, the optimization of electrospinning parameters will not be investigated in this work.*

3.2 Characterization of electrospun PVDF nanofibrous membranes

In this section, a series of characterizations is conducted to explore the properties and behaviors of the electrospun PVDF nanofibrous membranes. The information obtained will serve as a guideline for the proposal of the constitutive model.

3.2.1 Surface morphology analysis

Characterization tests using Scanning Electron Microscopy (SEM) are necessary to observe the microstructural morphology of the electrospun nanofibrous membrane produced. SEM is an analytical technique which utilizes a focused beam of electrons. The interaction of the electron beam with the sample's atoms produces various signals that reflect the information about the composition and surface morphology of the sample. For this research, a

Phenom ProX Tabletop Scanning Electron Microscope was employed for the surface morphology analysis of the electrospun PVDF nanofibrous membranes while a JEOL JFC-1600 Auto Fine Coater was used for the coating of the electrospun specimens prior to the SEM analysis. The procedure for the SEM characterization was as follows:

1. Specimens with the dimension of 8 mm × 8 mm were cut from the six samples of electrospun PVDF nanofibrous membranes produced, as indicated in Table 3.2.
2. The specimens were then subjected to platinum coating, using the JEOL JFC-1600 Auto Fine Coater, with 10 mA current and a coating duration of 12 seconds. The purpose of the platinum coating is to reduce the undesirable charging effect that might be produced during the SEM characterization tests.
3. Each of the coated specimens was then attached to a sample holder by using the double sided carbon tape.
4. Next, the sample was viewed under SEM with magnifications of 1000 ×, 2000 ×, 5000 × and 10000 × and multiple images of different magnifications were captured.
5. The number of beads on each specimens was observed through the acquired SEM images. Meanwhile, 50 readings of the fiber diameter were manually taken on the plane, from three different spots of the specimen under the magnification of 10000 ×, utilizing the measuring tools in the ImageJ software. Subsequently, the average and standard error of the mean of the fiber diameters were determined from the 50 readings obtained.
6. Step 4 and 5 were repeated for the other five samples fabricated from different sets of electrospinning parameters (Table 3.2).

Remark 6. *The amount of bead defects was evaluated from the SEM images of 1000 × magnification. However, the extraction of quantitative data was a daunting task due to*

the uneven sizes of beads as well as the agglomeration of beaded fibers. For simplicity, a qualitative analysis of the amount of bead defects was utilized in this work, where the amount of beads was classified as “tremendous”, “many”, “intermediate”, “less” and “nil”.

3.2.2 Physical evaluation of undeformed and deformed membranes

In order to further understand the physical characteristics of the material, investigations were conducted to examine the fiber diameter and pore size of the electrospun PVDF nanofibrous membranes, under undeformed and deformed states.

3.2.2.1 Comparison of fiber diameter

From the results of previous analysis, one representative sample was chosen for further characterization tests, i.e. determination of the deformed surface morphology, measurement of porosity, mechanical characterization and fiber orientation analysis.

Apart from the initial surface morphology, the deformed morphology of the electrospun PVDF nanofibrous membranes was also interested in order to determine the morphological changes associated with the applied deformation. For this purpose, the representative sample was again fabricated according to Section 3.1, and surface morphology analysis was again conducted utilizing SEM. Subsequently, specimens of two different conditions were prepared for the analysis: (1) undeformed and (2) deformed up to 20 % strain through uniaxial extension. The detailed procedures of the surface morphology analysis are slightly different as in the previous analysis, and are summarized as follow:

1. Specimen with the dimension of 8 mm × 8 mm was cut from the undeformed sample of electrospun PVDF nanofibrous membranes.
2. The specimen was then subjected to platinum coating, using the JEOL JFC-1600 Auto Fine Coater, with 10 mA current and a coating duration of 12 seconds. The

purpose of platinum coating is to reduce the undesirable charging effect that might be produced during the SEM characterization tests.

3. The coated specimens were attached to a sample holder by using double sided carbon tape.
4. Next, the sample was viewed under SEM with the magnification of $5000\times$ and multiple images were captured.
5. 50 readings of the fiber diameter were manually taken on the plane, from two different SEM images, utilizing the measuring tools in the ImageJ software. Subsequently, the average and standard error of the mean of the fiber diameters were determined from the 50 readings obtained.
6. Steps 1 to 5 were repeated by replacing the undeformed sample with the deformed sample.

From the results of this analysis, the average fiber diameter in the undeformed and deformed states were further analyzed in order to predict the relation between the changes in fiber diameter with overall volume changes of the electrospun membranes.

3.2.2.2 *Measurement of porosity*

The measurement of the porosity provides us with the structural information on the electrospun PVDF nanofibrous membranes. In this work, measurement of porosity is conducted such that the smallest pore size of the electrospun PVDF membranes before and after deformation is determined. Adopting the definition from Nimmo (2004), porosity is the fraction of total volume that is taken up by the pore space. Therefore, this analysis provides additional information for the investigation of the overall morphological changes as well as on the volume changes of the electrospun membranes, which in turn is useful for the prediction of the deformation mechanisms in electrospun PVDF nanofibrous membranes.

Subsequently, the measurement of porosity is conducted on the representative sample as mentioned in Section 3.2.1, through coulter porometer analysis by utilizing the equipment POROLUX 1000. POROLUX 1000 is commonly used to determine the pore size of polymeric membranes. This method measures the flow of gas bubbles through the pores at certain applied pressures. Subsequently, the pore size can be calculated through the Laplace equation and by assuming circular pores. The detailed procedures for the measurement of porosity are summarized as follows:

1. Circular shaped specimen with the diameter of 13 mm was cut from the undeformed sample.
2. The specimen was then subjected to coulter porometer analysis, using POROLUX 1000, by applying a pressure of 2 to 3 bar.
3. Result of the analysis was collected and the last measurement of the pore diameter was noted.
4. Steps 1 to 3 were repeated by replacing the undeformed sample with the deformed sample.

From the results of this analysis, the smallest pore size of undeformed and deformed samples were further analyzed in order to predict the relation between the changes in pore diameter with overall volume changes of the electrospun membranes.

Remark 7. *In morphological analysis, the specimens were deformed up to 20% strain and removed from the grips for further analysis. Therefore, recovery might take place on the deformed specimens.*

3.2.3 Mechanical characterization

Mechanical testing was conducted to investigate the mechanical response of the electrospun PVDF nanofibrous membranes, under simple and complex loading conditions. For

this purpose, an electrospun PVDF nanofibrous membrane with the best combination of fiber diameter and bead defects was subjected to a series of mechanical tests. To this end, a Shimadzu AGS-X Series Universal Tensile Testing Machine equipped with a load cell of 50 N was used along with the Trapezium X Materials Testing Software for all types of test in this research (unless otherwise specified). In this work, three different types of uniaxial loading conditions were considered: monotonic tensile tests, cyclic loading tests with increasing maximum strain and cyclic loadings interrupted with a number of relaxations, where the latter is termed as cyclic-relaxation test.

3.2.3.1 Sample preparation for mechanical characterization

Sample preparation is an important step prior to the mechanical testing. Test samples must be properly prepared in order to obtain consistent and accurate results. For the purpose of mechanical characterization, the sample preparation was carried out as follows:

1. Two perpendicular tensile directions were defined on the PVDF nanofibrous membrane, where the horizontal and vertical directions were designated as X-direction and Y-direction respectively, as shown in Figure 3.3.
2. Specimens with dimension of 60 mm × 10 mm (length × width) (Figure 3.3) were cut from the center of the fiber deposition area which has a constant membrane thickness, from the electrospun PVDF membrane, in both X and Y directions.
3. Intervals of 10 mm were measured and marked from both ends of the specimen (Figure 3.3).
4. Subsequently, the membrane thickness was measured for specimens from different locations using a Mitutoyo ABSOLUTE Digimatic Caliper with accuracy of 0.01 mm.

5. Finally, the 10 mm spaces at both ends of the specimens were gripped onto the tensile testing machine, resulting in a gauge length of 40 mm. Mechanical testing was conducted based on the desired loading conditions.

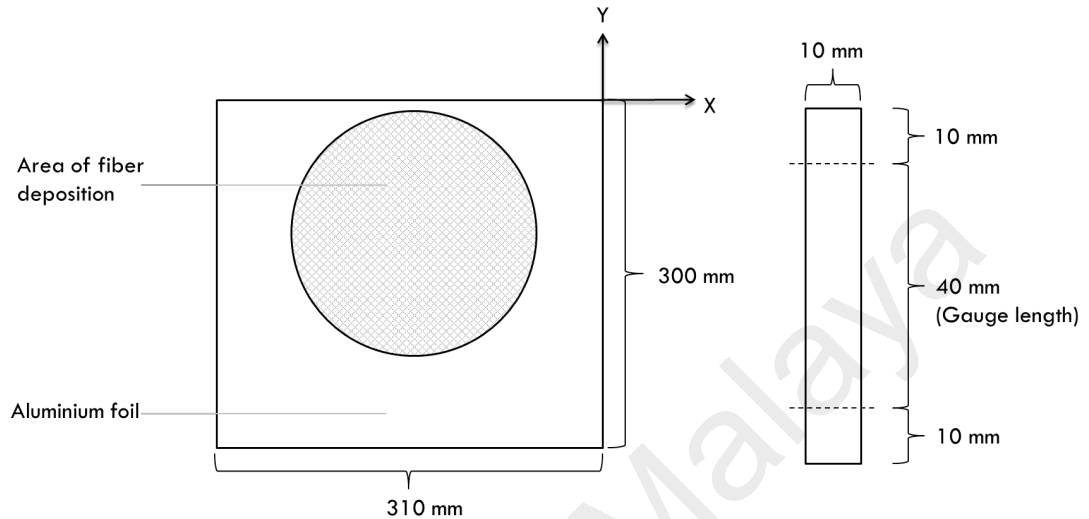


Figure 3.3: Schematic diagram of the electrospun PVDF nanofibrous membrane and dimension of the specimen

Remark 8. *It was assumed that the membrane thickness is homogeneous at the center of the fiber deposition area, and all the neighbouring specimens possess similar membrane thickness as measured. Following the above assumption, the specimens prepared for mechanical testing were not measured with respect to the thickness in order to avoid any undesirable damage on the specimens' surface. Similarly, all the steps were handled with much care in order to minimize the possibility of inducing damage to the delicate material.*

3.2.3.2 Monotonic tensile test

In monotonic tensile test, an increasing load is continuously applied to the specimen to induce deformation on the materials. From the results obtained, the plot of load versus displacement can be used to derive the stress-strain relationship of the material, providing that the area of the specimen is known. Through the stress-strain curve, information of the material such as yield strength, elastic modulus, ultimate tensile strength, fracture strength

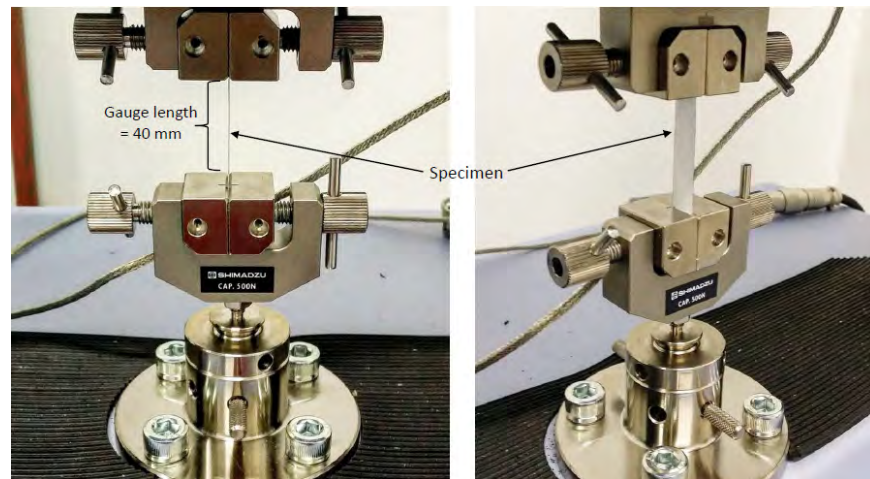
and their related strains can be determined. Generally, the monotonic tensile tests for the electrospun PVDF nanofibrous membranes were conducted as follows:

1. Firstly, a specimen from the X – direction was carefully inserted into the tensile testing machine, by gripping the 10 mm parts on both ends onto the machine. Thus, the remaining 40 mm in the middle part define the gauge length of the specimen. The images of specimen gripping are illustrated in Figure 3.4.
2. The specimen was slightly adjusted such that no buckling was observed on the gripped specimen.
3. The values of thickness, width and gauge length of the specimen were input into the Trapezium X software.
4. The strain rate for the tensile test was fixed at 0.001 s^{-1} .
5. Tensile testing was allowed to run until the fracture of the specimen that eventually brought the testing to a halt.
6. The results obtained were plotted into a stress-strain curve.
7. Steps 2 – 6 were repeated by replacing the X–direction specimens with the Y–direction specimens.

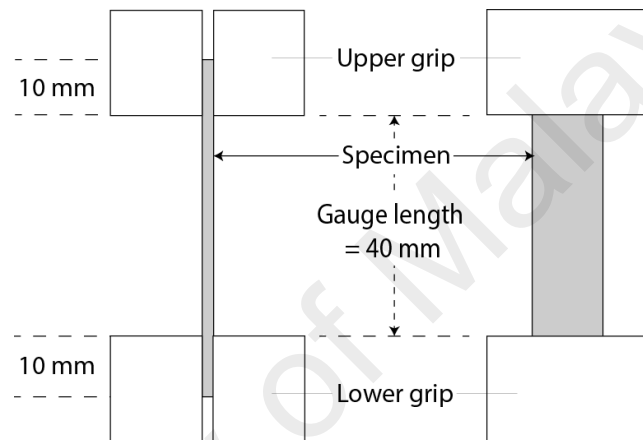
In this work, monotonic tensile tests were conducted for specimens from both X and Y directions in order to study the isotropy of the virgin material. With the obtained results, the tensile direction with higher strain at fracture was considered for the subsequent cyclic loading tests.

3.2.3.3 *Cyclic loading test with increasing maximum strain*

The cyclic loading test implements the application of repeated stresses, strains or stress intensities to the specimen of interest. Commonly, either cyclical tension, compression or



(a)



(b)

Figure 3.4: (a) Images and (b) schematic illustration of the gripping of specimen on tensile testing machine. Front view (left) and side view (right).

a combination of both will be applied to the specimen. Indeed, the purpose of this test was to determine the material's behavior over the duration of the test, as well as to determine the maximum limit which can be sustained by the material when subjected to continuous stresses. Subsequently, specimens from X – direction were selected for the cyclic loading tests with increasing maximum strain. The tests were conducted through the following steps:

1. Firstly, the specimen was properly inserted into the tensile testing machine by gripping the 10 mm parts from both ends onto the machine. Similar to the previous section, the remaining 40 mm in the middle part define the gauge length of the specimen.

2. The specimen was slightly adjusted so that no buckling was observed after gripping.
3. The values of thickness, width and gauge length of the specimen were input into the Trapezium X software.
4. The cyclic loading profile (Figure 3.5) was set as below by means of the Trapezium X software, utilizing the strain rate of 0.001 s^{-1} for all the following steps:
 - a) The specimen was loaded to a strain of 5% and unloaded to a force of 0 N.
 - b) The specimen was loaded to a strain of 10% and unloaded to a force of 0 N.
 - c) The specimen was loaded to a strain of 15% and unloaded to a force of 0 N.
 - d) The specimen was loaded to a strain of 20% and unloaded to a force of 0 N.
 - e) The specimen was loaded to a strain of 25% and unloaded to a force of 0N.
 - f) The specimen was loaded to a strain of 30% and unloaded to a force of 0 N.
 - g) The specimen was loaded again until the fracture of the specimen.
5. The results obtained were plotted into a stress-strain curve.
6. Steps 1 – 5 were repeated on a new specimen to confirm the accuracy and consistency of the results.

Remark 9. *The specimens were unloaded to zero force instead of zero strain at the end of each cycle in order to avoid buckling of the specimens. Indeed, the minimum stretch ratio of each cycle during the unloading is not 1 (see Figure 3.5).*

3.2.3.4 Cyclic-relaxation test

Stress relaxation is the gradual reduction in stress over time under the application of constant strain or displacement. In order to determine the stress relaxation of the material, the specimen is first deformed up to a certain amount of strain below its fracture strain and

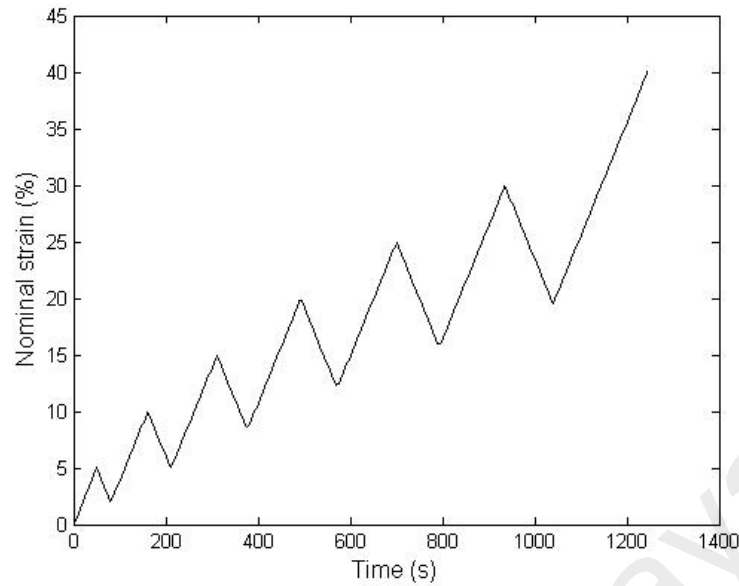


Figure 3.5: Loading profile for cyclic loading test with increasing maximum strain.

held for a period of time. The recorded stress values over the entire duration signify the stress relaxation behavior of the material. In short, stress relaxation test investigates how materials relieve stress under a constant strain. Similarly, specimens from X-direction were considered for the cyclic-relaxation test through the following steps:

1. Firstly, specimen was properly inserted into the tensile testing machine, by gripping the 10 mm parts from both ends onto the machine. Similarly, the remaining 40 mm in the middle part define the gauge length of the specimen.
2. The specimen was slightly adjusted such that no buckling was observed on the gripped specimen.
3. The values of thickness, width and gauge length of the specimen were input into the Trapezium X software.
4. The cyclic-relaxation profile (Figure 3.6) was set as below by means of the Trapezium X software, utilizing the strain rate of 0.001 s^{-1} for all the following steps:
 - a) The specimen was loaded to 10% strain, and held for 15 minutes (900 seconds).

- b) The specimen was further loaded to 20% strain, and held for another 15 minutes.
 - c) The specimen was further loaded to 30% strain and unloaded to 20% strain and held for 15 minutes.
 - d) The specimen was unloaded again to 10% strain, and held for another 15 minutes.
 - e) Finally, the specimen was unloaded to the initial strain of 0% .
5. The results obtained were plotted into a stress-strain curve.
 6. Steps 1 – 5 were repeated on a new specimen to confirm the accuracy and consistency of the results.

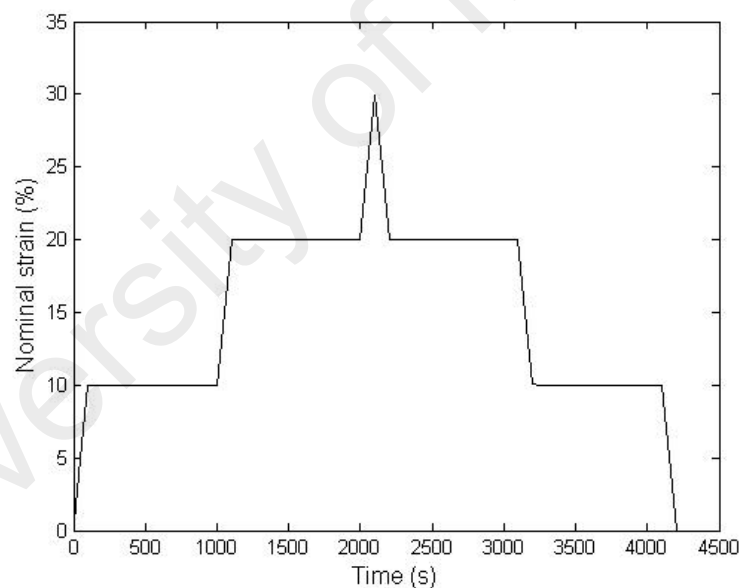


Figure 3.6: Loading profile for cyclic-relaxation test.

Remark 10. *The cyclic-relaxation test in this work consists of one cycle in which the relaxation periods were inserted during both loading and unloading. This peculiar test was adopted from the studies of bulk rubbers and polymer composites which were previously considered by several authors such as Andriyana et al. (2010) and Lion (1996).*

3.2.4 Investigation on volume change and Poisson's ratio

Poisson's ratio is one of the important material properties particularly for engineering materials. The investigation on Poisson's ratio allows us to understand the nature of the materials, as well as to judge the suitability of a material for certain application and subsequently to facilitate the design of materials. Despite the numerous potential applications of electrospun membranes, the Poisson's ratio of the electrospun membranes remains a myth to the researchers. This contributes to the difficulty in structural designing as there is a lack of information of the structures. To the best of our knowledge, there is still no investigation on the Poisson's ratio of electrospun membranes. Therefore, it is particularly important to have a better understanding on the Poisson's effect of the structures in order to have a deeper insight into its mechanical properties as well as to facilitate the development of a constitutive model.

In this section, the Poisson's ratio of randomly oriented electrospun PVDF membranes was investigated. The representative sample was fabricated utilizing the method in Section 3.1, under three different electrospinning durations, i.e. 10 hours (initial duration), 15 hours and 20 hours in order to obtain the representative sample of three different thicknesses. For simplicity, the three samples were named as "PVDF10", "PVDF15" and "PVDF20", where the 10, 15 and 20 represented the duration of electrospinning in hours. The purpose of fabricating electrospun PVDF membranes of three different thicknesses is to investigate the effect of thickness on volume change as well as on the magnitude of Poisson's ratio.

Subsequently, the determination of volume change and Poisson's ratio require the mechanical deformation of the specimens. Here, the Shimadzu AGS-X Series Universal Tensile Testing Machine equipped with a 5 kN load cell was utilized for the mechanical deformation of electrospun PVDF specimens, through uniaxial tensile tests. Subsequently, the identifications of volume change and Poisson's ratio were performed through the measure-

ment of lateral contraction and thickness change concurrently with the application of axial elongation. The detailed procedures for the determination of volume change and Poisson's ratio are summarized as follow:

1. Three specimens were cut in the dimension of 70 mm × 10 mm (length × width) from the PVDF10 sample (Figure 3.7 (a)), from the center of the fiber deposition area.
2. Subsequently, markings were made on three different positions on each specimen, as shown in Figure 3.7 (b).
3. The initial widths and thicknesses for all three specimens were measured at the three different positions (Figure 3.7 (b)), by adopting a Dino-Lite digital microscope and a Mitutoyo measuring gauge with an accuracy of 0.001 mm and measuring force of less than 3.5 N respectively.
4. Following this, mechanical deformation was conducted at a strain rate of 0.00002 s⁻¹.
5. The measurements of widths and thicknesses were acquired at strain levels of 5%, 10% and 20%, similarly at three different positions as specified earlier.
6. The volume at each strain level, for each specimen was computed through the multiplications of width, thickness and length at the specific strain level.
7. Finally, the Poisson's ratio was determined through the plot of the logarithm of transverse stretches versus the logarithm of axial stretch, by taking the slope of the linear plot through the data points where y-intercept was set to be zero.
8. Steps 1-7 were repeated twice by replacing PVDF10 sample with PVDF15 and PVDF20 samples.

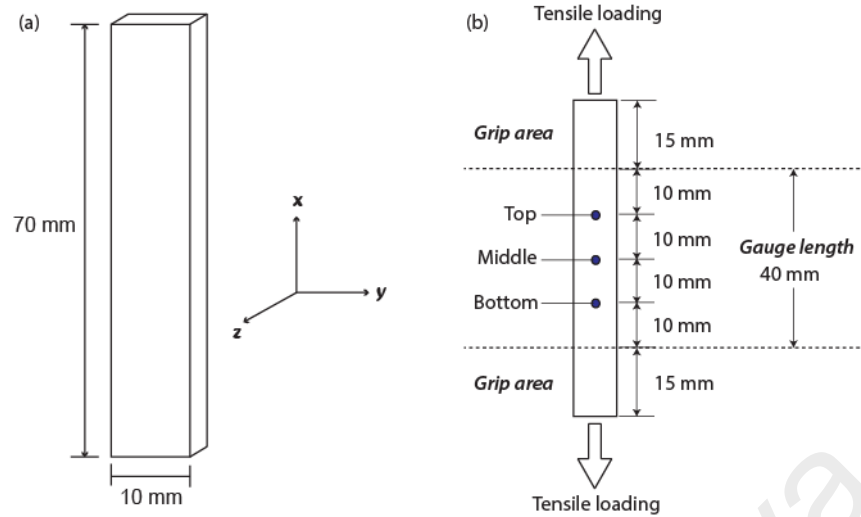


Figure 3.7: (a) Dimensions and axes of specimen, (b) illustration of specimen's measuring locations and gripping areas.

By representing the mechanical deformation in terms of stretches, the three-dimensional deformation gradient tensor for the case of uniaxial extension can be written in the general form as

$$\mathbf{F} = \begin{bmatrix} \lambda_1 & 0 & 0 \\ 0 & \lambda_2 & 0 \\ 0 & 0 & \lambda_3 \end{bmatrix} \quad (3.1)$$

Subsequently, the in-plane and out-of-plane Poisson's ratio can be determined by taking the gradients of the plots of $\ln \lambda_2$ and $\ln \lambda_3$ versus $\ln \lambda_1$ respectively.

Remark 11. *The extremely low strain rate of 0.00002 s^{-1} was chosen in order to allow sufficient duration for the images capturing as well as the measurement of the thicknesses of the specimens, at a particular strain level, without the need of halting the applied deformations. Here, it is assumed that the volume change of the electrospun structures is independent of the strain rate imposed during the mechanical test and therefore lowering the strain rate has an insignificant effect on the volume change.*

Remark 12. *Conventionally, Poisson's ratio is measured within the linear elastic region of the materials response. This concept is generalized in the present work. Indeed, the*

measurement of Poisson's ratio is conducted beyond elastic region for electrospun PVDF membranes.

3.2.5 Fiber orientation analysis

For this research, a stationary grounded collector was utilized for the collection of PVDF nanofibers fabricated through the electrospinning processing method. Randomly orientated fibers were observed to be deposited on the stationary collector where the orientation of fibers was of great interest. Generally, the objective of fiber orientation analysis is to investigate the average fiber orientation in the membrane before and after the application of mechanical loading, i.e. when the stress is null. Subsequently, it allows for the observation of deformation-induced fiber re-orientation effects of the material. Similar to the mechanical characterization, the same sample with the best combination of fiber diameter and bead defects was adopted for the fiber orientation analysis.

Three assumptions were made prior to the fiber orientation analysis: (1) Fiber orientation is assumed to be in-plane (two-dimensional); (2) Fiber orientation at the top layer is assumed to represent the fiber orientation of the whole material; (3) Effect of bead defects on fiber orientation is negligible due to the choice of sample that contains less beads as possible. Subsequently, the experimental procedure for the fiber orientation analysis was as follows:

1. A specimen of similar dimensions as in mechanical characterization (60 mm × 10 mm) was properly inserted into the tensile testing machine, by gripping the 10 mm parts from both ends of the specimen. The remaining 40 mm define the gauge length of the specimen.
2. The specimen was stretched up to 5% strain with the strain rate of 0.001 s⁻¹.
3. The stretched specimen was carefully removed from the tensile machine and the mid-

dle section of approximately 8 mm × 8mm was cut from the deformed specimen.

4. The stretching direction was marked on the cut specimen and the sample was attached to the sample holder for SEM analysis.
5. The sample was examined under 5000 × magnification and 35 images from different locations of the sample were captured.
6. Steps 1 – 5 were repeated by replacing the 5% strain with 10%, 20% and 25%.
7. Finally, an undeformed electrospun sample (0% strain) of approximately 8 mm × 8mm was cut and examined under SEM using 5000 × magnification, and 35 images from different specimen locations were captured.

Overall, the specimens were deformed by stretching up to a certain maximum strain and unloaded to zero force, as shown in Figure 3.8 (a), while the corresponding illustration of the deformation mechanism was depicted in Figure 3.8 (b). Here, ε_i indicates the maximum applied strain while ε_{in} is the inelastic (residual) strain remains on the material at the end of each deformation. Following this, each of the acquired images was analyzed using the ImageJ software, through the OrientationJ Distribution processing method to obtain the distribution of fiber orientations. No further image treatment was done prior to image processing. Here, the OrientationJ plugin evaluates the orientation for every pixel of the images based on the structure tensor defined for each pixel (Rezakhaniha et al., 2012). The analysis using OrientationJ Distribution provides the results of fiber orientations in terms of the probability distribution function, which is the probability of finding a fiber in each direction, i.e. from the orientation of $-\pi/2$ to $\pi/2$. Subsequently, the fiber orientation distribution of 35 images were averaged and normalized for each strain level. Employing the average fiber orientation distribution, the component of fiber orientation tensor along the direction of stretching (A_{11}) was determined by utilizing the equations for the fiber

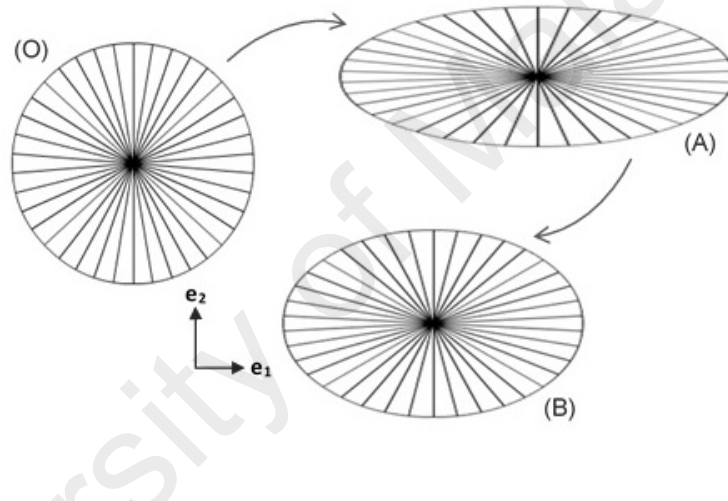
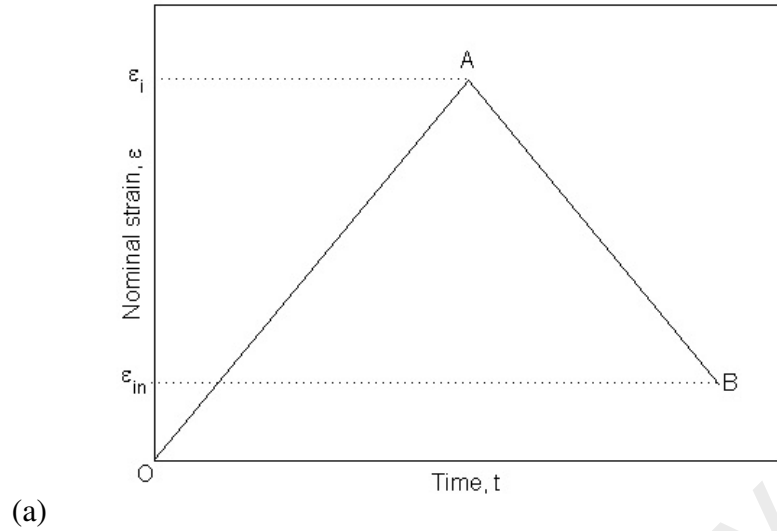


Figure 3.8: (a) Loading sequence for fiber orientation analysis and (b) illustration of deformation-induced fiber re-orientation.

orientation tensor \mathbf{A}_0 adopted from Advani and Tucker (1987) as follows:

$$\mathbf{A}_0 = \int_{\omega} \rho(\mathbf{a}_0) \mathbf{a}_0 \otimes \mathbf{a}_0 d\omega \quad (3.2)$$

The function $\rho(\mathbf{a}_0)$ denotes the normalized orientation distribution function with respect to the referential orientation \mathbf{a}_0 , which is obtained from the OrientationJ analysis. Assuming a two dimensional fiber orientation as examined under the SEM, an arbitrary unit direction vector was defined by

$$\mathbf{a}_0(\theta) = \cos \theta \mathbf{e}_1 + \sin \theta \mathbf{e}_2 \quad (3.3)$$

where $\mathbf{e}_{i(i=1,2)}$ define the axis of the Cartesian coordinate plane and θ is the angle of fiber with respect to the horizontal plane axis. Subsequently, the desired A_{11} orientation tensor can be expressed in the form of

$$A_{11} = \int_{-\pi/2}^{\pi/2} \rho(\theta) \cos^2 \theta d\theta \quad (3.4)$$

Remark 13. *Due to limitations of the available equipment, the deformation and surface morphology analysis of the specimens cannot be conducted concurrently. In this case, the specimens were immediately removed from the tensile machine after being stretched to the desired maximum strains. Thus, the specimens did not remain at the stretched configuration but in turn restored to a lower strain (residual or inelastic strain) as illustrated in Figure 3.8. Hence, it is important to note that the analyzed fiber orientation of the deformed specimens corresponded to the configuration at point B in Figure 3.8, which is the unloaded (or intermediate) configuration of the material.*

3.3 Constitutive modeling

Constitutive modeling is the mathematical description of the response of materials to various loadings. It is important for the prediction of the mechanical responses of the materials without the need of conducting experiments that are often costly and time consuming.

3.3.1 Characteristics of structures

The understanding of the materials characteristics is of particular importance in order to develop a constitutive model with sufficient physical meaning. Electrospun nanofibrous membrane is a material composed of uncountable nano-size fibers produced via the process of electrospinning. From the surface morphology analysis in Section 3.2.1, the SEM observations provide an idea of the microstructure of the material where it is noted that the electrospun membrane is made up of a number of fibrous layers and the fibers are mostly

long and straight. Moreover, it is believed that when the nanofibers are combined as a whole material, some inter-fiber interactions exist such as the fiber-fiber cohesion due to the electrostatic forces of attraction between fibers.

Theoretically, each fiber stands alone in an electrospun membrane because fibers are produced continuously one after another in the process of electrospinning. Unlike the fiber-reinforced material, there is no matrix that holds between the fibers. However, some fiber-fiber junctions are observed in the fabricated membrane that tend to connect two or more fibers. This structure is most likely due to the incomplete solvent evaporation when fibers are deposited on the collector, and causes two or more fibers to be jointed to form a junction. A great number of parameters control the final product of the electrospinning process, and the optimum conditions vary from one polymer to another. Thus, it is important to note that the fabrication of a perfect electrospun membrane with zero bead and junction is an extremely difficult task to be achieved and still being widely investigated in these days.

In general, apart from the contribution of an individual nanofiber, the fiber interactions and physical bondings would give an overall effect on the macroscopic scale which in turn contributed to the mechanical performance of the material. Recalling previous experimental works on electrospun nanofibrous materials (Huang et al., 2004; Molnar et al., 2012), some general features were observed including finite strain, elasticity and irreversible deformation. All these behaviors have to be taken into account in the development of an efficient constitutive model, e.g. in a phenomenological way.

3.3.2 Description of deformation and stress-strain response

The proposed model is inspired by the works of Planas et al. (2007) and Ridruejo et al. (2012). Planas et al. (2007) developed a continuum model to describe the macroscopic mechanical response of fiber-reinforced materials, which was later utilized by Ridruejo et al. (2012) to model nonwoven fabric. Different from the works of Planas et al. (2007) and

Ridruejo et al. (2012), modifications are made based on the experimental observations as well as on the structures of interest in this work, e.g. by using true stress and strain at the microscopic scale due to large deformations. Moreover, the present work focuses on reproducing the complex mechanical response of the structure of interest, which is not seen in the previously mentioned works.

In the present work, the fiber network structure is taken into consideration for the derivation of constitutive model. Furthermore, the computation of the macroscopic mechanical response requires the three-dimensional constitutive equation which can be obtained from the one-dimensional constitutive equation by integration over the unit element (Verron, 2015). By referring to Figure 3.9, the following assumptions are made to formulate

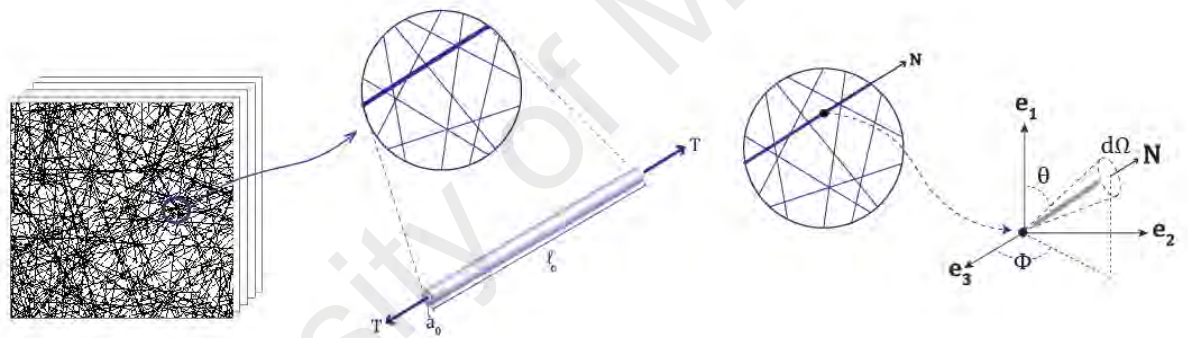


Figure 3.9: Schematic illustration of electrospun nanofibrous membrane and orientation of a single fiber characterized by unit vector \mathbf{N} in the reference configuration.

the continuum model:

1. Electrospun nanofibrous membrane is assumed to be homogenous and continuous at the macroscopic scale.
2. Electrospun nanofibrous membranes are made up of a number of layers of nanofibers which are superimposed, where the properties from one layer to another are assumed to be identical. Consequently, the properties are invariant in the direction perpendicular to the fiber layer. Moreover, fiber orientation varies only in-plane ($\Phi = \pi/2$), i.e. the material is transversely isotropic.

3. Since the properties in one nanofiber layer are assumed to be same as those in other layers, the deformation characteristics of the whole membrane can be described by considering only one layer. Therefore, while the general derivation of the proposed model is presented using a three-dimensional framework, the present work focuses on the in-plane (two-dimensional) mechanical response of the electrospun nanofibrous structures.
4. Single nanofibers are assumed to be incompressible, i.e. each fiber deforms with the constraint of constant volume. Moreover, it deforms following the deformation of the membrane, i.e. the motion is affine.

Considering the hyperelastic framework, we postulate the existence of a strain energy function W defined per unit volume in the reference (undeformed) configuration. Furthermore, it is assumed that W is the sum of strain energies in all possible in-plane directions of the fiber $w = w(\lambda_f^\theta)$ as follows (Lanir, 1983):

$$W = \int_{-\pi/2}^{\pi/2} \Psi(\theta) w(\lambda_f^\theta) d\theta \quad (3.5)$$

where $\Psi(\theta)$ is the probability of finding fibers in a particular orientation θ and λ_f^θ is the fiber stretch at the corresponding orientation which can be calculated from the assumption of an affine motion:

$$\lambda_f^\theta \equiv \frac{l}{l_o} = \|\mathbf{F}\mathbf{N}^\theta\| \quad (3.6)$$

In the above equation, l and l_o are the current and initial fiber lengths respectively. Moreover, \mathbf{F} is the deformation gradient tensor and \mathbf{N}^θ is the unit vector along the fiber direction in its reference (undeformed) configuration. The first Piola-Kirchhoff stress tensor is simply

defined as $\mathbf{P} = \partial W / \partial \mathbf{F}$ (Holzapfel, 2000) that leads to:

$$\mathbf{P} = \int_{-\pi/2}^{\pi/2} \Psi(\theta) \frac{\partial w}{\partial \lambda_f^\theta} \frac{\partial \lambda_f^\theta}{\partial \mathbf{F}} d\theta \quad (3.7)$$

Using Equation (3.6) and simple tensor algebra, we have

$$\frac{\partial \lambda_f^\theta}{\partial \mathbf{F}} = \mathbf{F} \frac{\mathbf{N}^\theta \otimes \mathbf{N}^\theta}{\|\mathbf{F}\mathbf{N}^\theta\|} \quad (3.8)$$

and the first Piola-Kirchhoff stress tensor in Equation (3.7) becomes

$$\mathbf{P} = \mathbf{F} \int_{-\pi/2}^{\pi/2} \Psi(\theta) s_f^\theta \frac{\mathbf{N}^\theta \otimes \mathbf{N}^\theta}{\|\mathbf{F}\mathbf{N}^\theta\|} d\theta \quad (3.9)$$

where s_f^θ is the nominal (engineering) fiber stress defined by

$$s_f^\theta = \frac{\partial w}{\partial \lambda_f^\theta}. \quad (3.10)$$

Using the incompressibility assumption of each nanofiber, the true fiber stress σ_f^θ is

$$\sigma_f^\theta = \lambda_f^\theta s_f^\theta = \lambda_f^\theta \frac{\partial w}{\partial \lambda_f^\theta}. \quad (3.11)$$

The above equation suggests that the nominal or true fiber stress can be determined once w is postulated. More precisely, in order to describe a particular material behavior, information has to be provided to the micromechanical model defined by the constitutive relation at the fiber scale. Finally, the first Piola-Kirchhoff stress tensor in Eq (3.9) becomes

$$\mathbf{P} = \mathbf{F} \int_{-\pi/2}^{\pi/2} \Psi(\theta) \sigma_f^\theta \frac{\mathbf{N}^\theta \otimes \mathbf{N}^\theta}{\|\mathbf{F}\mathbf{N}^\theta\|^2} d\theta \quad (3.12)$$

It is to note that the final expression of the first Piola-Kirchhoff stress tensor necessitates

the description of the true fiber stress. The corresponding description will be provided in Chapter 5. Following Planas et al. (2007), the deformation-induced fiber re-orientation can be evaluated by using the orientation index β defined by

$$\beta = \int_{-\pi/2}^{\pi/2} \Psi(\theta) \frac{\mathbf{FN}^\theta}{\|\mathbf{FN}^\theta\|} \cdot \mathbf{e}_1 d\theta \quad (3.13)$$

It is to note that $\beta = 2/\pi$ if the material is isotropic in the plane (Ridruejo et al., 2012). The orientation index can be linked to A_{11} (from Section 3.2.5) since both expressions define the re-orientation of fibers corresponding to uniaxial deformation. Further derivations will be presented in Chapter 5 while the comparison between experimental fiber re-orientation (A_{11}) and model prediction (β) will be conducted.

University of Malaya

CHAPTER 4: EXPERIMENTAL RESULTS AND DISCUSSION

4.1 Surface morphology analysis

In the present work, electrospinning of PVDF membranes was conducted by manipulating the polymer concentration as well as the applied voltage. Since optimization of electrospinning parameters is not investigated, all other parameters such as feed rate, capillary-to-collector distance and the ratio of solvents were kept constant in order to minimize the scope of investigations. Non-woven electrospun PVDF nanofibrous membranes were successfully fabricated utilizing different sets of electrospinning parameters. However, none of the membranes produced is completely free of beads and a wide range of fiber diameter is observed. According to Zhao et al. (2005), electrospun PVDF membranes possess more irregular and random fiber shapes with large differences between the fiber diameters compared to other polymeric membranes. Thus, it is difficult to obtain perfectly fabricated PVDF nanofibrous membranes through the electrospinning processing method.

Here, two different polymer concentrations of 13 wt.% and 15 wt.% were investigated while three different voltages were considered, i.e. 10 kV, 15 kV and 20 kV. Generally, randomly oriented fibers were collected on the aluminium foil attached to the stationary electrically grounded collector. The resulting fiber surface morphology was examined under SEM. The SEM micrographs of 1000 × and 5000 × magnifications are depicted in Figure 4.1 and Figure 4.2, for the polymer concentrations of 13 wt.% and 15 wt.% respectively. In order to analyze the effect of varying polymer concentration and applied voltage on the electrospun PVDF membrane, the average fiber diameter and the amount of bead defects for each sample in Table 3.2 were analyzed, and the results are subsequently tabulated in Table 4.1.

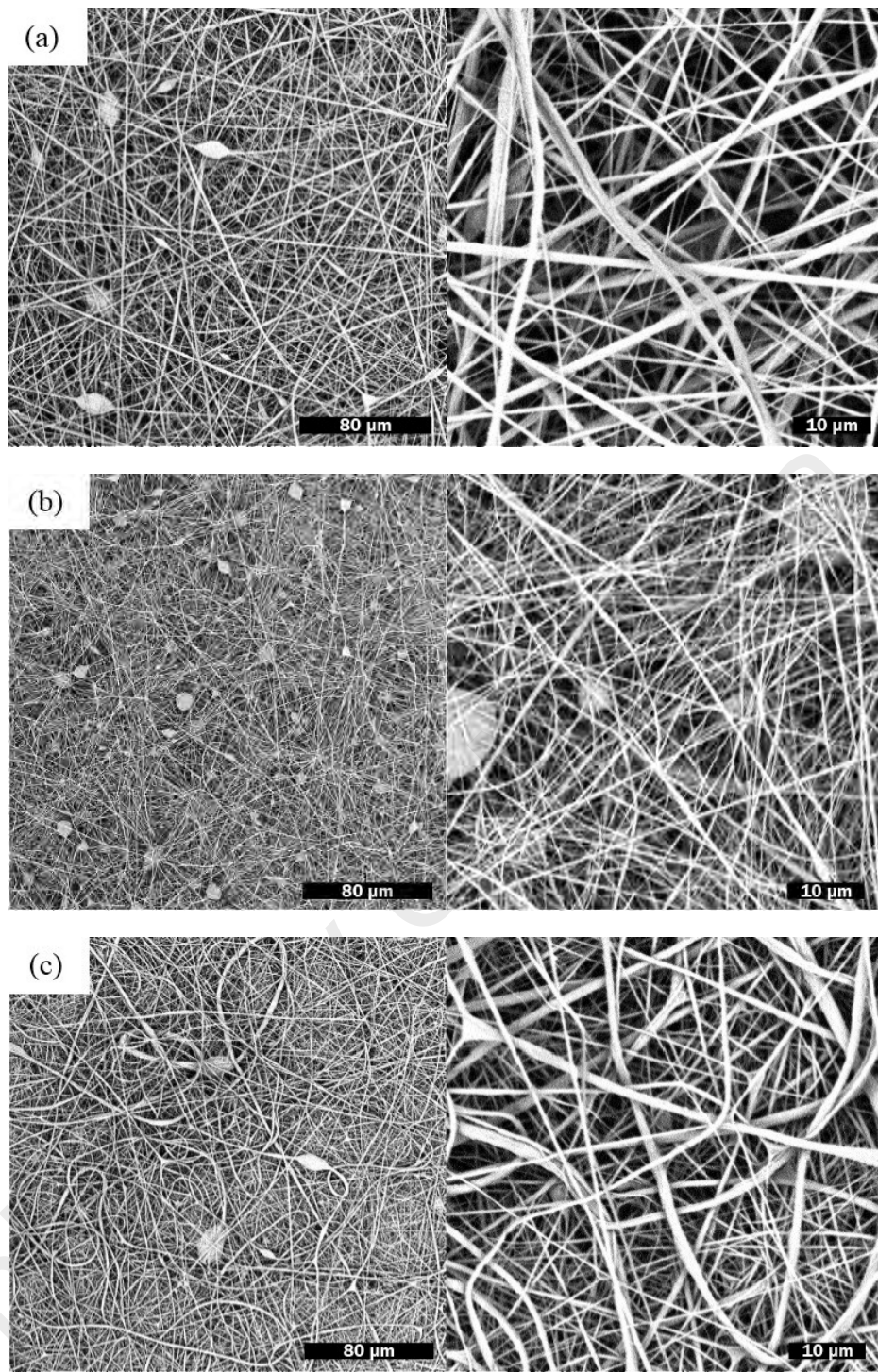


Figure 4.1: SEM micrographs of electrospun PVDF membranes with different processing voltages. Polymer concentration: 13 wt.%. Original magnification: 1000 × (left) and 5000 × (right). (a) 10 kV, (b) 15 kV, (c) 20 kV.

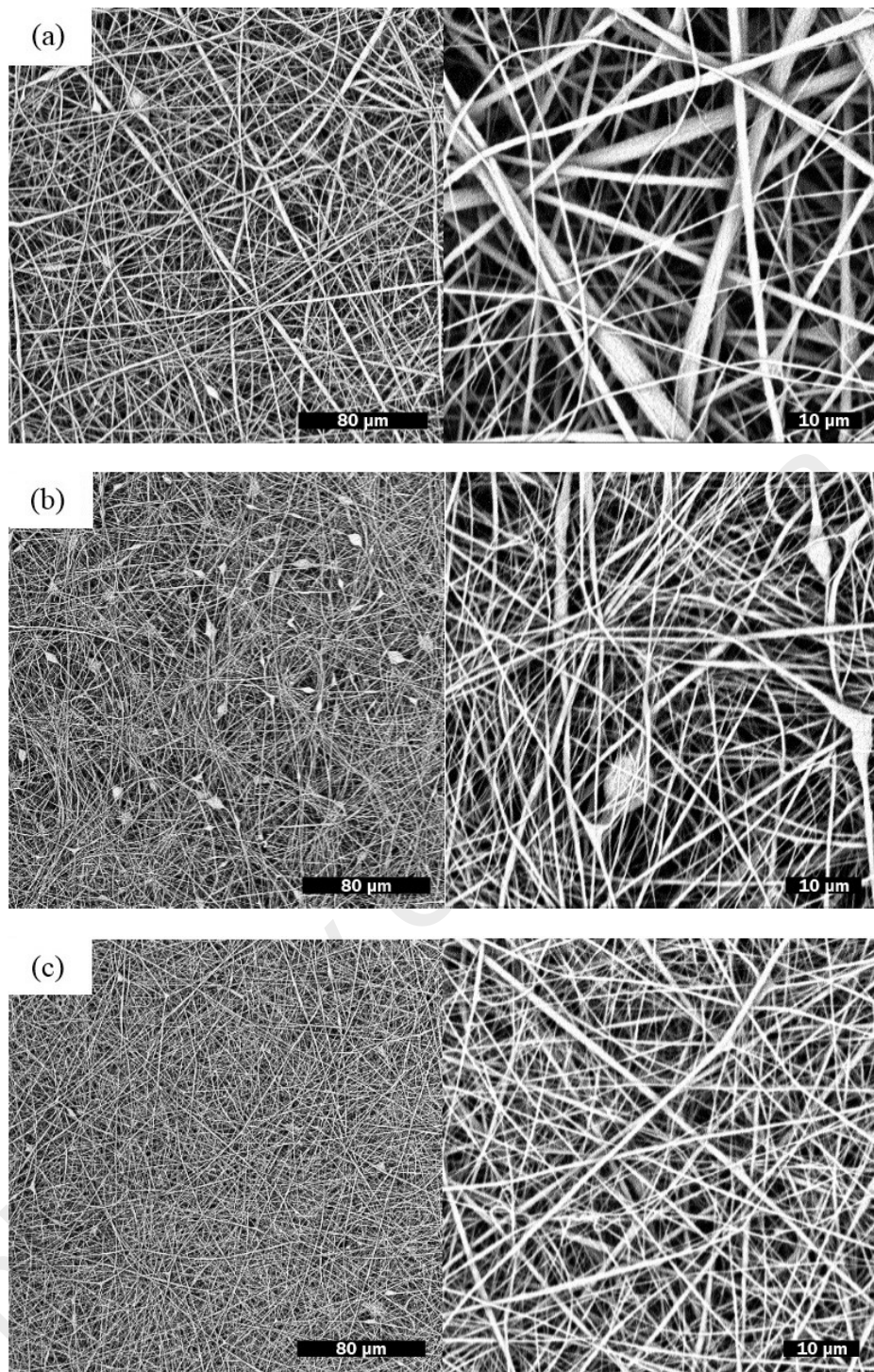


Figure 4.2: SEM micrographs of electrospun PVDF membranes with different processing voltages. Polymer concentration: 15 wt.%. Original magnification: 1000 × (left) and 5000 × (right). (a) 10 kV, (b) 15 kV, (c) 20 kV.

Table 4.1: Average fiber diameter and amount of beads for electrospun PVDF membranes.

Samples	Average diameter (nm)	Amount of beads
P ₁₃ V ₁₀	497 ± 49	Intermediate
P ₁₃ V ₁₅	295 ± 17	Tremendous
P ₁₃ V ₂₀	493 ± 36	Intermediate
P ₁₅ V ₁₀	777 ± 93	Less
P ₁₅ V ₁₅	399 ± 27	Tremendous
P ₁₅ V ₂₀	378 ± 22	Less

The average fiber diameter is represented as mean ± standard error of mean in Table 4.1. In general, a wide range in the diameter distribution is observed for each electrospun PVDF nanofibrous membrane. It is noticed that sample P₁₃V₁₅ possesses the smallest average fiber diameter of 295 nm whereas the largest average diameter of 777 nm is observed for the sample P₁₅V₁₀. Meanwhile, samples P₁₃V₁₅ and P₁₅V₁₅ hold the most number of bead defects while sample P₁₅V₁₀ and P₁₅V₂₀ possess lesser bead defects. Indeed, two extremities are noticed where sample P₁₃V₁₅ possesses the most desired fiber diameter but hold the highest number of beads, while the opposite is observed on sample P₁₅V₁₀.

4.1.1 Effects of applied voltage

On comparing the overall surface morphology, similar trend of increasing and then decreasing bead density is observed on both 13 wt.% and 15 wt.% polymer concentrations as the results of increasing applied voltage, indicating the existence of an optimum voltage range for the electrospinning of PVDF membranes. In this study, two optimum ranges which revolve around 10 kV and 20 kV voltages are determined through the smaller amount of beads per unit area. An applied voltage out of the optimum range produces a stronger or a weaker electric field which results in beaded morphologies or even the inhibition of jet initiation. According to Baji et al. (2010), an applied voltage lower than the critical voltage produces low electrostatic forces which is insufficient to overcome the surface tension of the polymer solution. Indeed, high voltage out of the critical range produces discontinuous

solution jet which promotes high bead density on the electrospun fibers, as reported in the findings of Deitzel et al. (2001). This phenomenon is in accordance with Cozza et al. (2013) and Pillay et al. (2013) whereby an optimum range of applied voltage is said to be existed for every polymer solution which greatly depends on the polymer-solvent system. This theory of optimum voltages is also supported by other literatures through the investigations on different polymer-solvent systems (Liu et al., 2011; Zhao et al., 2005).

For the comparisons of the average fiber diameter, dissimilar trends are noticed on 13 wt.% and 15 wt.% PVDF membranes upon increasing the applied voltages from 10 kV to 20 kV. Generally, the relationship between applied voltage and average fiber diameter is presented in Figure 4.3, for the polymer concentrations of 13 wt.% and 15 wt.%. On the basis of these findings, varying the applied voltage produces significant effects on the average fiber diameters where the results strongly depend on the polymer-solvent system. From Figure 4.3, the investigation on 13 wt.% polymer concentration results in an initial decrease and then increase in fiber diameter after a definite point, which is similar to the findings reported by Pillay et al. (2013), when the applied voltage was increased beyond a critical value. Meanwhile, the average fiber diameter for 15 wt.% polymer concentration demonstrates a monotonically decreasing trend upon increasing the applied voltage. These results are attributed to the stronger electric field that contributes to an increase in charge jet repulsion, which eventually leads to a higher degree of jet stretching and consequently to the decrease in the fiber diameter (Pillay et al., 2013).

4.1.2 Effects of polymer concentration

Polymer concentration plays a crucial role on the electrospinning process since it dictates the viscosity of polymer solutions and the resulting membrane's morphology. Indeed, increasing polymer concentration decreases the amount of beaded fibers while the applied voltage is kept constant, as shown in Table 4.1. At lower polymer concentration, lower solu-

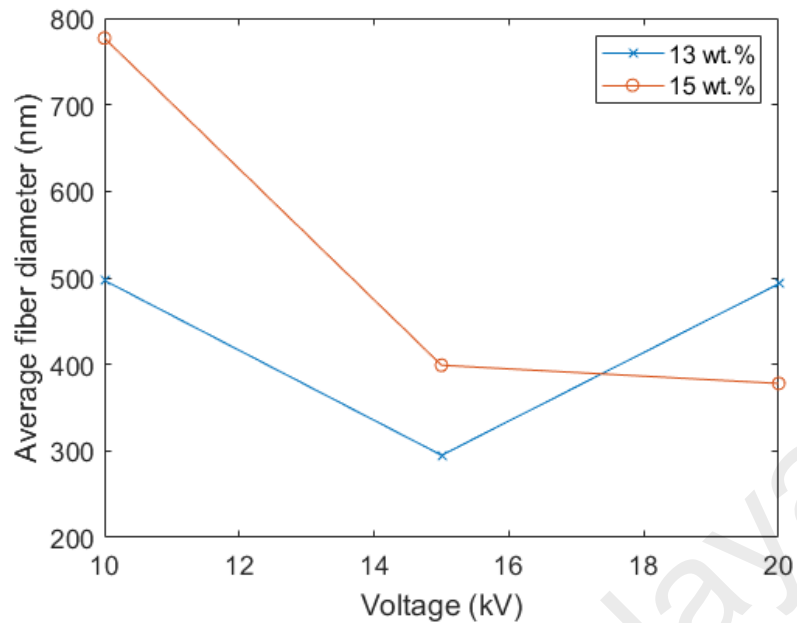


Figure 4.3: Relationship between applied voltage and average fiber diameter, for 13 wt.% and 15 wt.% polymer concentrations.

tion viscosity results in the fragmentation of charged jet due to the stronger repulsive force, which promotes the formation of beads and beaded fibers. Increase in polymer concentration generates higher solution viscosity that improves the entanglements between polymeric chains. Hence, preventing the fragmentation of the fiber jet and resulting in smoother fibers with little or no bead defect (Greiner & Wendorff, 2007; He et al., 2011; Venugopal et al., 2004).

Further comparisons on the average fiber diameter are conducted for different polymer concentrations while keeping the voltage constant. As shown in Table 4.1 and Figure 4.3, it appears that increasing polymer concentration from 13 wt.% to 15 wt.% increases the average fiber diameter when 10 kV and 15 kV voltages are utilized. It is commonly observed that the viscosity of the polymer solution increases with the polymer concentration. This in turn promotes a higher viscoelastic force that resists the stretching of the charged jet and subsequently the formation of thicker fibers. This finding had been widely reported in the literatures as the average diameter of electrospun fibers increases with spinning solution concentration (Beachley & Wen, 2009; Deitzel et al., 2001; Meechaisue et al., 2006).

Meanwhile, the opposite is observed for the applied voltage of 20 kV, which is believed to be the combination effect of polymer concentration and applied voltage.

Overall, increasing applied voltage promotes smaller fiber diameter but an increasing number of beads; while increasing polymer concentration produces larger fiber diameter with less beads. Here, it is suggested that a combination effect exists when polymer concentration and applied voltage were manipulated concurrently for the electrospinning processes. In order to produce bead free fibers, high polymer concentration with applied voltage in the optimum range are required. However, highly concentrated polymer solutions possess high viscosities that resist jet stretching during the electrospinning process, thus producing fibers with larger diameter which is often undesirable. Therefore, a higher voltage in the optimum range is needed to overcome the high viscoelastic forces of the solution to promote sufficient jet stretching, in order to produce thinner fibers along with smooth and bead free surface morphology. The result of this great combination effect of polymer concentration and applied voltage is reflected in sample P₁₅V₂₀, as indicated in Figure 4.2 (c) and Table 4.1.

4.1.3 Choice of samples for mechanical characterization

In order to provide an appropriate material for both the mechanical characterization and the fiber orientation analysis, six samples of PVDF nanofibrous membranes were fabricated using different electrospinning parameters. Among the six samples, only one sample with characteristics close to the ideal electrospun material (see Introduction) will be chosen as the representative for further characterization tests. Here, two criteria for ideal electrospun material are considered in the sample selection: (1) least number of beads and (2) small average fiber diameter.

Recalling the results presented in Table 4.1, both samples P₁₅V₁₀ and P₁₅V₂₀ fulfill the first criterion by possessing “less” beads compared to the other four samples. Thus,

the four samples with more beads are eliminated in the selection with first criterion. By switching the attention to the second criterion, comparison of average fiber diameter is made on samples $P_{15}V_{10}$ and $P_{15}V_{20}$. Results show that the sample $P_{15}V_{20}$ possesses a smaller average fiber diameter which is in accordance with the second criterion mentioned. By utilizing a qualitative selection method, the sample $P_{15}V_{20}$ is eventually chosen for further characterization tests.

4.2 Physical evaluation on undeformed and deformed membranes

The average fiber diameter and pore size of undeformed and deformed electrospun PVDF membranes were investigated, and the results are explained in the following sections.

4.2.1 Comparison of fiber diameter

From Section 4.1.3, the sample $P_{15}V_{20}$ is chosen as the representative sample for the investigations of initial and deformed morphologies of electrospun PVDF membranes. From the SEM analysis, images of $5000\times$ were taken for both undeformed and deformed specimens which were followed by the measurement of fiber diameters.

From both the SEM and the ImageJ analysis, undeformed and deformed specimens of the $P_{15}V_{20}$ sample possess average fiber diameters of 419 nm and 321 nm respectively, showing a significant decrement of 23.4% in accordance to the applied uniaxial deformation of 20% strain. It is suggested that as the electrospun fibers are deformed, fibers elongate resulting in the thinning of fibers, as observed in the decrease in average fiber diameter. Subsequently, the average fiber diameters with their standard error of mean are presented in Table 4.2, under two different conditions (undeformed and deformed).

Remark 14. *The minor discrepancy in the initial average fiber diameter in Table 4.2 with that reported in Table 4.1 might due to the small discrepancies arose during the fabrication of another $P_{15}V_{20}$ membrane, since the environmental parameters such as humidity and*

temperature were neither fixed nor manipulated during the fabrication process.

4.2.2 Measurement of porosity

Similarly to Section 4.2.1, the sample P₁₅V₂₀ was subjected to coulter porometer analysis under undeformed and deformed conditions, by adopting the equipment POROLUX 1000. Subsequently, the smallest pore diameter observed for undeformed condition is 176 nm while for deformed condition is 269 nm, showing an increase in the size of porosity of approximately 52%. The pore diameters for undeformed and deformed conditions are tabulated in Table 4.2, together with the measurement of fiber diameters in Section 4.2.1. Consequently, the changes in fiber diameter and pore diameter may contribute to the overall volume changes of the electrospun PVDF membranes, which will be further explained in the later section where volume changes are studied.

Table 4.2: Average fiber diameter and pore diameter of undeformed and deformed conditions for P₁₅V₂₀ sample.

Properties	Conditions	
	Undeformed	Deformed
Fiber diameter (nm)	419 ± 10	321 ± 10
Pore diameter (nm)	176	269

4.3 Mechanical testing

The mechanical properties of electrospun polymeric membranes are of great interest for many researchers. However, the difficulties in specimen preparation and handling obstruct the intention and motivation of researchers to perform mechanical testing on electrospun nanofibrous membranes. Thus, only the basic mechanical properties of electrospun PVDF membrane were probed by some of researchers (Choi et al., 2004; K. Hwang et al., 2011; Zhao et al., 2005).

For this research, the purpose is to explore the mechanical properties of electrospun PVDF membranes in a deeper extent, in the view of durability analysis. Following the previous sample selection in Section 4.1.3, sample P₁₅V₂₀ was employed for a series of mechanical tests, including monotonic tensile tests, cyclic loading tests with increasing maximum strain and cyclic-relaxation tests. Results obtained for each test will be discussed in the following sections.

4.3.1 Monotonic tensile test

Monotonic tensile test is the mechanical testing where specimen is subjected to tension in a single direction until the specimen experiences failure. For this test, two tensile directions, i.e. X and Y-directions were defined on the electrospun nanofibrous membrane as depicted in Section 3.2.3.2. Monotonic tensile tests were conducted on both tensile directions, and the resulting force-displacement curves are depicted in Figure 4.4. The transition from force-displacement curves to stress-strain curves is one of the challenges in this work due to the delicate specimens which made the tracking of the cross-section difficult. Thus, the mechanical response of the material is expressed in terms of the nominal (engineering) strain and stress for all the tests conducted. Here, nominal strain is taken as the ratio of the distance changed between two grips in tensile testing machine with its initial distance, while nominal stress is calculated from the ratio of force and initial measured cross-section. Following this, stress-strain curves for the monotonic tensile test are shown in Figure 4.5.

From the monotonic stress-strain curves in Figure 4.5 (a) and Figure 4.5 (b), representative mechanical properties such as stress and strain at fracture, yield strength and Young's modulus are determined for both X and Y tensile directions and the results are tabulated in Table 4.3.

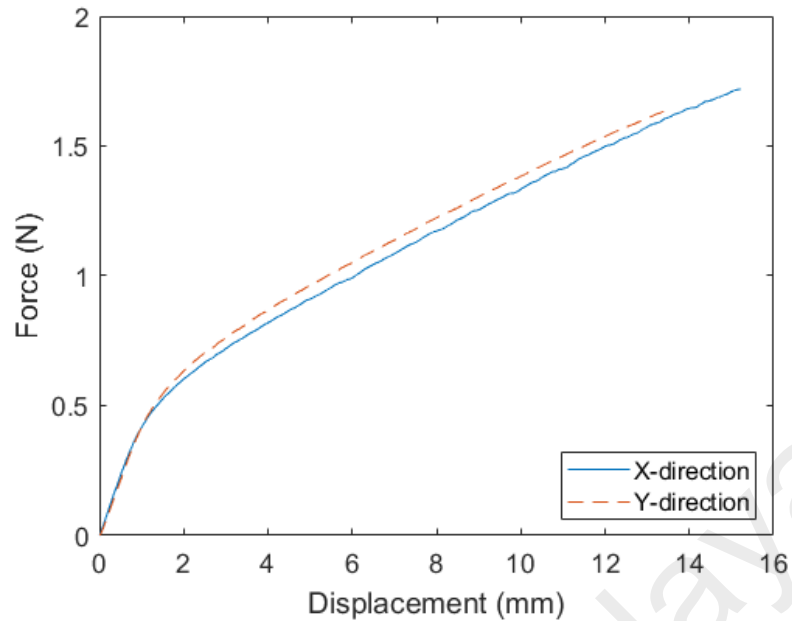


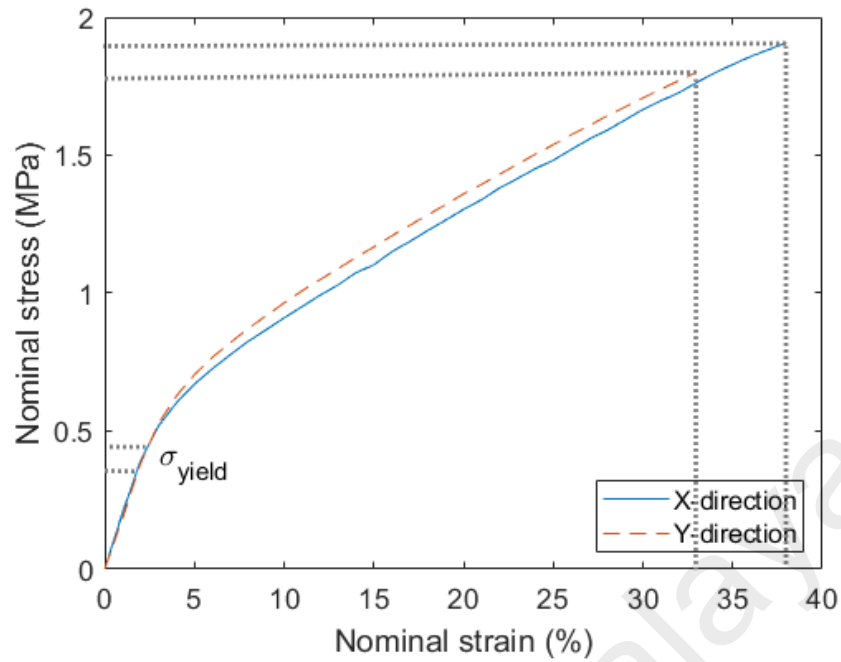
Figure 4.4: Force-displacement curves for monotonic tensile tests.

Table 4.3: Mechanical properties of electrospun PVDF membrane.

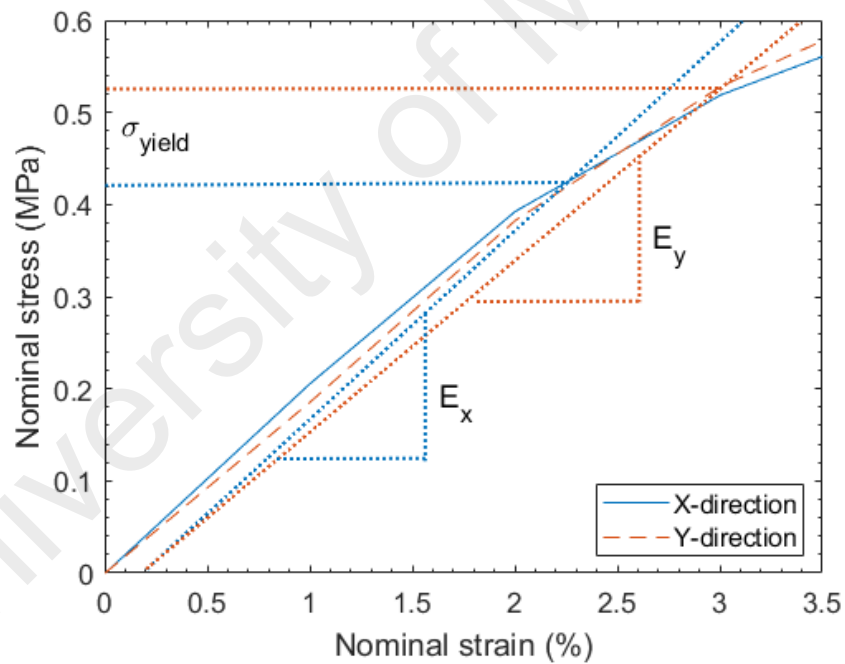
Direction of specimens	Strain at fracture (%)	Stress at fracture (MPa)	0.2% Off-set yield strength (MPa)	Young's modulus (MPa)
X	38	1.91	0.42	20.05
Y	33	1.80	0.52	19.05

From Figure 4.5 (a), the stress and strain values at fracture are determined from the end-point of the stress-strain curves. In this case, the Young's modulus is computed in the small strain region (less than 2% strain) at which the stress and strain show a linear relationship, while the yield strength is determined by means of the well-known 0.2% offset strain method since no distinct yield point is observed from the monotonic stress-strain curves (see Figure 4.5 (b)).

In general, both specimens show similar curves where the specimen exhibits a slightly higher stress-strain response in the Y-direction. At small strains, linear elastic response is observed before the materials undergo a transition to non-linear stress-strain response.



(a)



(b)

Figure 4.5: Stress-strain curves for monotonic tensile tests (a) Original scale and (b) enlarged scale.

Observations on the stress-strain responses along with the obtained mechanical properties suggest that the materials are essentially directional independent and thus can be considered as initially isotropic in the X-Y plane. Due to similar properties obtained for both tensile directions, for simplicity, only the X-direction is chosen for the following tests, i.e. cyclic

loading test with increasing maximum strain, cyclic-relaxation test and multiple-relaxation test.

4.3.2 Cyclic loading test with increasing maximum strain

For the cyclic loading test, specimens were subjected to repeated loadings and un-loadings with increasing maximum strain until the specimens fracture. Subsequently, the resulting stress-strain curve for the cyclic loading test is illustrated in Figure 4.6. During the test, buckling of the specimen was prevented by unloading the specimen to zero force instead of zero strain at the end of every cycle. However, it was noted that, at the end of the first cycle (at zero force), the specimen did not return completely to its initial length despite the specimen was unloaded to the initial force. Subsequent cycles showed a similar trend where the end-point of each cycle halted at much higher strain values than that of the previous cycles. This signified the occurrence of inelastic deformations where the material was permanently deformed under the application of force, thus the material could not return to its initial configuration at the end of the each cycle. Moreover, the inelastic deformation appears to increase with increasing maximum strain, as shown clearly in Figure 4.6. From

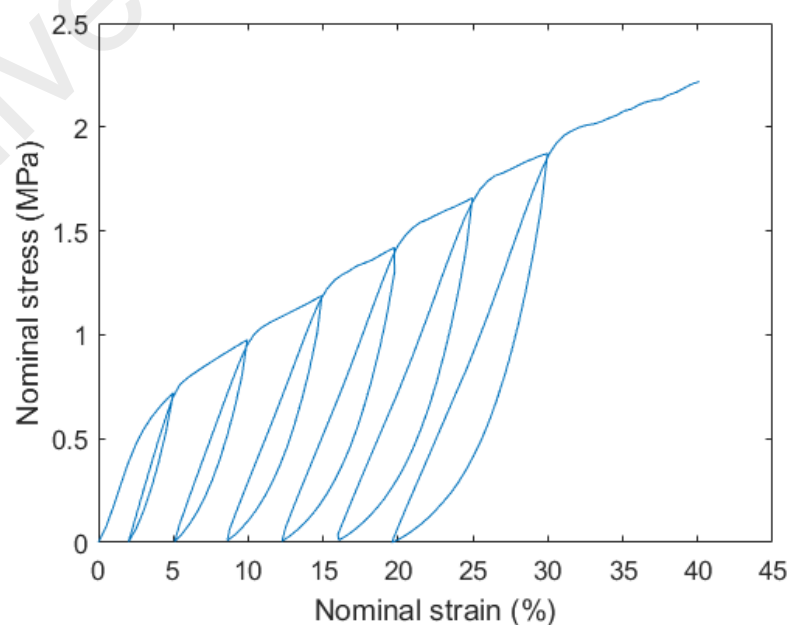


Figure 4.6: Stress-strain curve for cyclic loading test.

the stress-strain curve of the cyclic loading test, the inelastic strain and the Young's modulus for each cycle were determined as depicted in Figure 4.7. Subsequently, the inelastic strain ratio and Young's modulus ratio are computed from the data obtained. Here, the inelastic strain ratio is defined as the ratio between the inelastic strain and the corresponding maximum strain. Moreover, the Young's modulus ratio is defined by the ratio between the Young's modulus at a given cycle (given maximum strain) with that at first cycle. It is to note that for each cycle, the Young's modulus is identified by measuring the initial slope of reloading curve. Generally, the amount of inelastic strain, inelastic strain ratio, Young's modulus and Young's modulus ratio which correspond to the maximum strain of each cycle are obtained and tabulated in Table 4.4.

In order to probe closely on the nature of inelastic deformation and damage in the materials, the evolutions of inelastic strain ratio and Young's modulus ratio are plotted as a function of maximum strain. The results are depicted in Figure 4.8.

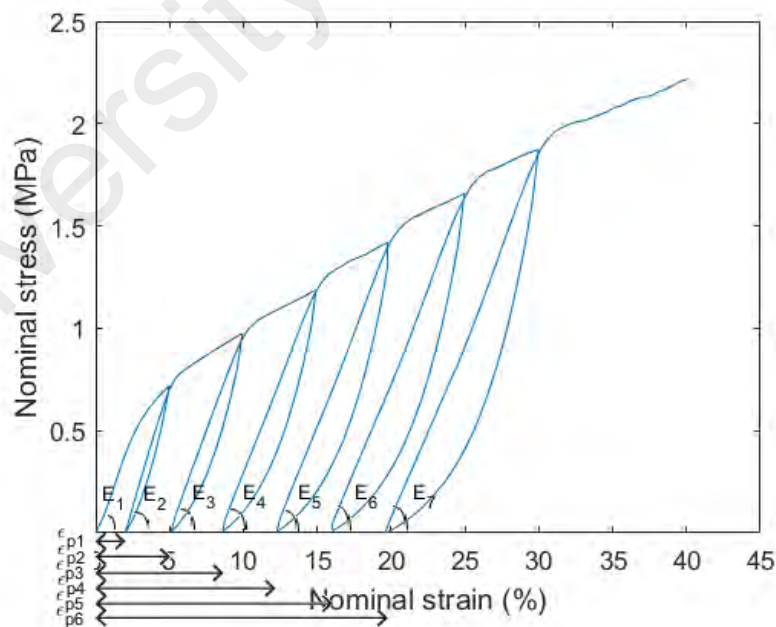


Figure 4.7: Stress-strain curve for cyclic loading test indicating inelastic strain and Young's modulus for each cycle.

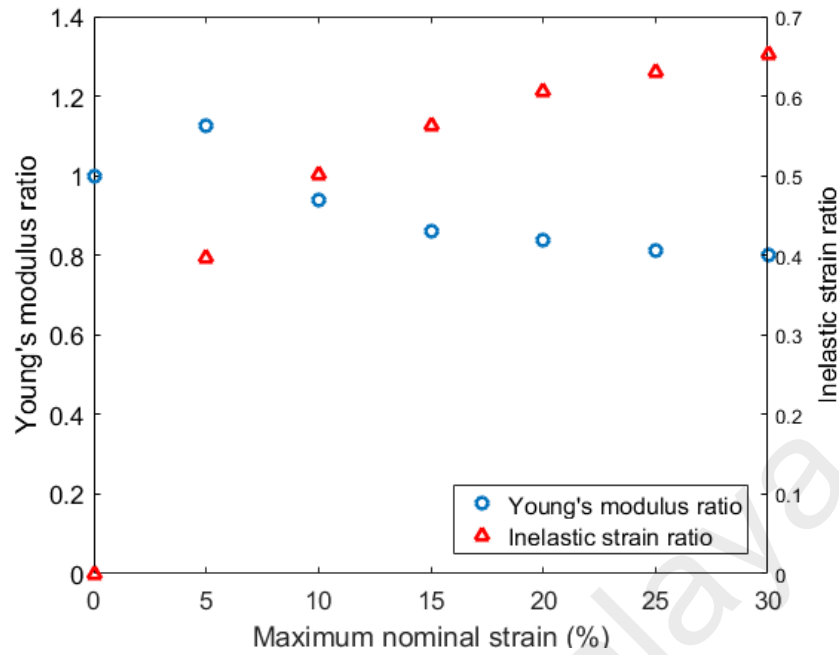


Figure 4.8: Plot of inelastic strain ratio and Young's modulus ratio versus maximum nominal strain.

Table 4.4: Inelastic deformation, inelastic strain ratio, Young's modulus and Young's modulus ratio corresponded to the maximum strains.

Maximum strain, ϵ_{max} (%)	Inelastic strain, ϵ_p (%)	Inelastic strain ratio, $\epsilon_p/\epsilon_{max}$	Young's modulus, E (MPa)	Young's modulus ratio, E_i/E_o
0	0	0	18.5	1.000
5	1.982	0.396	24.5	1.320
10	5.013	0.501	20.2	1.087
15	8.443	0.563	18.4	0.993
20	12.121	0.606	17.9	0.967
25	15.771	0.631	17.4	0.938
30	19.572	0.652	17.2	0.925

From Figure 4.8, it was observed that the inelastic strain ratio evolves nonlinearly with the maximum strain. Furthermore, the evolution of the Young's modulus ratio as a function of maximum strain firstly increases and then decreases continuously until the end of the test. The results suggest that two competing phenomena take place during the deformation of nanofibrous membranes: (1) deformation-induced fiber re-orientation (as highlighted in Section 3.2.5) resulting in higher stiffness along the stretch direction and (2) deformation-induced damage rendering to lower stiffness. According to Ridruejo et al. (2011), damage

begins at very low strains by fracture of interfiber bonds, which causes further fiber rearrangement. In our case, the deformation-induced fiber re-orientation appears to be predominant at small strains as marked by the increase in the Young's modulus. Further loading promotes greater fiber damage that cannot be overcome by the fiber re-orientation effect, resulting in the decrease in Young's modulus.

Apart from the above mentioned properties, the yield strength of the material is of great interest and its derivation is particularly important for further modeling purposes. From Figure 4.6, it was noted that the yield limit for each successive cycle increased as the maximum strain increased. In this case, the resistance of the material to inelastic deformation increased due to the increased yield limit upon each successive cycle. This phenomenon signified the occurrence of strain hardening on the deformed specimen. Subsequently, the yield strengths of the initial loading and of each reloading curve were estimated by taking the data before the onset of yield, as depicted in Figure 4.9. Inelastic flow stress was computed as the current yield strength, σ_{yi} , minus off the initial yield strength, σ_{yo} . The yield strength and inelastic flow stress corresponding to the inelastic strain for each cycle were tabulated in Table 4.5, and the inelastic flow stress was plotted as a function of inelastic strain, as depicted in Figure 4.10.

Table 4.5: Inelastic deformation, yield strength and inelastic flow stress.

Inelastic strain, ϵ_p (%)	Yield Strength, σ_y (MPa)	Inelastic flow stress, $\sigma_{yi} - \sigma_{yo}$ where $i = 1, 2, 3, 4, 5, 6$
0	0.387	0
1.982	0.707	0.320
5.013	0.970	0.583
8.443	1.179	0.792
12.121	1.4156	1.031
15.771	1.650	1.263
19.572	1.870	1.483

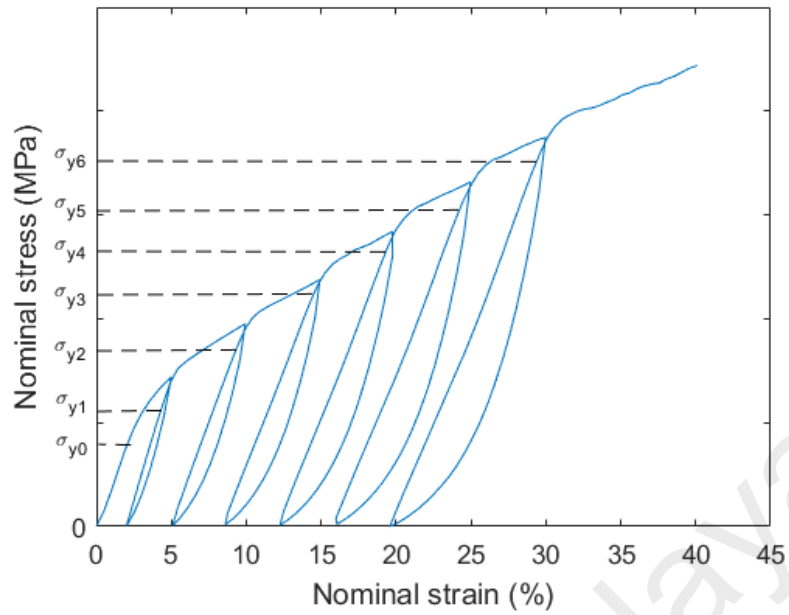


Figure 4.9: Cyclic loading stress-strain curve indicating the yield limit for each cycle.

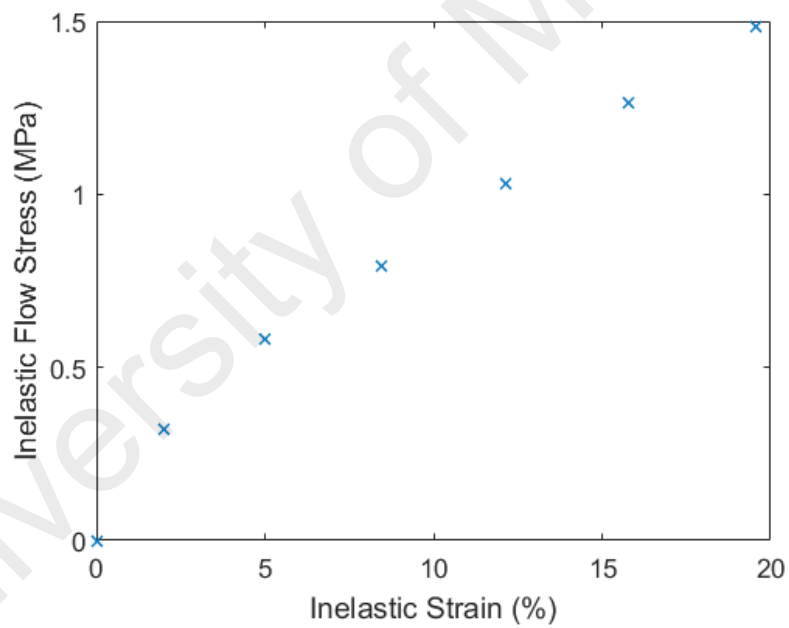


Figure 4.10: Plot of inelastic flow stress versus inelastic strain.

Inelastic flow stress is the instantaneous stress required to continuously deform the material in an inelastic manner. Figure 4.10 allows us to investigate how hardening evolved as a function of the inelastic strain. It is then observed that strain hardening increased with the inelastic strain until the fracture of the specimen.

4.3.3 Cyclic-relaxation test

The time-dependent characteristic of electrospun PVDF nanofibrous membranes was investigated, in which the loading and unloading stages were interrupted by a number of stress relaxation tests (see Figure 3.6). The entire investigation was carried out below the fracture strain of the material. For each relaxation segment, the specimen was held at constant strain for duration of 15 minutes. The resulting stress-strain curve is plotted in Figure 4.11.

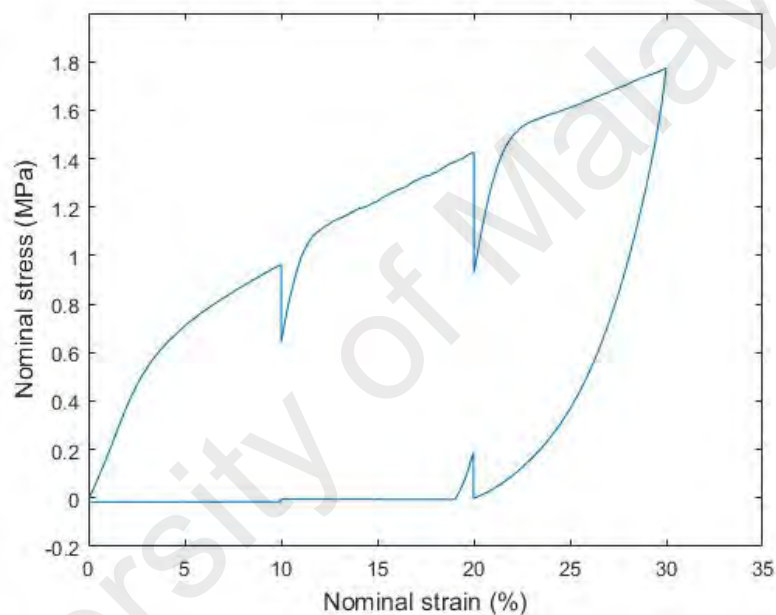


Figure 4.11: Stress-strain curve for cyclic-relaxation test.

From Figure 4.11, the stress decreases during unloading and increases during loading for the relaxation parts of the test. The time-dependent behavior appears to be more significant during the unloading than during the loading. Subsequently, similar findings can be observed in rubber materials by Lion (1996), Bergström & Boyce (1998) and in fiber reinforced thermoplastics by Andriyana et al. (2010). It is to note that only one stress relaxation at 20% strain is clearly observed for the unloading part as compared to the two stress relaxation at 10% and 20% for the loading section. Unlike the previous cyclic loading test, a purely strain-controlled process was utilized in conducting the cyclic-relaxation test.

Thus, relaxation at 10% strain during unloading could not be observed due to the buckling of the specimen (material experiences inelastic deformation, see Figure 4.12).



Figure 4.12: Buckling of specimens at the end of cyclic-relaxation tests.

Subsequently, the stress values for the relaxation segments are extracted and the evolution of stress during relaxations are presented in Figure 4.13. From Figure 4.13, the first and second relaxations correspond to the relaxations during uploading at 10% and 20% strains respectively, while the third relaxation represents the relaxation at 20% strain during unloading. Figure 4.13 shows that the stress approaches to what appears to be an equilibrium state after 15 minutes of relaxation duration. Furthermore, the rate of approach towards this relaxed state is a decreasing function of the relaxation duration. According to Lion (1996), the corresponding behavior was characterized by the existence of a so-called equilibrium hysteresis in the case of bulk rubber materials. Thus, no unique equilibrium state where the stress response was controlled solely by the strain state exists and consequently, hysteresis may be associated with viscoplasticity. Nevertheless, Bergström & Boyce (1998) inferred the existence of a unique equilibrium state that can be reached in the limit of infinite relaxation duration. In this case, the authors attributed hysteresis in rubbers to viscoelasticity.

In order to further investigate the time-dependent response of the electrospun PVDF

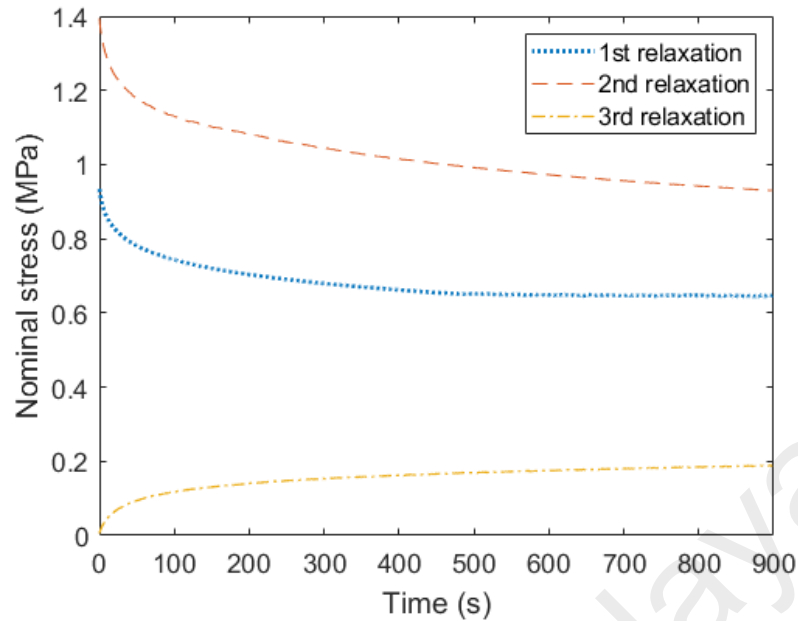


Figure 4.13: Evolution of stress as a function of relaxation duration during the relaxation test.

nanofibrous membranes, the normalized stress for the first and second relaxations are computed through the ratio of the stress level at that time to the initial stress value for the corresponding relaxation stage. Subsequently, the normalized stress is plotted as a function of the relaxation duration as illustrated in Figure 4.14. As observed in this figure, it appeared that the two curves are superimposed. The result suggests that the kinetics of stress-relaxation is essentially independent of the strain level at which the relaxation test was conducted, i.e. linear time-dependent response.

4.4 Volume change of electrospun PVDF membranes

The volume change and Poisson's ratio of the representative $P_{15}V_{20}$ sample were investigated for membranes of three different electrospinning durations, i.e. 10 hours (initial duration), 15 hours and 20 hours. Recall that the initial thickness of specimens was measured using a Mitutoyo measuring gauge. The average thickness from all three positions of three specimens (nine readings) was computed with the standard error of mean, and are presented in Table 4.6 for all the three samples, i.e. PVDF10, PVDF15 and PVDF20.

Table 4.6 shows that a significant difference in thickness can be obtained when the

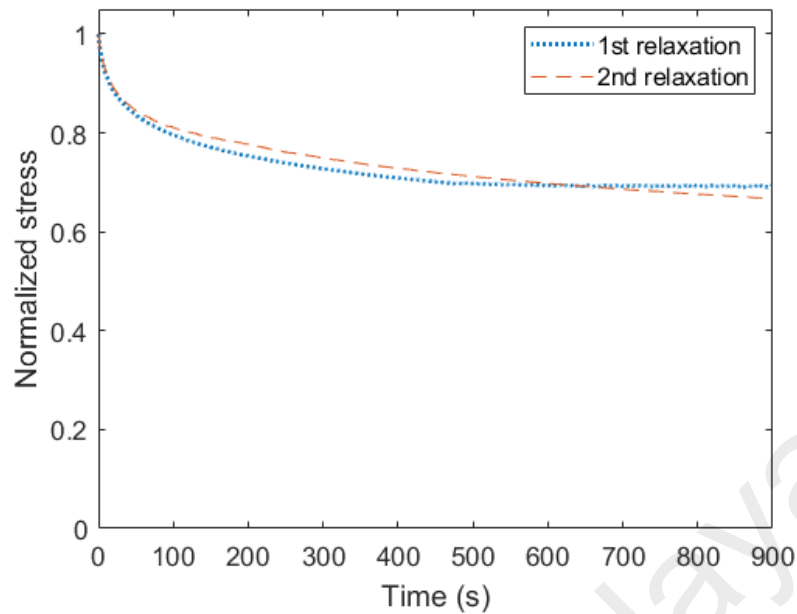


Figure 4.14: Normalized stress as a function of relaxation duration during relaxation tests.

Table 4.6: Initial thickness of three electrospun PVDF samples.

Sample	Membrane thickness (mm)		
	PVDF10	PVDF15	PVDF20
PVDF	0.1481 ± 0.0083	0.1988 ± 0.0031	0.2496 ± 0.0046

electrospinning duration was increased at five hours intervals, from 10 hours to 15 hours and lastly to 20 hours. At first, the electrospinning duration of 10 hours was adopted in order to produce sufficient membrane thickness for the easy handling of specimens during mechanical testing. It is noticed that the membrane thickness is proportionally related to the electrospinning duration, and thus increasing the electrospinning duration increases the membrane thickness. However, electrospinning duration of more than 20 hours might not be feasible due to the decreased conductivity of the metal collector, since a large amount of fibers have been deposited and covered the conductive surface.

For the determination of the volume change, the widths and thicknesses were recorded for all three positions as stated in Figure 3.7, i.e. bottom, middle and top, at strain levels of 0%, 5%, 10% and 20%, for all the specimens investigated. Subsequently, the volume at each position was computed through the multiplication of length, width and thickness

(length \times width \times thickness), and the average volume of each specimen was computed from the volumes at the three positions, for every particular strain level. Following this, the average volume ratio was computed as the ratio between the average volume at particular strain with the initial average volume. Finally, the mean with standard error of mean of average volume ratio from three specimens was computed for every sample. In order to probe closely the volume change for three PVDF samples, the evolution of average volume ratio (V/V_0) is plotted as a function of the nominal strain, as depicted in Figure 4.15.

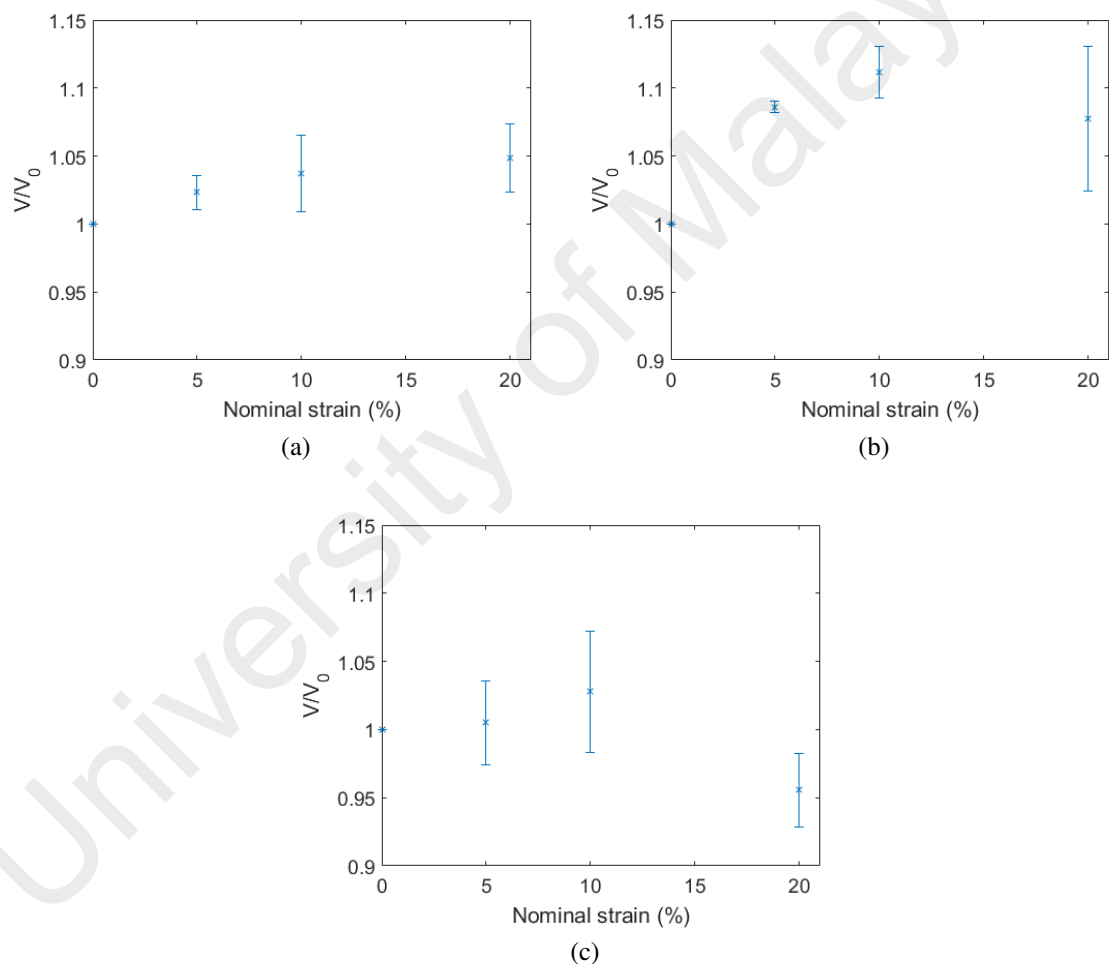


Figure 4.15: Plots of average volume ratio versus nominal strain for (a) PVDF10, (b) PVDF15 and (c) PVDF20.

Figure 4.15 shows the volume change for electrospun PVDF membranes of three different samples fabricated from different electrospinning durations. Generally, volume changes of up to 14% exists when electrospun PVDF membranes are deformed under uni-

axial extension. From Figure 4.15 (a), the average volume ratio increases gradually from 0% to 20% nominal strain. Whereas in Figure 4.15 (b), the average volume ratio increased substantially at the beginning but decrease gradually towards the end of mechanical deformation. Lastly in Figure 4.15 (c), the average volume ratio increases slowly towards 10% strain but decreases from 10% to 20% strain in a larger magnitude as compared to the increment at the former part. The decrease in average volume ratio denotes a reduction in the average volume of the specimens. Overall, there is no general trend in the volume change of electrospun PVDF samples of different thicknesses.

Throughout the analysis, the overall membrane volume can be simply divided into the volume of fibers and the volume of porosity (gaps or spaces between fibers). Recalling the results in Section 4.2.1, it is believed that the significant reduction in the fiber diameter of approximately 23% in PVDF10 constitutes to the reduction in the fiber volume, while the increase in pore diameter of approximately 52% leads to an increase in the porosity volume. The combined effects of both are reflected in Figure 4.15 (a), where a gradual increase is shown in the overall membrane volume. Knowing that the fibers reduce in volume, the overall increment in membrane volume in PVDF10 (Figure 4.15 (a)) is therefore the contribution of pore diameter increment.

Previously, it is assumed that similar electrospinning parameters produce electrospun membranes of similar fiber size and surface morphology, regardless of the duration of electrospinning. Despite the similarities assumed in PVDF10, PVDF15 and PVDF20, the volume changes in PVDF15 (Figure 4.15 (b)) and PVDF20 (Figure 4.15 (c)) appear to behave differently than that observed in PVDF10 (Figure 4.15 (a)). Assuming that the fibers deform similarly in all three PVDF samples, the discrepancies in the volume change are most likely due to the contribution of the porosity volume. Subsequently, it is suggested that an increasing membrane thickness modifies the kinetics of pore growth on deformations, where pore grows slower as membrane thickness increases. The degree of the pore volume

growth could not compensate for the reduction in the fiber volume, leading to the reduction in overall membrane volume especially for the case of PVDF20 (Figure 4.15 (c)). However, the details on the kinetics of pore growth is still unclear. The observed phenomenon might arise due to the nature of the PVDF material, or other uncertainties during characterization processes such as specimens handling or measurement on the specimens which were difficult to be justified, since electrospun PVDF membranes are always fragile and difficult to handle.

Generally, the volume change of electrospun PVDF membranes can be attributed to the materials or structural changes, or even the combination of both. Yet, the complexities in microstructure and deformation mechanisms that arise from the deformation of individual fibers, deformation at inter-fiber junctions, re-orientation of fibers and changes in porosities might overall contribute to the volume change of the structures. These complexities are difficult to trace and their combined effect is difficult to be separated during mechanical testing which render the reason of the volume change inconsistencies in PVDF membranes remain unconfirmed.

4.5 Poisson's ratio of electrospun PVDF membranes

Recall that for each PVDF sample, three specimens were extracted for the mechanical test in order to determine the volume change as well as the magnitudes of Poisson's ratio. Subsequently, data on the changes in widths and thicknesses was converted into λ_2 and λ_3 respectively, while λ_1 is computed from the magnitude of imposed deformations. The in-plane and out-of-plane Poisson's ratios can be determined respectively through the plots of $\ln \lambda_2$ versus $\ln \lambda_1$ and $\ln \lambda_3$ versus $\ln \lambda_1$. Here, linear curves with zero intercept are fitted to the plots of $\ln \lambda_2$ and $\ln \lambda_3$ versus $\ln \lambda_1$, and the slopes of the linear curves will be the magnitudes of Poisson's ratio. Subsequently, the determinations of in-plane and out-of-plane Poisson's ratio are tabulated in the following sections.

4.5.1 In-plane Poisson's ratio

Three specimens were investigated for each electrospun PVDF sample. For each specimen subjected to mechanical deformation and measurement of dimensional changes, λ_2 is computed at three different locations, i.e. "top", "middle" and "bottom" (recall Figure 3.7). The average of λ_2 from three different locations are computed for each specimen.

Subsequently, the average results of $\ln \lambda_2$ versus $\ln \lambda_1$ for three specimens were plotted for each PVDF samples, i.e. PVDF10, PVDF15 and PVDF20 as illustrated in Figure 4.16. For each plot (each PVDF sample), the data was fitted with a linear curve with zero intercept in order to determine the magnitude of the in-plane Poisson's ratio. The in-plane Poisson's ratios obtained are tabulated in Table 4.7.

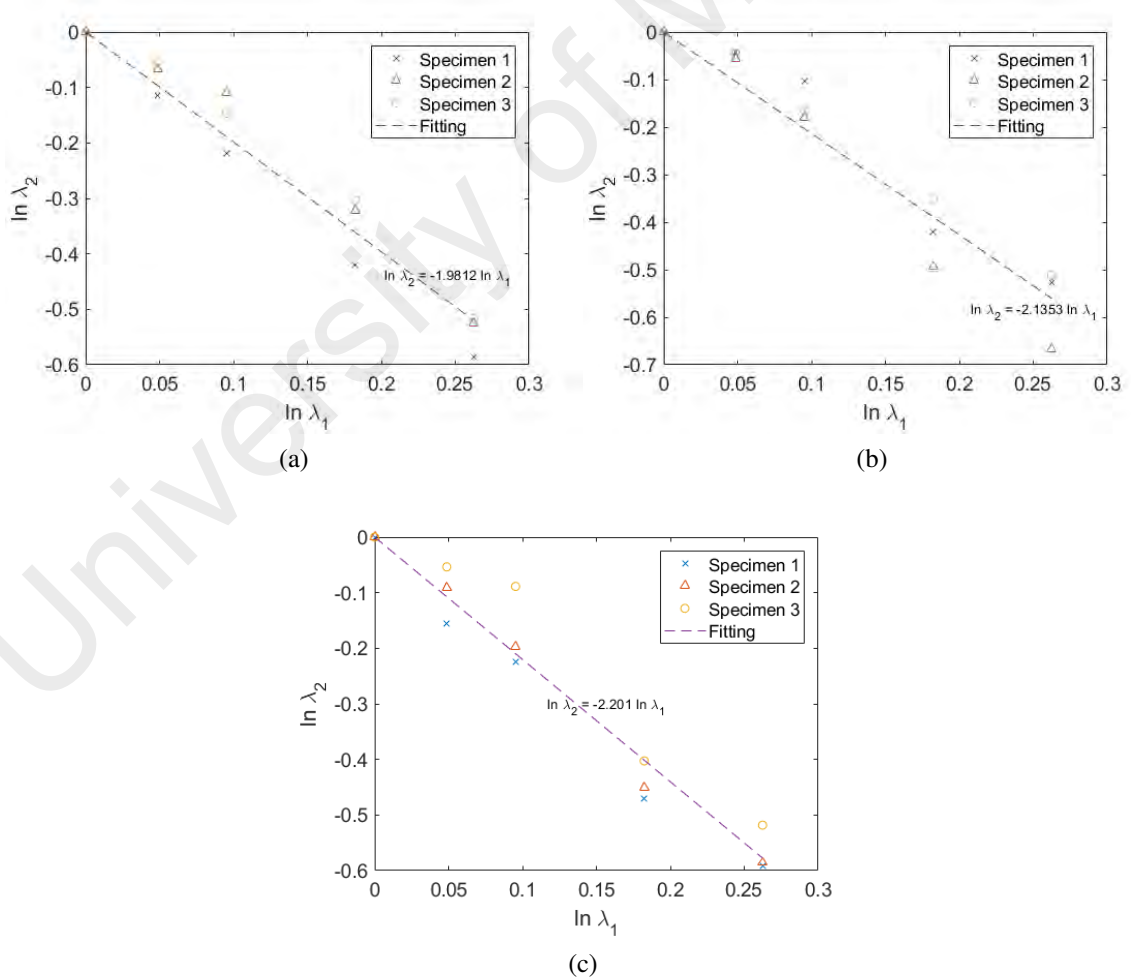


Figure 4.16: Determination of the in-plane Poisson's ratio for electrospun (a) PVDF10, (b) PVDF15 and (c) PVDF20 samples.

From Table 4.7, the in-plane Poisson's ratio is found to range from 1.9812 to 2.201. This range of values takes into account the Poisson's ratio obtained from each particular positions, from all the electrospun PVDF specimens being investigated. Generally, a slight increment in the average values of Poisson's ratio is observed from PVDF10 to PVDF20, as the thickness of the membranes increases. However, the increment is insignificant and therefore, it is assumed that the membrane thickness does not significantly affect the values of the in-plane Poisson's ratio. Furthermore, the results obtained for electrospun PVDF membranes show peculiar values of Poisson's ratio which are extremely different from those of the conventional bulk PVDF material (with Poisson's ratio of approximately 0.38) (Laiarinandrasana & Hochstetter, 2006). Besides, the values obtained also show that the rate of decrement in width is higher than the rate of membrane elongation in axial direction. Generally, randomly oriented electrospun nanofibrous membranes possess unique structures and fibers assembly which are different from the conventional bulk materials. It is believed that the combined effects of both precursor material and assemblies of structures in electrospun nanofibrous membranes constitute to the values of Poisson's ratio as shown in Table 4.7. This information of the in-plane Poisson's ratio will be useful later in the prediction of the in-plane mechanical response of randomly oriented electrospun PVDF membranes.

4.5.2 Out-of-plane Poisson's ratio

Similar to the practice in Section 4.5.1, the out-of-plane Poisson's ratio can be computed through the plots of $\ln \lambda_3$ versus $\ln \lambda_1$. Here, Poisson's ratio exists as a constant value illustrating the gradual changes in thickness with respect to the applied axial deformation. Similarly to Section 4.5.1, λ_3 is computed at three different locations, i.e. "top", "middle" and "bottom" (recall Figure 3.7), and the average of λ_3 from three different locations are computed for each specimen.

Subsequently, the average results of $\ln \lambda_3$ versus $\ln \lambda_1$ for three specimens were plotted for each PVDF samples, i.e. PVDF10, PVDF15 and PVDF20 as illustrated in Figure 4.17. For each plot (each PVDF sample), the data was fitted with a linear curve with zero intercept in order to determine the magnitude of the out-of-plane Poisson's ratio. The out-of-plane Poisson's ratios obtained are tabulated in Table 4.7.

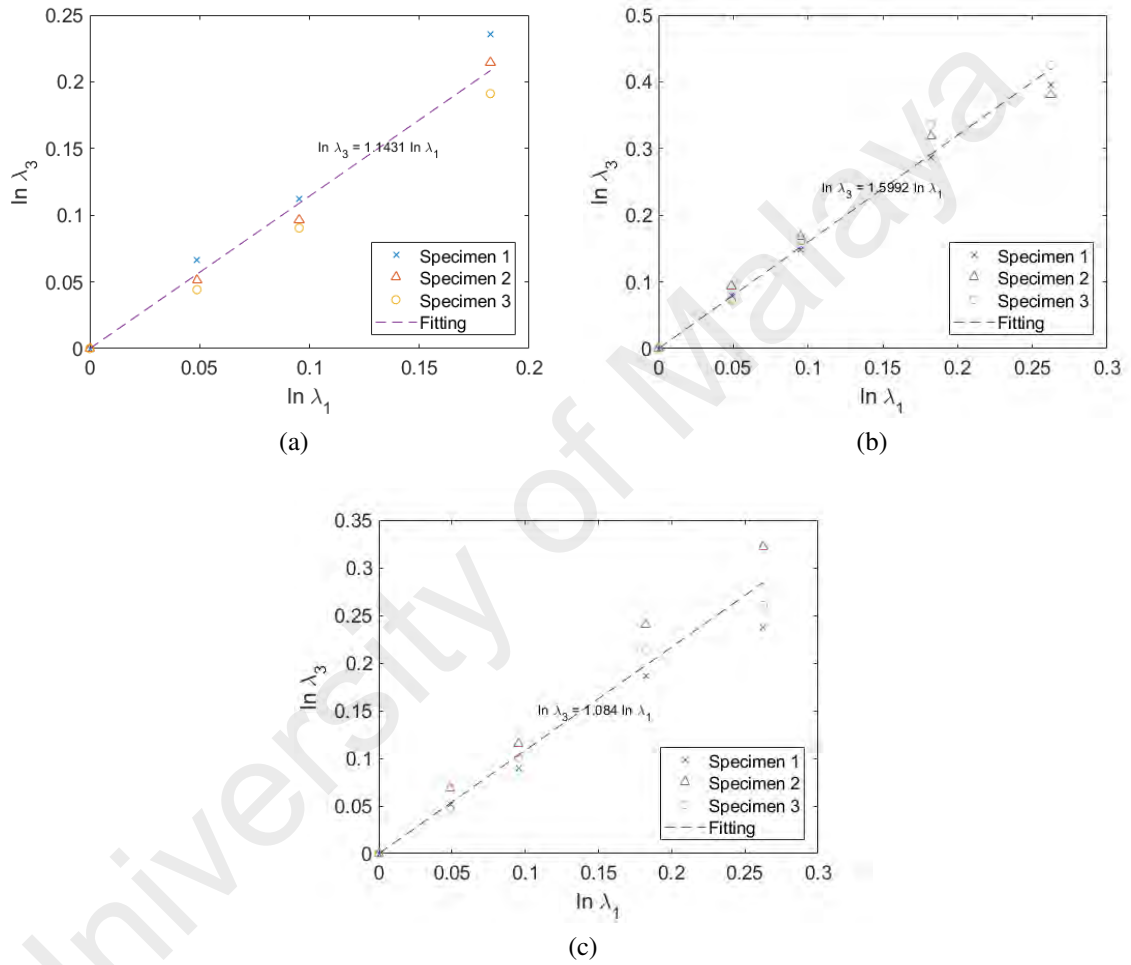


Figure 4.17: Determination of the out-of-plane Poisson's ratio for electrospun (a) PVDF10, (b) PVDF15 and (c) PVDF20 samples.

From Table 4.7, the values of the out-of-plane Poisson's ratio for electrospun PVDF membranes range from -1.084 to -1.5992. The negative sign here indicates that the thickness of specimens increases with the applied mechanical deformation, i.e. the structures are auxetics. It is observed that sample PVDF15 possess slightly higher values as compared to samples PVDF10 and PVDF20. In general, the value increases from PVDF10 to PVDF15,

and decreases from PVDF15 to PVDF20. This suggests that the overall changes in thickness is greater for sample PVDF15 upon the axial deformation of the specimens. At the moment, it is still unclear why the PVDF15 sample shows deviant values of out-of-plane Poisson's ratio from the other two PVDF samples. However, the reason should be related to the discrepancies in volume changes of PVDF samples as discussed earlier in Section 4.4.

Here, it is suggested that the unique structures or assemblies of the electrospun nanofibrous membranes contribute to the increment of membrane thickness with applied deformation. In randomly oriented electrospun membranes, more fibers tend to realign along the direction of applied deformation as the imposed strain increases. Therefore, the increment of membrane thickness is accompanied by the fiber re-orientation during the application of in-plane uniaxial deformation, such that the increase in thickness is due to the re-orientation of fibers. Further work is needed in the future to validate this statement.

Table 4.7: Poisson's ratio of electrospun PVDF membranes, for three different membrane thicknesses.

Sample	PVDF10	PVDF15	PVDF20
In-plane Poisson's ratio	1.9812	2.1353	2.201
Out-of-plane Poisson's ratio	-1.1431	-1.5992	-1.084

4.6 Fiber orientation analysis

Fiber orientation analysis was conducted to determine the evolution of the fiber orientation as a function of the applied tensile strain. In Section 3.3, electrospun PVDF nanofibrous specimens were subjected to different levels of maximum tensile strain, i.e. 5%, 10%, 20% and 25% to examine the deformation-induced fiber re-orientation phenomenon on the material. For this purpose, the results of 35 SEM images were analyzed for each maximum strain (including the undeformed 0% strain) to improve the accuracy of the data, by utilizing the ImageJ software with OrientationJ plugin. An example of SEM images of different

maximum tensile strains subjected to fiber orientation analysis are presented in Figure 4.18. The average fiber orientation distribution of 35 SEM images and their normalized counterpart were computed for each maximum strain. Here, the normalized fiber orientation distribution is defined as the ratio of fiber orientation distribution at a particular fiber angle to the sum of fiber orientation distribution of all angle for the corresponding maximum strain. Subsequently, the standard deviation as well as standard error of the mean corresponding to the normalized fiber orientation distribution were determined for each maximum tensile strain.

Eventually, the curves of the normalized fiber orientation distribution with and without standard error of mean and the component of fiber orientation tensor along tensile direction (A_{11}) calculated using Equation 3.4 are depicted in Figure 4.19, Figure 4.20 and Figure 4.21 respectively. Considering the deformation mechanism presented in Figure 3.8, all results correspond to the intermediate or unloaded configuration of the deformed materials.

Note that the 0-degree orientation in Figure 4.18, Figure 4.19 and Figure 4.20 corresponds to the direction of specimen stretching. A small peak is observed around -40 -degree orientation from both Figure 4.19 and Figure 4.20 for the initial undeformed material. Even though most of the fibers appear to be oriented along the -40 -degree direction, the discrepancies between various directions are not significant resulting to the initial macroscopic mechanical properties that are nearly independent of direction as previously discussed in Section 4.3.1. As the material was stretched to larger strain, the peak shifted slowly to the right and eventually halted around 0-degree orientation, i.e. the direction of applied strain. The evidence suggests that a deformation-induced fiber re-orientation phenomenon takes place. More fibers are realigned along the direction of stretching as the imposed strain increases. This phenomenon can again be clearly seen from Figure 4.18 where more fibers appear in light blue color (0-degree orientation) as the imposed maximum strain increases, indicating the re-orientation of fibers with deformation.

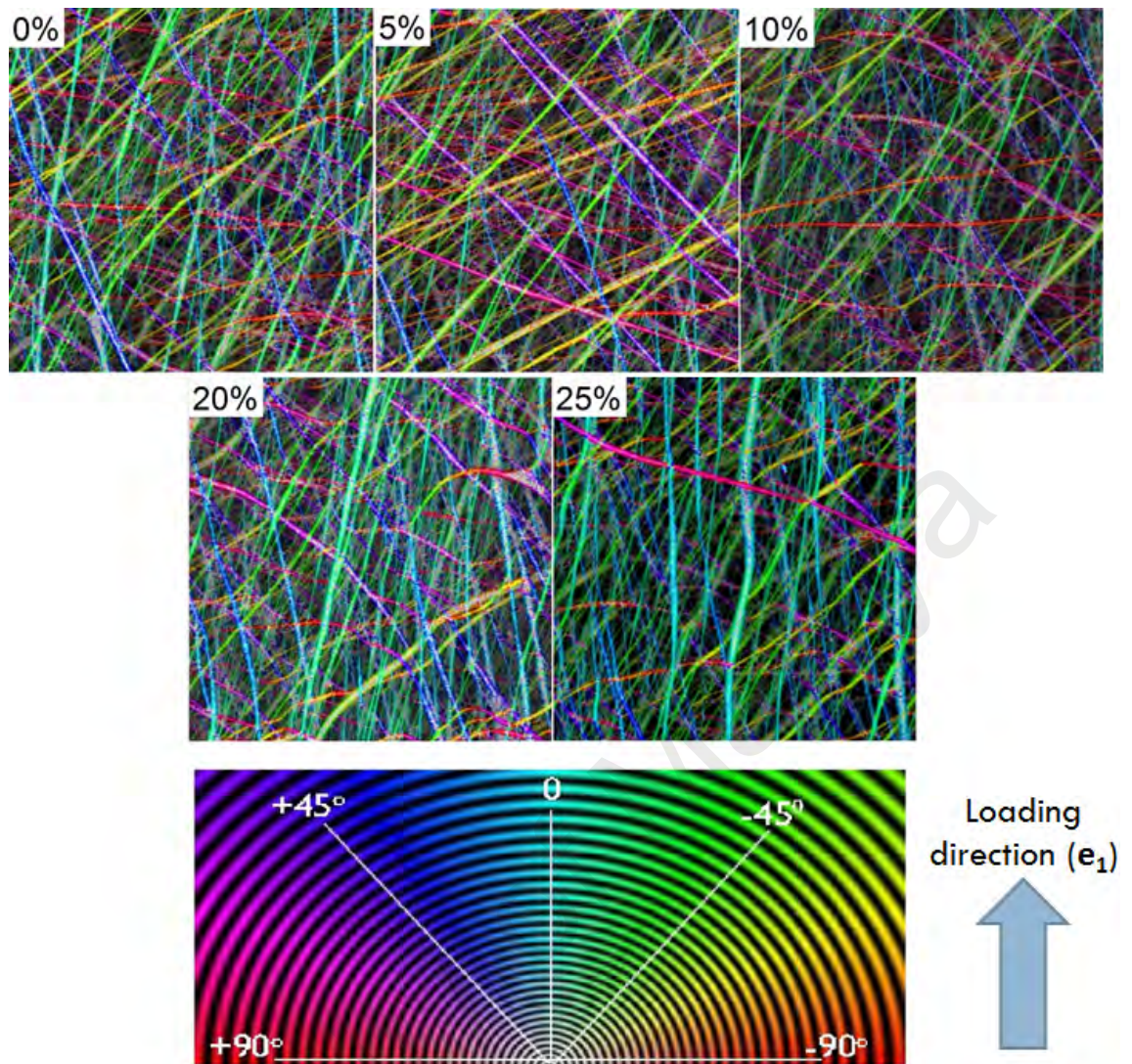


Figure 4.18: Example of SEM images of different maximum strain levels subjected to fiber orientation analysis.

The deformation-induced fiber re-orientation can also be probed through the plot of component of fiber orientation tensor along tensile direction (A_{11}) as a function of inelastic strain, as depicted in Figure 4.21. The figure suggests that the fibers are statistically oriented uniformly in all directions along the plane of the membrane at the undeformed state of the material. The component A_{11} appears to evolve essentially in a linear way with the inelastic strain. Recalling Figure 4.8, the Young's modulus increased up to around 5% strain before it dropped with a decreasing rate towards the fracture of the material. This phenomenon suggests that the rate of interfiber bond damage is relatively low at lower strain before increasing at the higher strain level. Further investigations are essential in

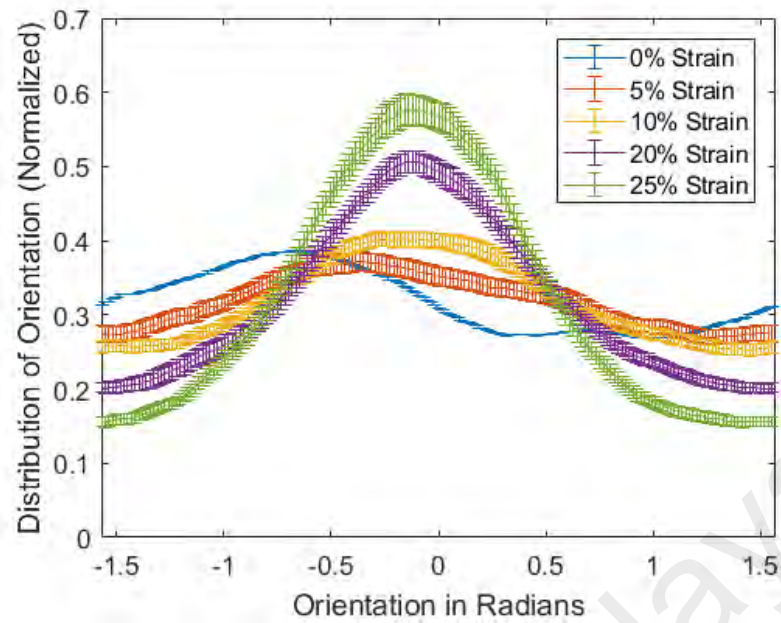


Figure 4.19: Fiber orientation distribution \pm standard error of mean for different applied maximum strain values.

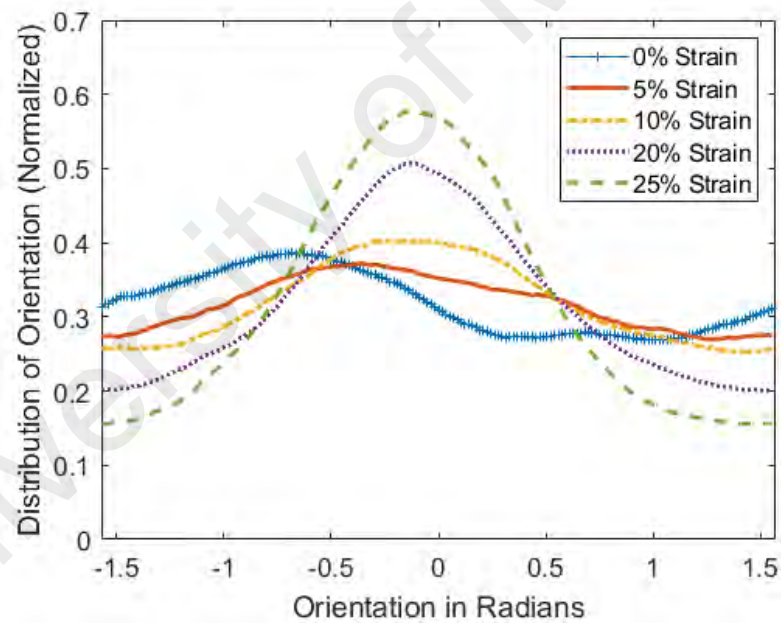


Figure 4.20: Fiber orientation distribution curves for different applied maximum strain values.

order to fully understand the deformation-induced fiber re-orientation and deformation-induced fiber damage phenomena in electrospun nanofibrous membrane.

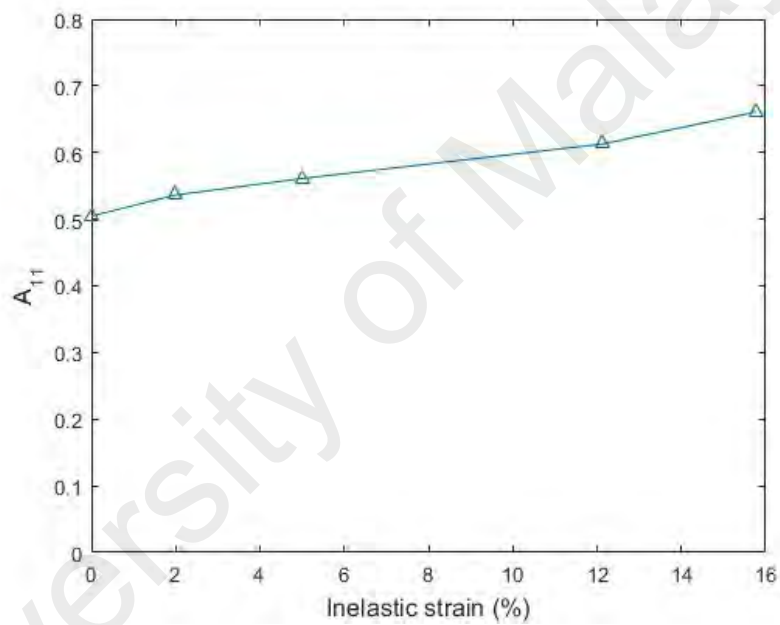


Figure 4.21: Evolution of the component of fiber orientation tensor along tensile direction (A_{11}) as a function of inelastic strain.

CHAPTER 5: MODELING RESULTS AND DISCUSSION

The general description of deformation and stress-strain response for constitutive model of electrospun nanofibrous membranes has been proposed earlier in Section 3.3. In this section, modeling of the mechanical response proceeds into the detailed derivation of the stress in the fibers, following by the particularization of the model for the special case of uniaxial extension of 2D membranes. Subsequently, the proposed constitutive model is employed for a series of simulations by utilizing MATLAB software.

5.1 Derivation of the stress in fibers

As highlighted in the previous section, the stress response in Eq. (3.12) is completely defined if w is postulated so that the true fiber stress can be determined via Eq. (3.11). For this purpose, a simple rheological model is proposed at the fiber scale to describe the fiber scale stress response. Recall that Baji et al. (2010) listed four factors that influence the mechanical properties of electrospun membranes, i.e. (1) fiber structural morphology, (2) geometrical arrangement of fibers, (3) individual fiber properties and (4) interaction between fibers. The fiber structural morphology refers to the morphology down to molecular scale in the fiber and is therefore omitted in this work. For the geometrical arrangement of fibers, the present work focuses on randomly oriented electrospun nanofibrous membranes. Following this, it is assumed that the overall fiber response is governed by two main contributions: (1) stiffness of the individual fiber and (2) irreversible fiber-fiber interactions (for example the physical junctions and the electrostatic forces of attractions between fibers as discussed in the previous Section). Subsequently, the fiber response is illustrated through the rheological model presented in Figure 5.1.

Along this line, a nonlinear spring (elastic component) is adopted to represent the response of the individual fiber, while a linear spring in series with a skidding block and a linear spring in parallel (elasto-plastic component) is utilized to account for the irreversible

inter-fiber interactions. The overall fiber response is characterized by the parallel arrange-

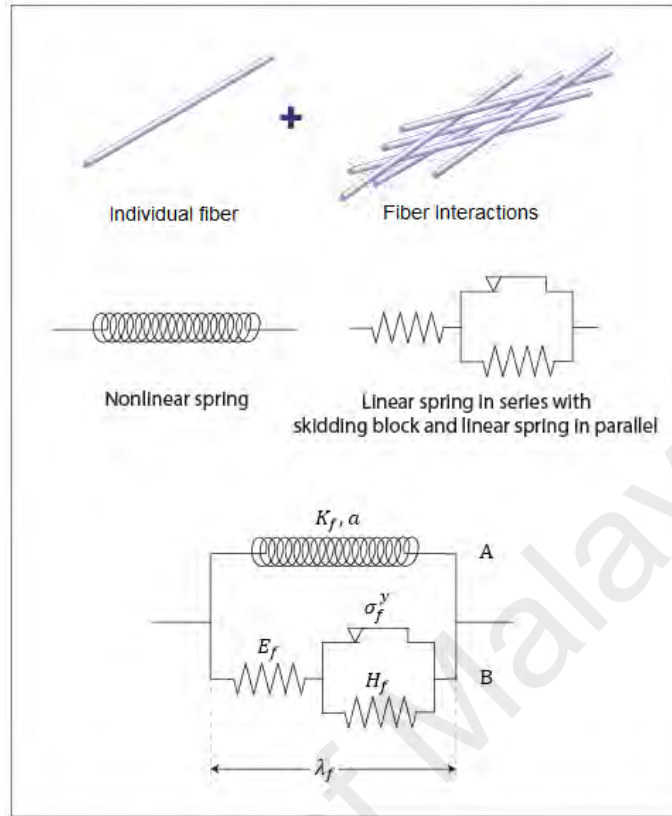


Figure 5.1: Schematic illustration of the rheological model for interacting fibers.

ment of the two components. In this work, the elasto-plastic component is used to represent the fiber scale interactions instead of the molecular scale interactions as in Planas et al. (2007). Electrospun PVDF membranes exhibit strong time-dependent response as observed from the experimental results. However, the time-dependent response is ignored in the modeling part due to the aim of developing a simple phenomenological model. Since large strain is observed from the mechanical testing of electrospun nanofibrous membrane (from the results of mechanical characterization), true stress instead of nominal stress is used for the description of the fiber scale deformation. Moreover, the multiplicative split of stretch is adopted. These features differentiate our model from the work of Planas et al. (2007).

The fiber stretch λ_f^θ is decomposed multiplicatively as follow:

$$\lambda_f^\theta = \lambda_{f,e}^\theta \lambda_{f,i}^\theta \quad (5.1)$$

where $\lambda_{f,e}^\theta$ and $\lambda_{f,i}^\theta$ are the elastic and inelastic parts of the fiber stretch respectively. More precisely, the latter transforms conceptually the fibers from the reference configuration to the intermediate (unloaded) configuration. In view of determining the true fiber stress σ_f^θ , the following form of w^θ is postulated:

$$w = \widehat{w}(\lambda_f^\theta, \lambda_{f,e}^\theta) = w^A(\lambda_f^\theta) + w^{B1}(\lambda_{f,e}^\theta) + w^{B2}(\lambda_{f,i}^\theta) \quad (5.2)$$

where w^A (defined per unit volume of the reference configuration) is the strain energy of branch A. w^{B1} (defined per unit volume of the intermediate configuration) and w^{B2} (defined per unit volume of the reference configuration) are the strain energy of branch B associated with the first spring and second spring (in parallel with the skidding block) of the rheological model respectively. Using Eqs (3.11) and (5.1), the true fiber stress becomes:

$$\sigma_f^\theta = \sigma_f^{\theta,A} + \sigma_f^{\theta,B} \quad (5.3)$$

where $\sigma_f^{\theta,A}$ and $\sigma_f^{\theta,B}$ are the true fiber stress of branch A and branch B respectively. They are given by:

$$\sigma_f^{\theta,A} = \lambda_f^\theta \frac{\partial w^A}{\partial \lambda_f^\theta} \quad \text{and} \quad \sigma_f^{\theta,B} = \lambda_{f,e}^\theta \frac{\partial w^{B1}}{\partial \lambda_{f,e}^\theta} = \sigma_f^y + \lambda_f^\theta \frac{\partial w^{B2}}{\partial \lambda_{f,i}^\theta} \quad (5.4)$$

where σ_f^y is a material constant of the skidding block that represents the initial threshold stress of inelastic deformation (yield stress).

5.2 Form of material functions

In the following, the specific forms of w^A and w^B are formulated. Referring to Figure 5.1, branch A represents the response of an individual fiber. In order to describe the non-linear stress-stretch characteristic of individual fiber, the following nonlinear strain energy function is adopted:

$$w^A = \frac{K_f}{a+1} (\lambda_f^\theta - 1)^{a+1} \quad (5.5)$$

and the resulting true fiber stress response is simply given by:

$$\sigma_f^{\theta,A} = K_f \lambda_f^\theta (\lambda_f^\theta - 1)^a \quad (5.6)$$

where K_f stands for the fiber stiffness and a is the shape control constant for the stress-stretch relationship. This relation holds for $\lambda_f^\theta \geq 1$.

Besides, the present work aims to model the irreversible deformation of the electrospun nanofibrous structures as a consequence of irreversible inter-fiber interactions, represented by Branch B in Figure 5.1. The mechanism of such irreversible interactions may be complex and therefore, for simplicity, the classical rate-independent elasto-plastic framework with linear isotropic hardening is adopted to describe such interactions. Since the corresponding interactions might involve more than just plastic deformation, in the following we use the term inelastic strain for any strain that occurs due to irreversible interactions among the fibers. Moreover, the time-dependent response is neglected in the present work.

Subsequently, linear stress response is chosen for the two elastic springs in Branch B (Figure 5.1) and the strain energy function associated with Branch B is assumed to have the following form:

$$w^{B1} = \frac{E_f}{2} (\ln \lambda_{f,e}^\theta)^2 \quad \text{and} \quad w^{B2} = \frac{H_f}{2} (\ln \lambda_{f,i}^\theta)^2 \quad (5.7)$$

and the resulting elastic fiber stress is given by

$$\sigma_f^{\theta,B} = E_f \ln \lambda_{f,e}^{\theta} = E_f \ln \left(\frac{\lambda_f^{\theta}}{\lambda_{f,i}^{\theta}} \right) = \sigma_f^y + H_f \ln \lambda_{f,i}^{\theta} \quad (5.8)$$

where E_f is a material parameter. Moreover, H_f is a parameter akin to hardening modulus in the classical theory of plasticity. The yield-like function that signifies the occurrence of inelastic deformations can be expressed as

$$f(\sigma_f^{\theta,B}) = |\sigma_f^{\theta,B}| - (\sigma_f^y + H_f \alpha) \quad (5.9)$$

where α is the internal variable that corresponds to the accumulated inelastic deformation. The yield function acts as a threshold condition to monitor the onset of inelastic deformation when the fiber stress $|\sigma_f^{\theta,B}|$ exceeds the yield capacity of the material. Subsequently, two possible outcomes exist for the computation of yield function:

$$f(\sigma_f^{\theta,B}) = \begin{cases} < 0 & \text{response is elastic} \\ = 0 & \text{inelastic response takes place} \end{cases}$$

When inelastic deformation takes place, the evolution of inelastic strain is governed by the following simple flow rule:

$$\left(\frac{\dot{\lambda}_{f,i}^{\theta}}{\lambda_{f,i}^{\theta}} \right) = \gamma \text{sign}(\sigma_f^{\theta,B}) \quad (5.10)$$

where γ is the consistency parameter for determining the inelastic flow rate and the hardening-like phenomenon, while $\text{sign}(\sigma_f^{\theta,B})$ returns +1 if $\sigma_f^{\theta,B}$ is positive and -1 if $\sigma_f^{\theta,B}$ is nega-

tive. Subsequently, the isotropic hardening law can be expressed as

$$\dot{\alpha} = \gamma \quad (5.11)$$

The evolution of inelastic flow follows the Kuhn-Tucker conditions, i.e.

$$\gamma \geq 0 \quad \text{and} \quad f(\sigma_f^{\theta,B}) \leq 0 \quad \text{and} \quad \gamma f(\sigma_f^{\theta,B}) = 0 \quad (5.12)$$

Subsequently, $\dot{f}(\sigma_f^{\theta,B}) = 0$ and the consistency parameter can be derived from the chain rule, where

$$\gamma = \frac{E_f}{E_f + H_f} \frac{\dot{\lambda}}{\lambda} \text{sign}(\sigma_f^{\theta,B}) \quad (5.13)$$

For more information on the algorithm of the elasto-plastic framework, the reader may refer to Simo and Hughes (2006). In summary, the computation of true fiber stress for branch B can be illustrated as below:

1. Assuming that the initial values of the variables $\lambda_{f,i}^{\theta}(t)$ and $\alpha(t)$ are known, an elastic trial stress is first computed at the instant step $t + dt$, where

$$\sigma_f^{\theta,B \text{ trial}}(t + dt) = E_f \ln \left(\frac{\lambda_f^{\theta}(t + dt)}{\lambda_{f,i}^{\theta}(t)} \right) \quad (5.14)$$

2. By having the elastic trial stress, the trial yield function can be computed as

$$f^{\text{trial}}(t + dt) = \left| \sigma_f^{\theta,B \text{ trial}}(t + dt) \right| - \left(\sigma_f^y + H_f \alpha(t) \right) \quad (5.15)$$

3. If $f^{\text{trial}}(t + dt) \leq 0$, the load step is elastic and $\sigma_f^{\theta,B}(t + dt) = \sigma_f^{\theta,B \text{ trial}}(t + dt)$.

Else if $f^{trial}(t + dt) > 0$, the load step involves inelasticity and the true stress value needs to be further corrected by the use of other variables.

4. In the case where inelasticity occurs, the consistency parameter can be computed from the equation below:

$$\Delta\gamma = \frac{\text{sign}\left(\sigma_f^{\theta,B\,trial}(t + dt)\right) E_f}{E_f + H_f} \left(\frac{\lambda_f^\theta(t + dt) - \lambda_f^\theta(t)}{\lambda_f^\theta(t + dt)} \right) \quad (5.16)$$

5. Finally, the true stress for the inelastic step can be computed by

$$\sigma_f^{\theta,B}(t + dt) = \sigma_f^{\theta,B\,trial}(t + dt) - E_f \ln \left(1 + \Delta\gamma \text{sign}\left(\sigma_f^{\theta,B\,trial}(t + dt)\right) \right) \quad (5.17)$$

6. The inelastic stretch and internal variable can be updated following the equations below:

$$\lambda_{f,i}^\theta(t + dt) = \lambda_{f,i}^\theta(t) \left(1 + \Delta\gamma \text{sign}\left(\sigma_f^{\theta,B\,trial}(t + dt)\right) \right) \quad (5.18)$$

$$\alpha(t + dt) = \alpha(t) + \Delta\gamma \quad (5.19)$$

Steps 1 to 6 are repeated for the computation of the true fiber stress in branch B at the subsequent load step ($t + dt$, $t + 2dt$, $t + 3dt$, and etc.). Finally, the total true fiber stress for any given fiber orientation θ is:

$$\sigma_f^\theta = K_f \lambda_f^\theta \left(\lambda_f^\theta - 1 \right)^a + E_f \ln \left(\frac{\lambda_f^\theta}{\lambda_{f,i}^\theta} \right) \quad (5.20)$$

and the first Piola-Kirchhoff stress tensor in Eq (3.12) becomes:

$$\mathbf{P} = \mathbf{F} \int_{-\pi/2}^{\pi/2} \Psi(\theta) \left(K_f \lambda_f^\theta (\lambda_f^\theta - 1)^a + E_f \ln \left(\frac{\lambda_f^\theta}{\lambda_{f,i}^\theta} \right) \right) \frac{\mathbf{N}^\theta \otimes \mathbf{N}^\theta}{\|\mathbf{FN}^\theta\|^2} d\theta \quad (5.21)$$

Table 5.1 summarizes the material parameters to be determined from the experimental data.

Table 5.1: Summary of the material parameters at fiber scale.

Model component	Parameter
Branch A (Elastic component)	K_f a
Branch B (Elasto-plastic component)	E_f σ_f^y H_f

Remark 15. *The elasto-plastic framework adopted in the present study encompasses more general dissipative phenomena than the classical plastic deformations commonly observed in metals beyond yield stress. Indeed, as previously emphasized, this framework is used in order to phenomenologically describe the irreversible inter-fiber interactions in the materials.*

Remark 16. *For simplicity, linear hardening is considered in the development of the constitutive model (in the elasto-plastic component) despite the non-linear hardening response observed from the experimental results (Figure 4.10).*

5.3 Special case of uniaxial extension of 2D membrane

The stress analysis in this work is simplified to two-dimensional (2D) state due to the extremely thin structures of the electrospun nanofibrous membranes, where the stress component in the third direction (thickness direction) is considered as negligible. Subsequently,

there is no imposed constraint on the compressibility of the electrospun nanofibrous structures.

In the following, we focus our attention on the special case of uniaxial extension. Recall that the material is assumed to be homogenous and continuous in the macroscopic scale. By assuming only the in-plane variation of the fiber orientation, the unit vector \mathbf{N}^θ characterizing the initial orientation of the fibers is expressed as

$$\mathbf{N}^\theta = \cos \theta \mathbf{e}_1 + \sin \theta \mathbf{e}_2 \quad (5.22)$$

which is only a function of θ . Under uniaxial extension, the two-dimensional form of the deformation gradient tensor \mathbf{F} is

$$\mathbf{F} = \lambda \mathbf{e}_1 \otimes \mathbf{e}_1 + \lambda^{-k} \mathbf{e}_2 \otimes \mathbf{e}_2 \quad (5.23)$$

where λ is the ratio between the current and initial lengths of the membrane and k is the in-plane Poisson's ratio for the case of uniaxial extension. The tensor product $\mathbf{N}^\theta \otimes \mathbf{N}^\theta$ is

$$\mathbf{N}^\theta \otimes \mathbf{N}^\theta = \cos^2 \theta \mathbf{e}_1 \otimes \mathbf{e}_1 + \sin^2 \theta \mathbf{e}_2 \otimes \mathbf{e}_2 + \cos \theta \sin \theta (\mathbf{e}_1 \otimes \mathbf{e}_2 + \mathbf{e}_2 \otimes \mathbf{e}_1) \quad (5.24)$$

and the fiber stretch is given by

$$\lambda_f^\theta = \|\mathbf{F}\mathbf{N}^\theta\| = \sqrt{\lambda^2 \cos^2 \theta + \lambda^{-2k} \sin^2 \theta} \quad (5.25)$$

By substituting all the relevant components into Equation (3.12), the first Piola-Kirchhoff stress along the tensile direction is

$$P_{11} = \int_{-\pi/2}^{\pi/2} \Psi(\theta) \sigma_f^\theta \left(\frac{\lambda \cos^2 \theta}{\lambda^2 \cos^2 \theta + \lambda^{-2k} \sin^2 \theta} \right) d\theta \quad (5.26)$$

which is equivalent with

$$P_{11} = \frac{F}{A_o} \quad (5.27)$$

provided that the axial force F and the initial cross section A_o of the material (membrane) are known. It is to note that the in-plane Poisson's ratio k is treated as one of the material parameters and is determined through the fitting of experimental data with model in the later section. Finally, under uniaxial tensile loading, the orientation index in Equation (3.13) reduces to

$$\beta = \int_{-\pi/2}^{\pi/2} \Psi(\theta) \left(\frac{\lambda \cos \theta}{\sqrt{\lambda^2 \cos^2 \theta + \lambda^{-2k} \sin^2 \theta}} \right) d\theta \quad (5.28)$$

Generally, the proposed model is adopted for the computation of fiber scale and macroscopic scale responses, by utilizing the software MATLAB. The overview for the simulation of the behavior on the fiber scale and macroscopic scale is depicted in Figure 5.2.

5.4 Parametric studies

A total of five material parameters (K_f , a , E_f , σ_f^y and H_f) are employed at the fiber scale for the description of fiber response, while one parameter (k) is adopted for the determination of membrane response for the special case of uniaxial extension, in a phenomenological way. Each material parameter has a different physical significance and plays an important role in determining the final outcome of the model. Subsequently, two parameters attribute to the non-linear elastic response (Branch A) while three other parameters for the elasto-plastic response (Branch B) of the material. Subsequently, the influence of each material parameter is investigated by the simulation of stress-stretch response at fiber scale, by changing the value of the particular parameter and keeping all other values constant. Recall that the present work focuses on the mechanical response of randomly oriented electrospun nanofibrous membranes, where fibers are randomly deposited in all possible

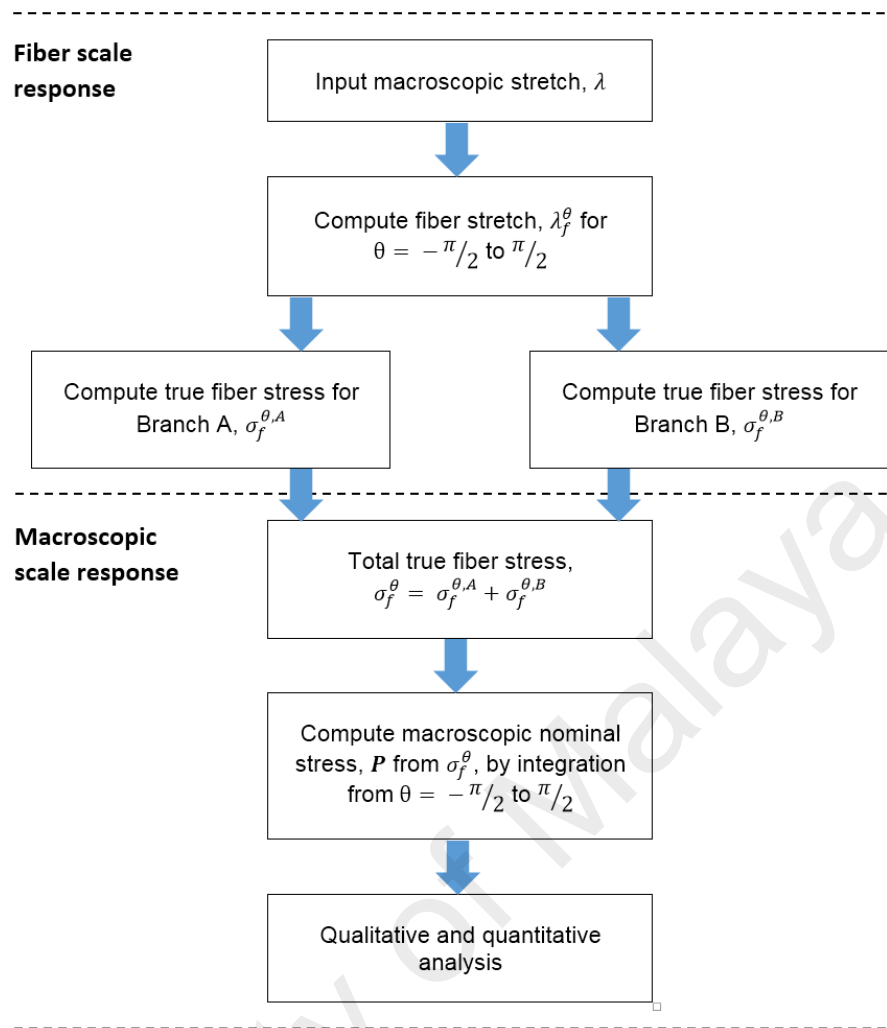


Figure 5.2: Overview for the computation of mechanical response by using MATLAB software.

directions ($\theta = -\pi/2$ to $\theta = \pi/2$). Therefore, fibers from different orientations respond differently towards the applied macroscopic deformation. In this section, simulations are conducted by assuming a constant fiber orientation of 0° (direction of applied uniaxial deformation) for all the cases. Constant values of the material parameters as shown in Table 5.2 are adopted for the simulation, except for the parameter to be investigated in the particular case. Meanwhile, the effect of fiber orientation will be investigated in the following section.

5.4.1 Elasticity (Branch A)

Branch A consists of a nonlinear spring that represents the behavior of an individual fiber. Two material parameters are adopted, with K_f represents the stiffness of a single fiber

Table 5.2: Values of material parameters used for simulation.

Parameter	Value
K_f	7.0 (MPa)
a	0.8
E_f	70.0 (MPa)
σ_f^y	1.0 (MPa)
H_f	2.5 (MPa)
k	0.2

while a serves as the shape control constant for the stress-stretch relationship. In order to determine the significance of each material parameter, macroscopic uniaxial cyclic loading is simulated for one cycle, from $\lambda = 1$ to $\lambda = 1.05$ for uploading and the reverse for unloading, as shown in Figure 5.3. Meanwhile, arbitrarily values are set for the interest parameter while keeping all other values constant. It is important to note that λ is the macroscopic stretch while λ_f is the stretch at fiber scale. In the present work, the relationship of λ_f to λ is linked by the affine motion assumption as presented in Section 3.3.2. For the special case of uniaxial extension of 2D membrane, the relationship of λ_f to λ is further formulated as stated in Equation (5.25). Consequently, at $\theta = 0^\circ$, $\lambda_f = \lambda$ and the deformation of $\lambda = 1$ to $\lambda = 1.05$ corresponds to $\lambda_f = 1$ to $\lambda_f = 1.05$ in this case. Subsequently, the simulation is conducted for two different cases, by manipulating (1) K_f and (2) a , and the resulting fiber stress-stretch curves are depicted in Figure 5.4.

Figure 5.4 (a) and 5.4 (b) are simulated by adopting different values of K_f and a respectively. It was observed that increasing the value of K_f increases the stiffness of the fiber and thus reflected by a greater slope of the stress-stretch curve. Meanwhile, altering the value of a produces slightly different shape of the stress-stretch curves which can be seen by increasing the value of a . Moreover, a smaller value of a gives rise to a higher stress level as can be seen in Figure 5.4 (b). Due to the absence of irreversible deformation, the curves in Figure 5.4 possess similar paths for both loading and unloading and no

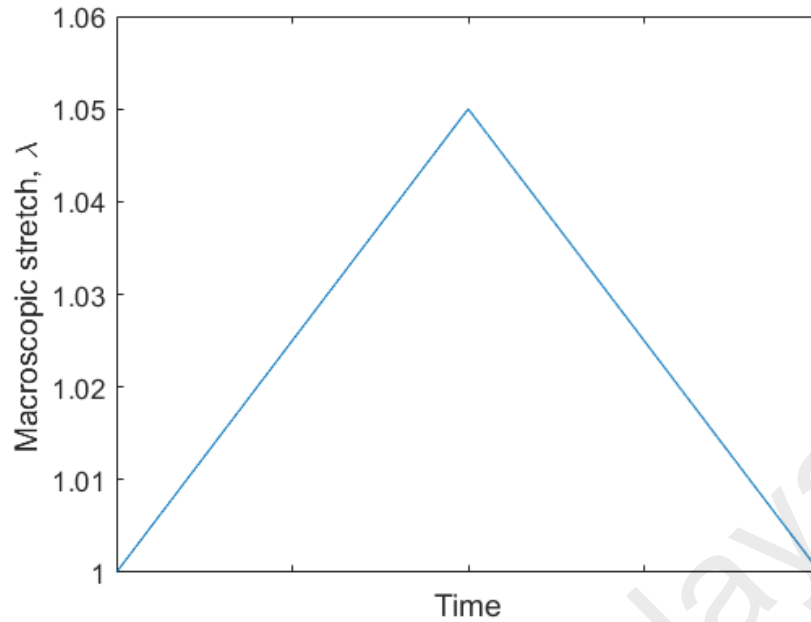


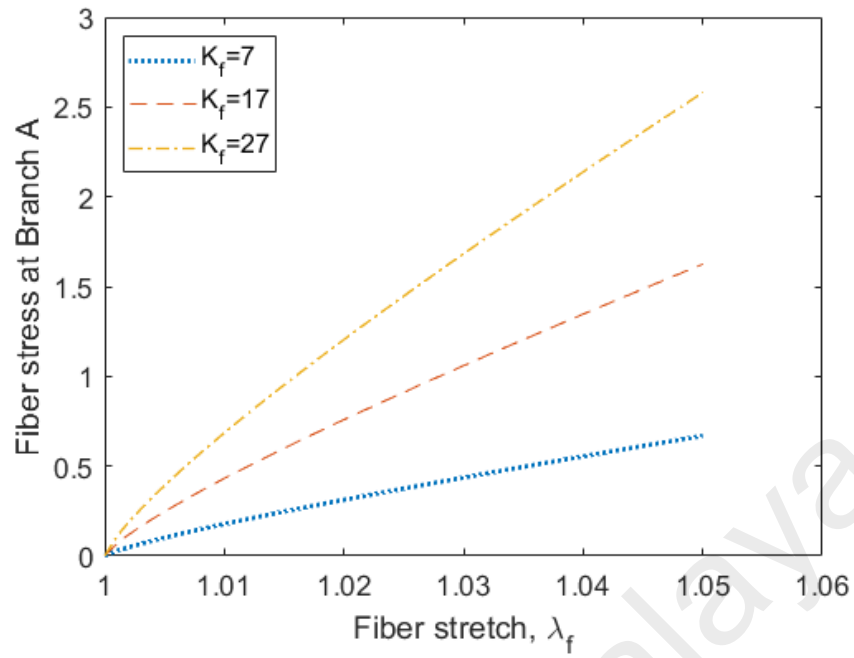
Figure 5.3: Loading profile for the simulation of one cycle, from $\lambda = 1$ to $\lambda = 1.05$.

hysteresis is observed in this case.

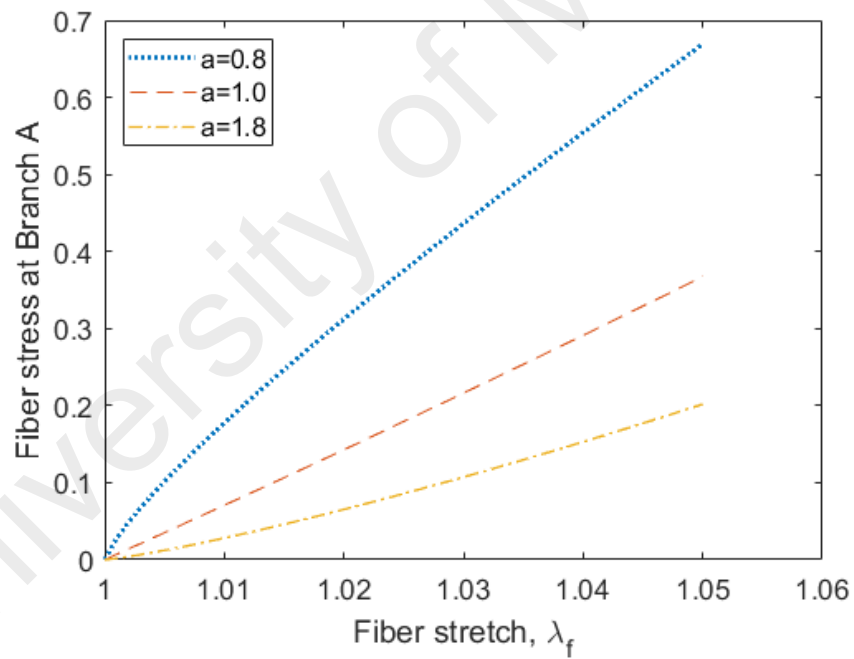
5.4.2 Elasto-plasticity (Branch B)

Branch B consists of a linear spring connected in series with a skidding block and another linear spring in parallel, representing the elasto-plastic behavior of the material. In this case, isotropic, linear hardening is adopted for the inelastic behavior. Subsequently, three material parameters are employed for the elasto-plastic component. Recalling that E_f is the material parameter for the first linear spring (see Figure 5.1), H_f as the parameter akin to hardening modulus in classical plasticity theory and σ_f^y as the initial threshold stress of inelastic deformation. Similar loading conditions as in the previous section are simulated for three different cases, by manipulating (1) E_f , (2) σ_f^y and (3) H_f , and the resulting fiber stress-stretch curves are illustrated in Figure 5.5.

Figure 5.5 (a), 5.5 (b) and 5.5 (c) are simulated by adopting different values of E_f , σ_f^y and H_f respectively. It is observed that by increasing the values of E_f , the slope of the first linear part increases in both uploading and unloading of the cycle (Figure 5.5 (a)). Subsequently, increasing the value of σ_f^y promotes a higher initial threshold stress for the



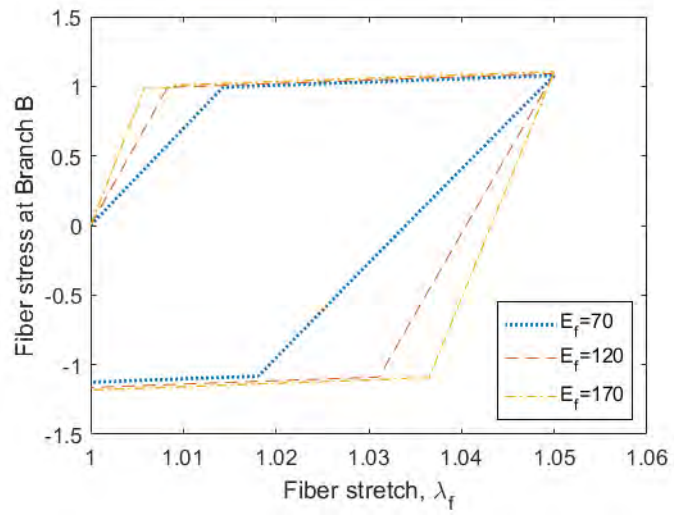
(a)



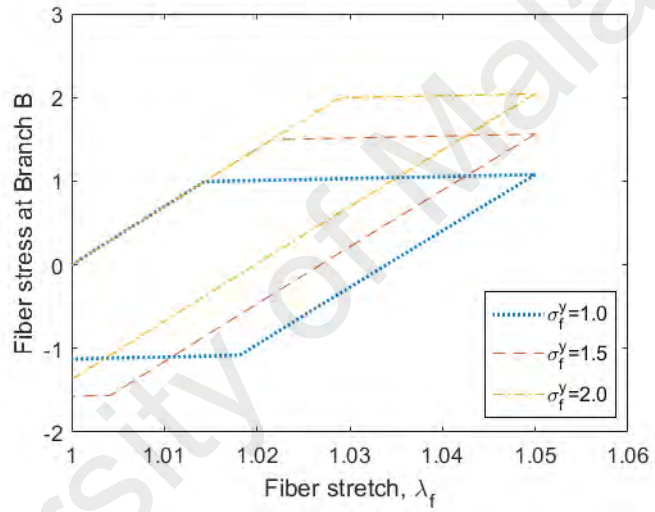
(b)

Figure 5.4: Influence of the material parameters (a) K_f and (b) a on fiber stress at branch A.

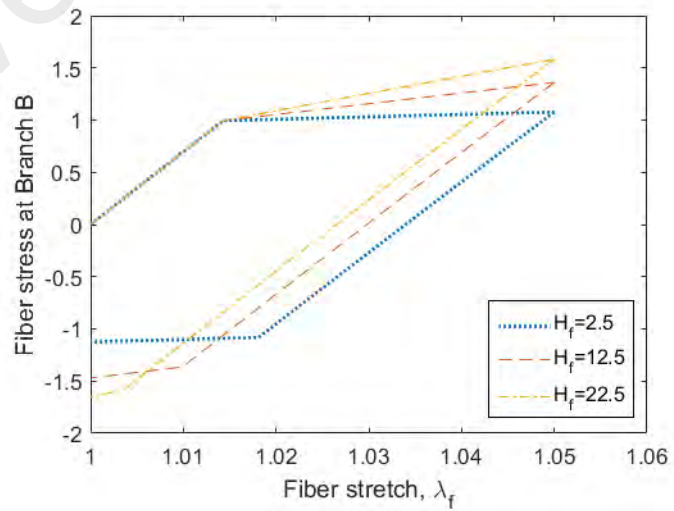
initiation of inelastic deformation (the point of sudden sharp change of the stress level), and thus material starts to deform only at higher stress level for a higher value of σ_f^y (Figure 5.5 (b)). Lastly, increasing the values of H_f increases the gradient of the second linear part, as illustrated in Figure 5.5 (c).



(a)



(b)



(c)

Figure 5.5: Influence of the material parameters (a) E_f , (b) σ_f^y and (c) H_f on fiber stress at branch B.

5.4.3 Macroscopic parameter, k

Recall that in the present work, the focus is put on the uniaxial extension of 2D membrane (as explained in Section 5.3). The relationship between stretches in two perpendicular directions, i.e. axial and transverse directions is represented by the parameter k , which is determined through the fitting of experimental data with the proposed model. Since k is a macroscopic parameter, simulation was conducted at the macroscopic scale by manipulating the value of parameter k and keeping the values of all other parameters constant, in order to observe the effect of k on the mechanical response of the material. For this purpose, cyclic loading test with increasing maximum strain (as conducted in Section 3.2.3.3) is simulated by adopting the macroscopic stretch values from experimental data. Subsequently, the result obtained is depicted in Figure 5.6.

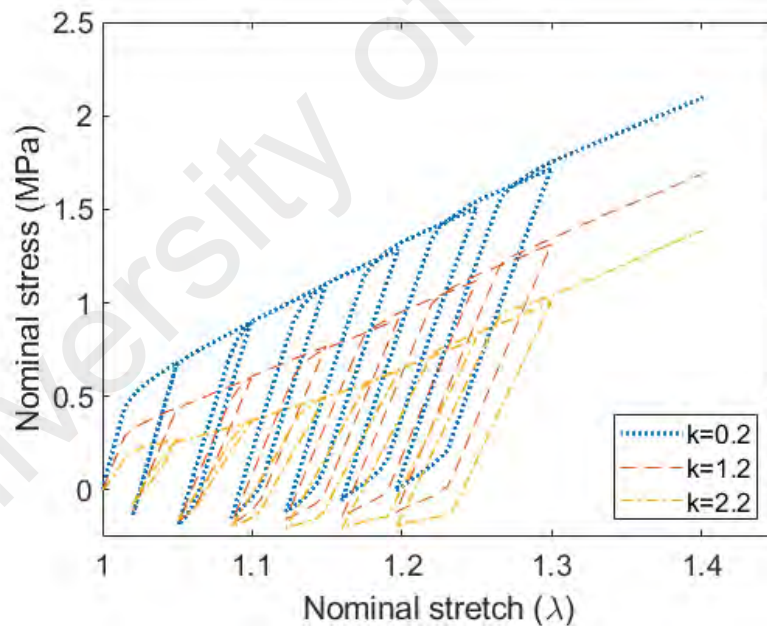


Figure 5.6: Influence of material parameter k .

From Figure 5.6, it is observed that stress level decreases as the value of k increases. Increasing the value of k signifies that the lateral contraction (λ_2) is greater corresponds to the axial elongation (λ_1). Generally, increasing the value of k does not modify the general stress response where characteristics such as hysteresis and inelastic deformation are still

preserved. However, the sizes of the last three hysteresis loop increase with increasing the value of k . Furthermore, negative stress level is observed at some parts of the curves. This is because unlike experimental test where specimens were unloaded to zero force, simulation is purely controlled by macroscopic stretch values obtained from experimental data, and there is no constraint on the minimum force for each unloading path.

5.5 Influence of fiber orientation

As mentioned earlier, the fiber scale response for randomly oriented nanofibrous membrane is different in each orientation and is highly dependent on the direction of the macroscopic material deformation. In order to investigate the influence of fiber orientation on the mechanical response of the single fiber, uniaxial cyclic loading of one cycle (similar as in Sections 5.4.1 and 5.4.2) is simulated from $\lambda = 1$ to $\lambda = 1.05$ for uploading and the reverse for unloading (see Figure 5.3), for seven different fiber orientation, i.e. 0° , 15° , 30° , 45° , 60° , 75° and 90° with respect to the loading axis, utilizing constant values of material parameters as shown in Table 5.2. The plot of fiber stretch, λ_f as a function of macroscopic stretch, λ is presented in Figure 5.7, for all seven orientations of fiber. Subsequently, the simulated fiber stress-stretch curves for nonlinear elastic component (Branch A) and elastoplastic component (Branch B) are shown in Figure 5.8 and Figure 5.9 respectively.

Recall that the fiber stretch defined in Equation (3.6) is a function of unit vector \mathbf{N} which depends on the fiber orientation θ . Therefore, material responses differently in each orientation when deformation is applied globally, due to the different λ_f developed in each orientation. From Figure 5.7, it is observed that fibers in the orientations of 0° to 60° experience tension while those in 75° and 90° orientations experience compression when similar deformation is applied at the macroscopic scale. Subsequently, this gives rise to different stress-stretch response in the microscopic scale. It is crucial to understand this phenomenon since it is one important characteristic of randomly oriented electrospun nanofibrous mem-

brane that determines the global mechanical response of the material.

For the nonlinear elastic component (Branch A), the fiber stress-stretch curves of all seven orientations show different stress responses as plotted in Figure 5.8. This is due to the reason that the fibers in different orientation experience different degrees of stretching with respect to the loading axis (0°). Here, fibers from 0° experience the same amount of stretch that is applied globally and thus having the highest level of stress and stretch. Subsequently, the stress-level decreases with increasing degree of orientation since fibers are further away from the direction of applied macroscopic deformation. Since Branch A considers only the elastic behavior of the fiber, loading and unloading follow similar paths as in Section 5.4.

Meanwhile for the elasto-plastic component (Branch B), different responses are observed on the seven different orientations as shown in Figure 5.9. From Figure 5.9, simulation shows that fibers from 0° to 45° orientations experience inelastic deformation while fibers in the 60° to 90° orientations remain in the elastic region of the stress-stretch curves. Here, yield stress is exceeded for the cases of 0° to 45° orientations as shown by the sharp change of the stress-stretch curves and hysteresis observed. On the other hand, fibers in the 60° orientation remain elastic in tension while fibers in 75° and 90° orientations remain elastic in compression.

5.6 Influence of number of integration points

Cyclic loading with increasing maximum strain as conducted in the experimental work is simulated using the proposed model. Recalling Equation (3.7), the simulation of the macroscopic response requires the numerical integration over the unit element to obtain the stress response of the material. According to Verron (2015), the determination of a relevant number of integration points is crucial for the evaluation of the constitutive equation. In this section, the minimum number of integration points required to produce a smooth stress-stretch relationship will be discussed.

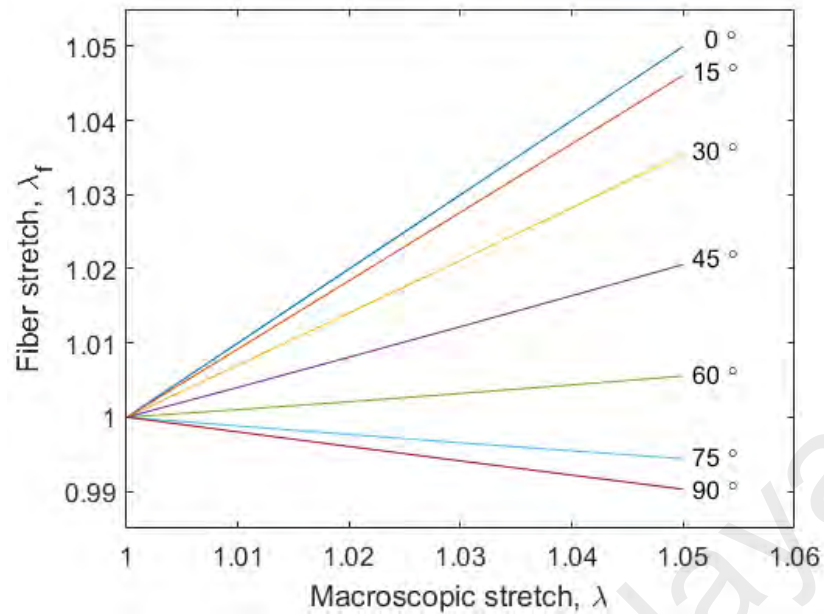


Figure 5.7: Fiber stretch, λ_f as a function of macroscopic stretch, λ for seven fiber orientations, i.e. 0° , 15° , 30° , 45° , 60° , 75° and 90° .

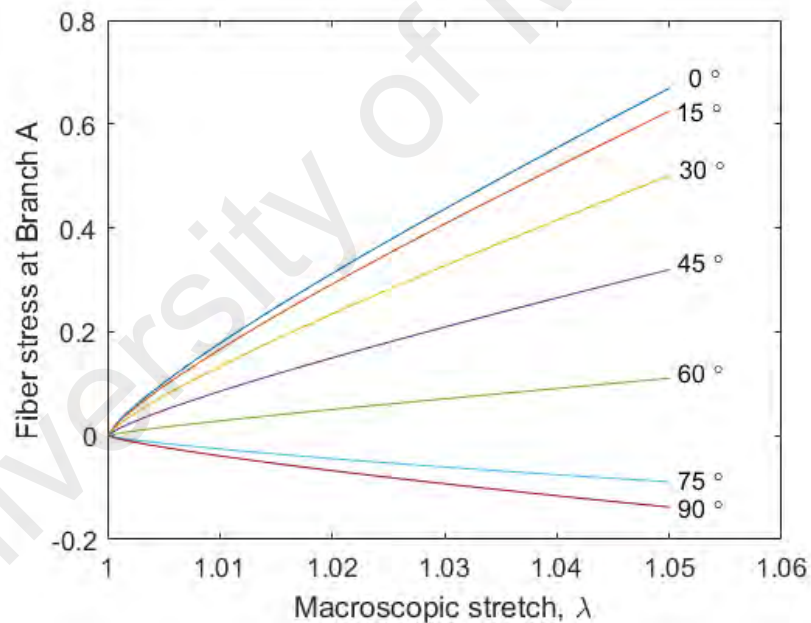


Figure 5.8: Micromechanical response in different orientations for the elastic behavior (Branch A).

Similar to Section 5.4.3, simulation is conducted by adopting the macroscopic stretch values from experimental data. Subsequently, constant material parameters as shown in Table 5.2 are employed and different numbers of integration points are assigned for the simulation. The simulation is initiated with 5 integration points, and increase to 10, 20, 50 etc. The stress-stretch curves produce from different numbers of integration points are

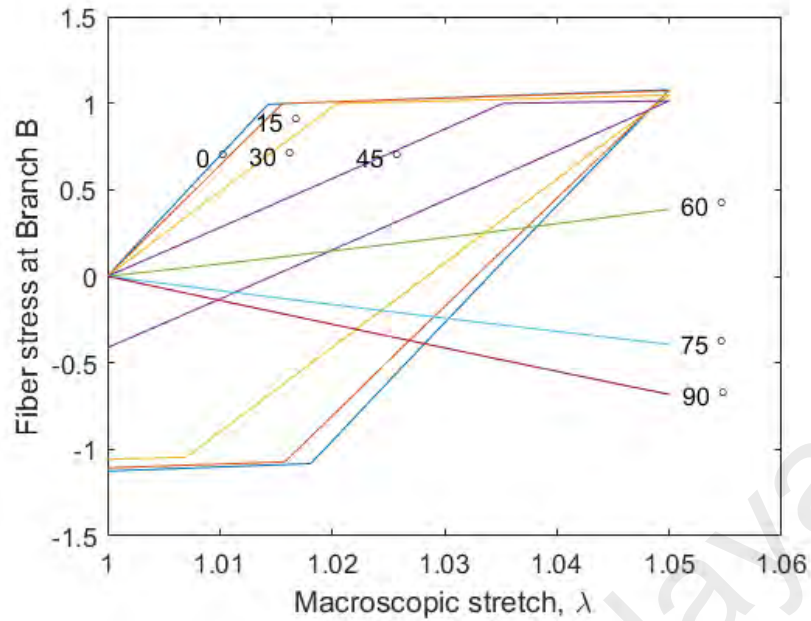


Figure 5.9: Micromechanical response in different orientations for the inelastic behavior (Branch B).

shown in Figure 5.10.

Generally, it is observed that the stress-stretch curve in Figure 5.10 (a) is non-smooth due to the insufficient integration points for the computation. Increasing the number of integration points to 10 produces a smoother stress-stretch curve as depicted in Figure 5.10 (b). Further increasing to 20 points produces a better, smoother curve that is sufficient to represent the macroscopic stress-stretch response (Figure 5.10 (c)). Finally, 50 integration points produce a sufficient smooth stress-stretch curve (Figure 5.10 (d)) that is similar to the curve computed with 20 integration points.

5.7 Identification of material parameters

The constitutive model developed in this work is implemented in MATLAB in order to identify the material parameters through the fitting of the proposed model with experimental data. Subsequently, a nonlinear constrained optimization technique with the `fmincon` solver is adopted for the identification purpose. Generally, the proposed constitutive model exhibits six material parameters, i.e. five parameters for fiber scale response (K_f , a , E_f , σ_f^y and H_f) and one parameter for the special case of uniaxial extension (k).

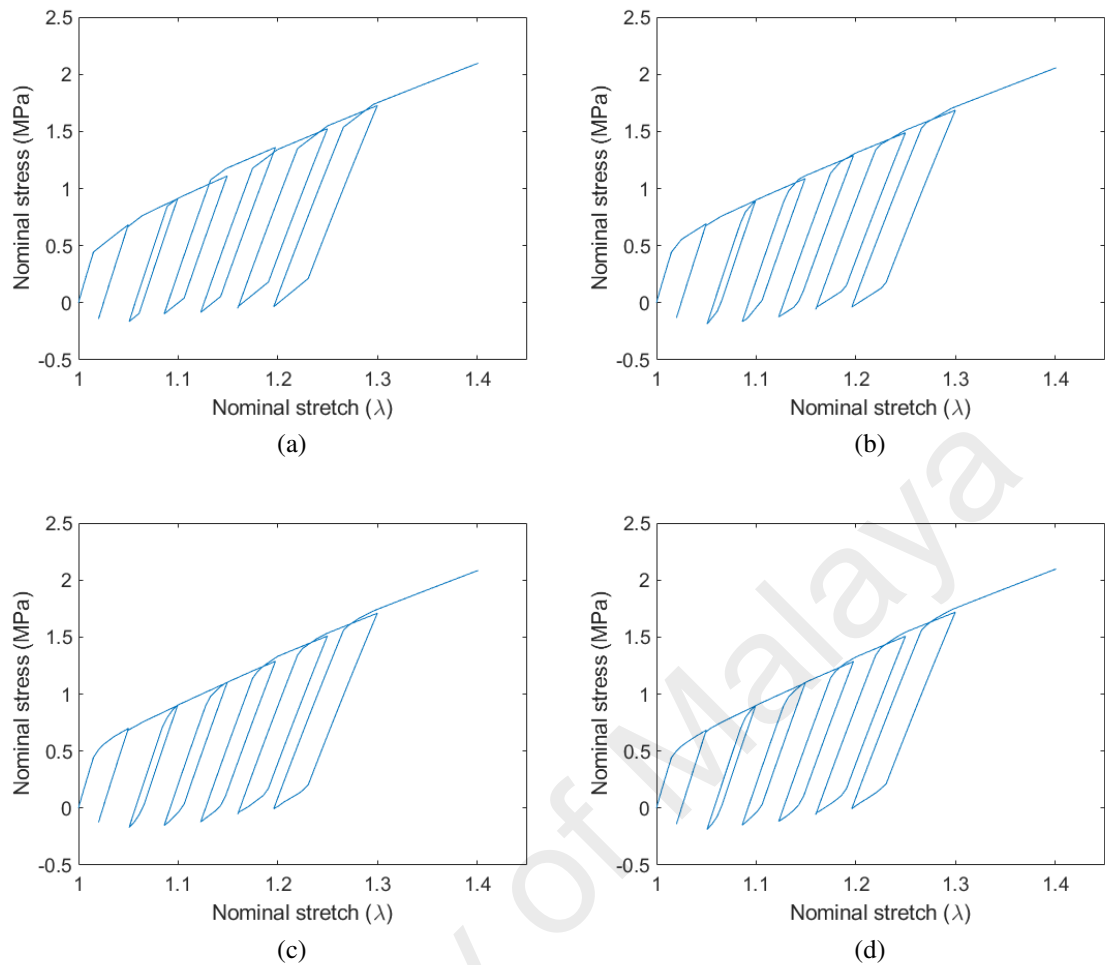


Figure 5.10: Influence of number of integration points on the macroscopic stress-stretch curve: (a) 5 points, (b) 10 points, (c) 20 points and (d) 50 points.

In this section, the proposed continuum model is fitted to the experimental data obtained from the uniaxial cyclic loading test of randomly oriented PVDF nanofibrous membrane, by assuming that the material is isotropic in-plane in the reference configuration. It was found that the material exhibits strong inelastic responses characterized by hysteresis and inelastic strain observed during the loading-unloading-reloading path. The obtained parameters are presented in Table 5.3 while the comparison between model and experiment is given in Figure 5.11.

Evaluating Figure 5.11, it is found that the proposed model is capable to describe qualitatively well the general stress-strain response of the material, despite a slight under-

Table 5.3: Material parameters involved in the computation of macroscopic stress-stretch response of randomly oriented electrospun PVDF nanofibrous membrane.

Parameter	Value
K_f	7.2373 (MPa)
a	0.8369
E_f	70.1568 (MPa)
σ_f^y	1.0666 (MPa)
H_f	2.4574 (MPa)
k	0.1979

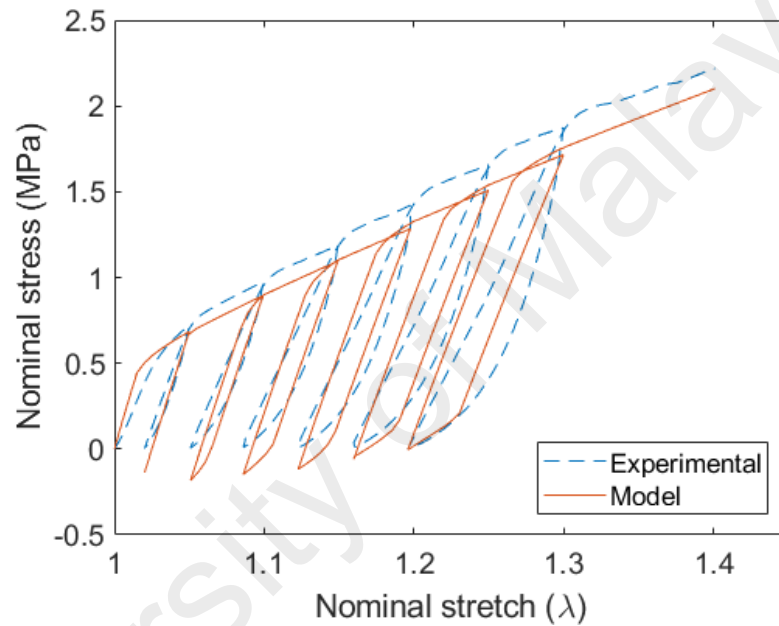


Figure 5.11: Comparison of model prediction with experimental results of cyclic loading test with increasing maximum strain.

estimation on the overall stress-stretch curve. Indeed, both hysteresis and inelastic strains are generally well captured by the model. Moreover, the model shows that the size of the hysteresis increases whenever the inelastic deformation increases. Similar to Section 5.4.3, recall that the macroscopic stress-stretch response is purely simulated by imposing the macroscopic stretch values obtained from experimental data. Furthermore, there is no constraint on the minimum force for each unloading path, resulting in the negative stress values as observed in Figure 5.11.

With these fitted values of material parameters, the model is subsequently used to simulate the material response under uniaxial monotonic loading. The model response is

compared with the related experimental curve (Figure 4.5), as illustrated in Figure 5.12. It is observed that the model is capable to reproduce qualitatively the monotonic experimental results. Despite the small discrepancy at the initial slope, the model appears to capture well the general fundamental response of the material.

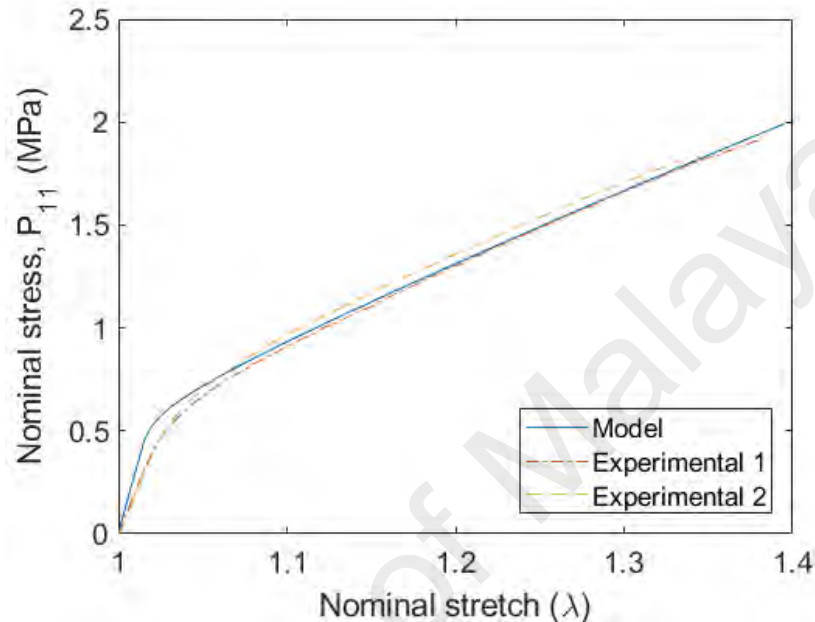


Figure 5.12: Comparison of model prediction with experimental results of uniaxial monotonic loading test.

From the cyclic loading curve with increasing maximum stretch simulated in Figure 5.11 (model prediction), Young's modulus of the simulated curve can be computed by measuring the slope of each uploading paths, similar to the experimental practice in Section 4.3.2. Subsequently, the Young's modulus ratio can be defined by the ratio between the Young's modulus for a given cycle (given maximum strain) with that of the first cycle. The values of the Young's modulus and the Young's modulus ratio for the simulated curve are tabulated in Table 5.4, corresponding to the maximum strain of each cycle.

The computation of the Young's modulus ratio from model prediction allows further comparison on the evolution of Young's modulus ratio between experimental and the proposed model. For this purpose, the evolution of Young's modulus ratio of the simulated

Table 5.4: Young's modulus and Young's modulus ratio of simulated cyclic loading curve corresponded to the maximum strains.

Maximum strain, ϵ_{max} (%)	Young's modulus, E (MPa)	Young's modulus ratio, E_i/E_o
0	30.0	1.000
5	26.7	0.890
10	25.0	0.833
15	25.0	0.833
20	24.0	0.800
25	23.3	0.777
30	22.5	0.750

curve is plotted together with the values from experiment (Figure 4.8) as a function maximum nominal strain, as illustrated in Figure 5.13.

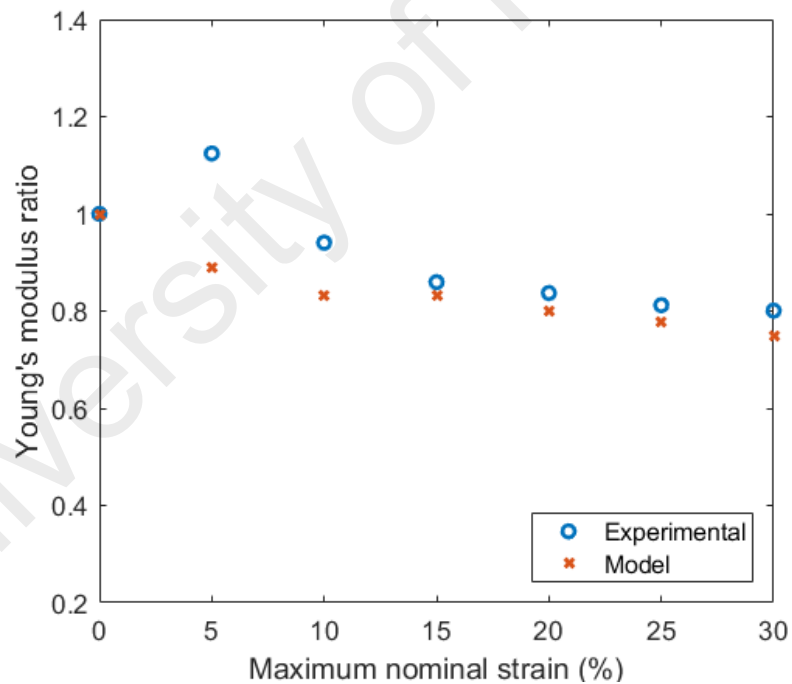


Figure 5.13: Comparison of model prediction with experimental results of Young's modulus ratio.

From Table 5.4, it is observed that the proposed model predicted slightly higher values of the Young's modulus as compared to that from the experiment (Table 4.4). Whereas from Figure 5.13, unlike the phenomenon observed from experimental data, Young's modulus from model prediction does not show increment from the first to second point. Instead,

a gradual decrement of Young's modulus is observed. Thus, the model predicted that the stiffness of electrospun PVDF nanofibrous membranes decreases with increasing maximum strain. Even though the proposed model failed to predict the initial increment on the evolution of Young's modulus ratio, the trend of decrement of Young's modulus from second point onwards is reproduced well by the model.

In addition to the mechanical responses presented in Figures 5.11, 5.12 and 5.13, comparison can also be conducted on the fiber orientation along the tensile direction between experimental and model by employing the orientation tensor A_{11} determined experimentally in Section 3.2.5 with the simulation of the orientation index, β in Equation (5.28). In order to be able to use the data of A_{11} , the orientation index β in Equation (5.28) should be converted into A_{11} . Recall the general equation of orientation index β (Equation (3.13)), by applying simple vector algebra, Equation (3.13) can be rewritten as:

$$\beta = \int_{-\pi/2}^{\pi/2} \Psi(\theta) \cos \theta \, d\theta \quad (5.29)$$

Subsequently, the orientation index β can be simply related to A_{11} (Equation (3.4)) via

$$A_{11} = \beta \int_{-\pi/2}^{\pi/2} \cos^2 \theta \, d\theta \quad (5.30)$$

Finally, a simulation is conducted using Equation (5.30) and the comparison between model and experimental A_{11} is given in Figure 5.14.

From Figure 5.14, it is observed that the rate of the deformation-induced fiber re-orientation is higher in the experimental data in comparison with the prediction of model. This observation signifies that in reality, fibers re-oriented more rapidly towards the direction of applied macroscopic deformation than that assumed by the affine motion assumption. Even though the affine motion assumption might not truly represent the fiber response

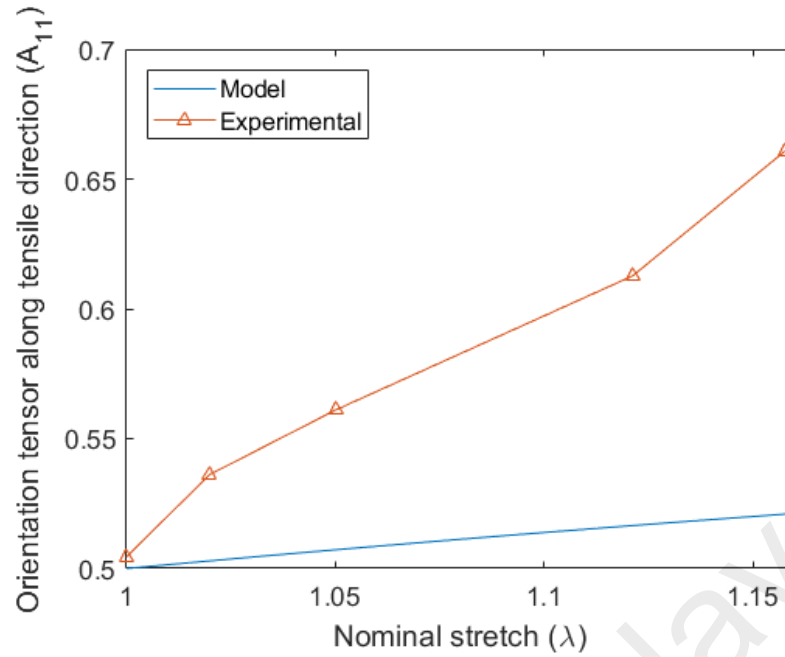


Figure 5.14: Comparison of model prediction with experimental result of fiber orientation tensor along tensile direction, A_{11} .

towards macroscopic deformation, this assumption is utilized for simplicity in accordance with one of the objective of the present work, i.e. to proposed a simple phenomenological model.

5.8 Simulation of other deformation modes

In order to further explore the predictive capability of the model, simulations are conducted for other deformation modes, i.e. biaxial stress states, by using the values of the material parameters tabulated in Table 5.3. In this case, the deformation gradient tensor has the form:

$$\mathbf{F} = \lambda \mathbf{e}_1 \otimes \mathbf{e}_1 + \lambda^B \mathbf{e}_2 \otimes \mathbf{e}_2 \quad (5.31)$$

where B is the biaxiality constant having the following values (Andriyana, 2006):

$$B = \begin{cases} -0.2 & \text{for uniaxial extension} \\ 0 & \text{for pure shear (planar extension)} \\ 1 & \text{for equibiaxial extension} \end{cases}$$

In the following, the model response under equibiaxial extension and pure shear is first presented. Subsequently, the effect of biaxiality on the fiber re-orientation is investigated.

5.8.1 Equibiaxial extension

The governing equations needed for the simulation of equibiaxial loadings are summarized as below:

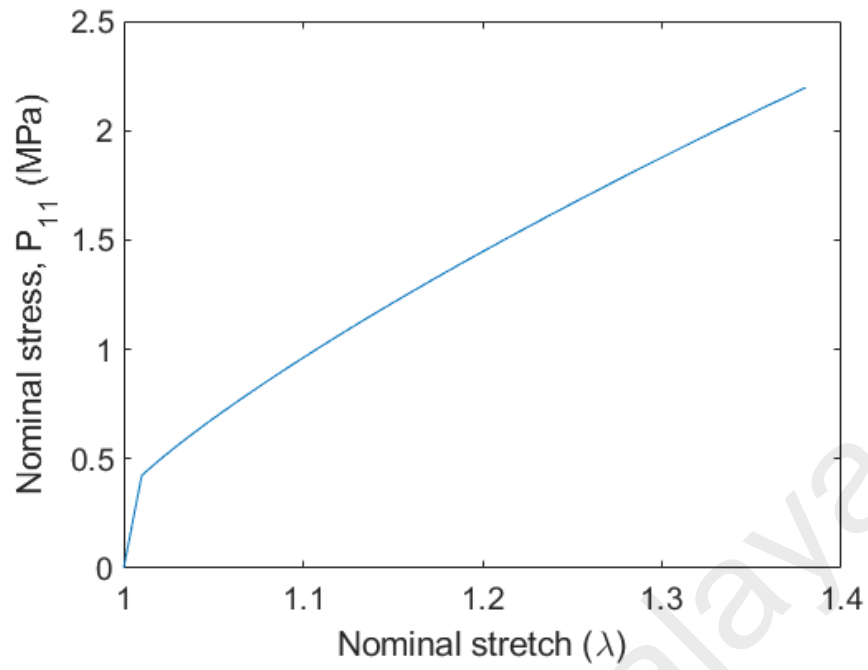
$$\lambda_f^\theta = \|\mathbf{FN}^\theta\| = \lambda \quad (5.32)$$

$$P_{11} = P_{22} = \int_{-\pi/2}^{\pi/2} \Psi(\theta) \sigma_f^\theta \frac{\cos^2 \theta}{\lambda} d\theta \quad (5.33)$$

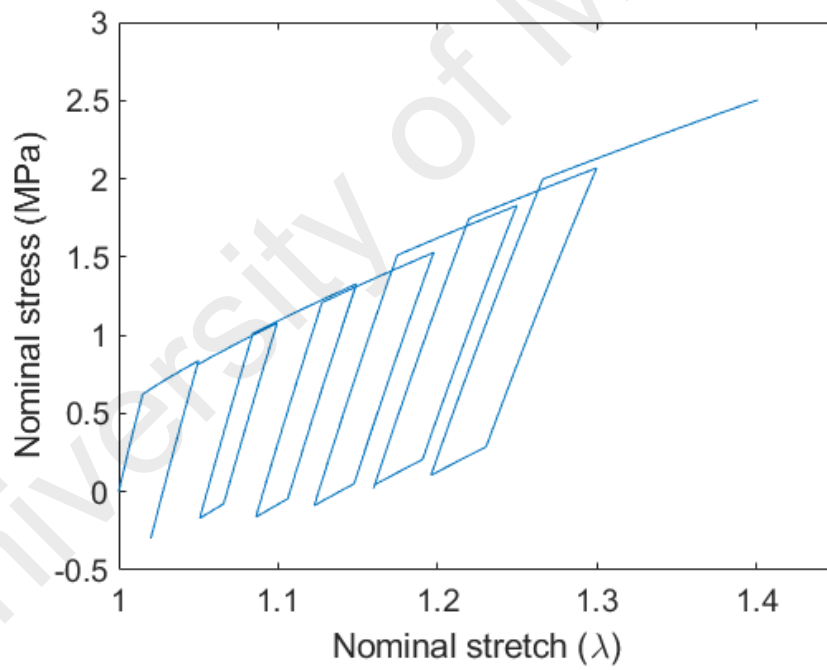
$$\beta = \int_{-\pi/2}^{\pi/2} \Psi(\theta) \cos \theta d\theta \quad (5.34)$$

Utilizing equation (5.33), monotonic and cyclic loading with increasing maximum strain are simulated, and the model behaviors are illustrated in Figures 5.15 (a) and 5.15 (b).

From Figure 5.15, the monotonic and cyclic loading conditions under equibiaxial extension is simulated with elastic and inelastic responses. Generally, higher stress level is observed from the macroscopic stress-stretch curves under equibiaxial extension, as compared to the case of uniaxial extension. From Figure 5.15 (b), hysteresis starts to form from the second cycle and the size of the hysteresis becomes larger as the imposed maximum stretch increases. Furthermore, it is observed that the inelastic stretch increases as the nominal stretch increases.



(a)



(b)

Figure 5.15: Simulation of (a) monotonic and (b) cyclic loading with increasing maximum stretch for equibiaxial extension.

5.8.2 Pure shear

The governing equations needed for the simulation of pure shear are summarized as below:

$$\lambda_f^\theta = \|\mathbf{FN}^\theta\| = \sqrt{\lambda^2 \cos^2 \theta + \sin^2 \theta} \quad (5.35)$$

$$P_{11} = \int_{-\pi/2}^{\pi/2} \Psi(\theta) \sigma_f^\theta \left(\frac{\lambda \cos^2 \theta}{\lambda^2 \cos^2 \theta + \sin^2 \theta} \right) d\theta \quad (5.36)$$

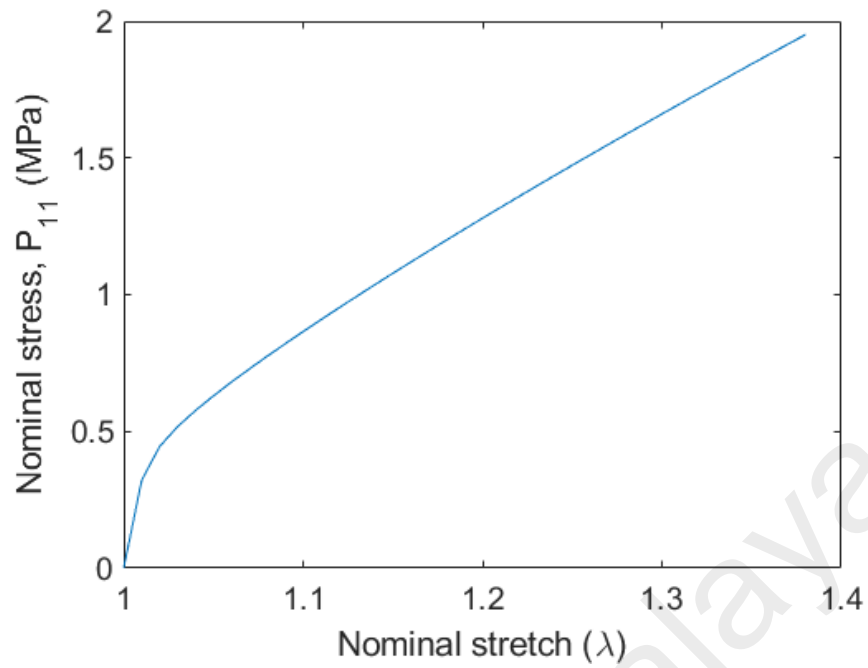
$$\beta = \int_{-\pi/2}^{\pi/2} \Psi(\theta) \left(\frac{\lambda \cos \theta}{\sqrt{\lambda^2 \cos^2 \theta + \sin^2 \theta}} \right) d\theta \quad (5.37)$$

Similarly, monotonic and cyclic loadings with increasing maximum stretch are simulated for pure shear (planar extension) utilizing Equation (5.36), and the resulting stress-stretch curves are depicted in Figure 5.16. It is observed that the macroscopic stress level of pure shear is lower than that of equibiaxial extension, but higher as compared to the curves of uniaxial extension. From Figure 5.16 (b), hysteresis starts to form from the second cycle. Similarly to Section 5.8.1, the size of hysteresis becomes larger as the maximum stretch increases. Meanwhile, the inelastic stretch increases as cyclic loading progresses.

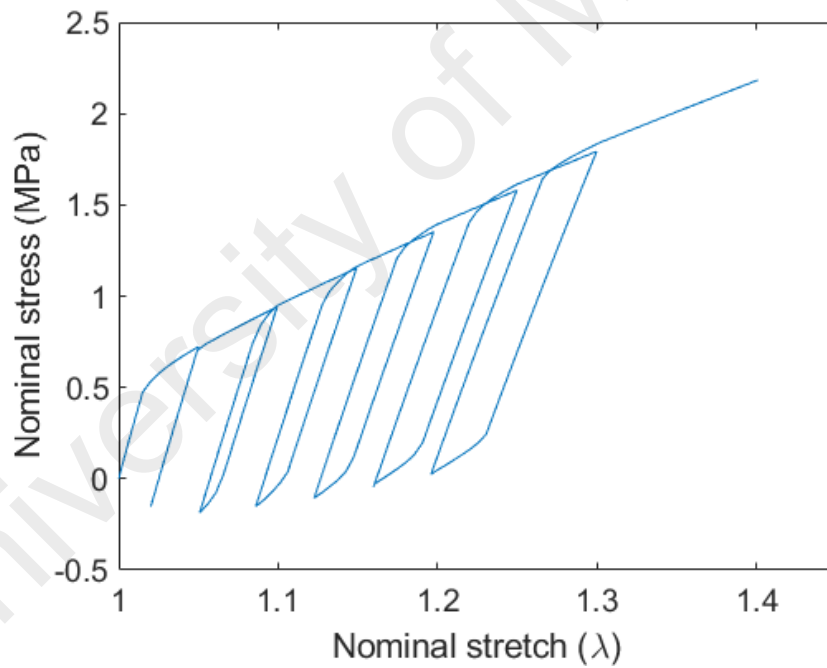
5.8.3 Effect of biaxiality

The effect of biaxiality on the degree of fiber re-orientation is investigated at three different global stretch values, i.e. $\lambda = 1.1$, $\lambda = 1.2$ and $\lambda = 1.3$, utilizing Equation (5.28), (5.34) and (5.37). Note that the simulation is conducted by assuming that the material is initially isotropic in the plane, where $\beta = 2/\pi$ (Ridruejo et al., 2012). Subsequently, the orientation index β is plotted against the biaxiality constant B , as illustrated in Figure 5.17 (a). Meanwhile, the degrees of fiber re-orientation in three different deformation modes are also investigated, as indicated in Figure 5.17 (b).

Remark 17. *It is to note that both the orientation index β and the component A_{11} of the orientation tensor can be used to represent the deformation-induced fiber re-orientation (in different magnitude). The relationship between β and A_{11} was presented in Section 5.7. For pure simulation, orientation index β instead of orientation tensor A_{11} is utilized to represent the re-orientation of fibers.*



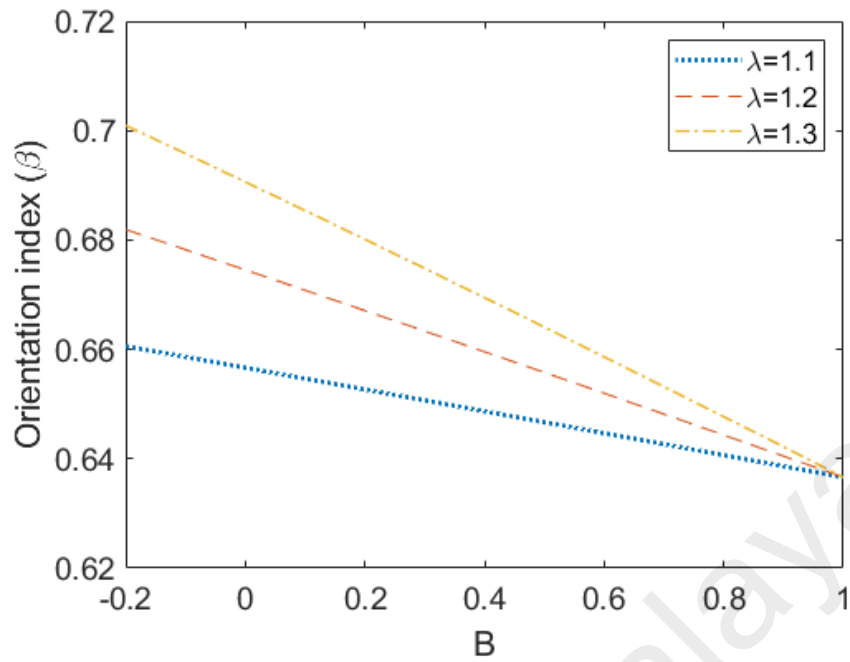
(a)



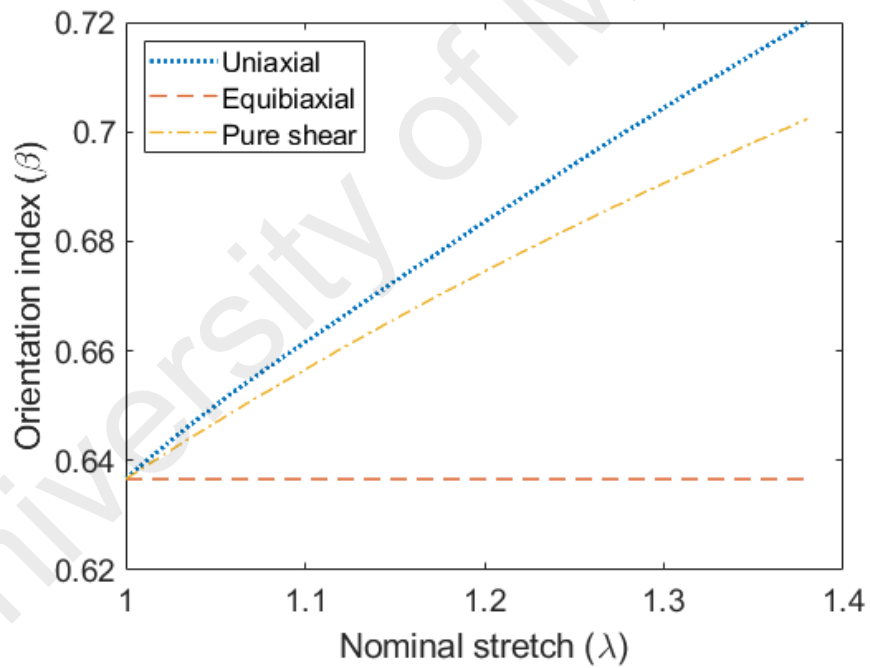
(b)

Figure 5.16: Simulation of (a) monotonic and (b) cyclic loading with increasing maximum stretch for planar extension.

From Figure 5.17 (a), it is observed that all three curves converged at $B = 1$, showing an orientation index of $\beta = 0.6366$ or $\beta = 2/\pi$. Recalling the values of biaxiality constant, $B = 1$ represents the case of equibiaxial extension. Thus, it is said that for the case of equibiaxial extension, the fiber orientation does not evolve with deformation due to the



(a)



(b)

Figure 5.17: (a) Effect of biaxiality at three different global stretch values ($\lambda = 1.1$, $\lambda = 1.2$ and $\lambda = 1.3$) and (b) evolution of orientation index with deformation.

equal stretching at two principal directions, i.e. \mathbf{e}_1 and \mathbf{e}_2 . This phenomenon is again validated in Figure 5.17 (b), where the orientation index β does not evolve with applied deformation for the case of equibiaxial extension. Subsequently, it is observed that fibers re-oriented more rapidly in the case of uniaxial extension as compared to pure shear.

Lastly, it is to note that the above orientation index was calculated using the assumption of affine motion, i.e. a fiber initially at \mathbf{N}^θ is mapped in the deformed state to \mathbf{FN}^θ . Further work is needed to investigate the validity of this assumption.

University of Malaya

CHAPTER 6: CONCLUSION AND FUTURE WORKS

6.1 Conclusion

The present thesis is concluded with reference to the objectives listed in Chapter 1.

1. To fabricate PVDF nanofibrous membranes by using electrospinning technique.

A total of six electrospun PVDF nanofibrous membranes were successfully fabricated by utilizing the electrospinning processing technique. The six PVDF membranes were produced utilizing two different polymer concentrations, i.e. 13 wt.% and 15 wt.% and three different voltages, i.e. 10 kV, 15 kV and 20 kV, by keeping all other electrospinning parameters constant. The purpose of fabricating a number of electrospun PVDF membranes through the manipulation of polymer concentration and voltage was to provide a suitable sample for further evaluations on the mechanical response as well as the fiber orientation of the randomly oriented electrospun PVDF membranes. Therefore, optimization of the electrospinning parameters was not discussed in the present work.

2. To characterize the surface morphology and mechanical response of electrospun nanofibrous membranes.

Results from surface morphology analysis suggested that the PVDF nanofibrous membrane fabricated from electrospinning parameters of 15 wt.% polymer concentration, 20 kV applied voltage, feed rate of 0.5 ml/h and capillary-collector distance of 150 mm produced the best combination of desired fiber diameter and with less bead defects among all the fabricated membranes. Subsequently, this sample of PVDF nanofibrous membrane was selected as the representative for the physical evaluation on undeformed and deformed membranes, mechanical characterization and fiber orientation analysis. Physical evaluation on undeformed and deformed specimens

showed that the pore diameter increases while fiber diameter decreases on inducing deformation on the electrospun PVDF membranes. Three types of mechanical loadings, i.e. monotonic tensile tests, cyclic loadings with increasing maximum strain and cyclic-relaxation tests were conducted on the representative sample of PVDF nanofibrous membrane. Monotonic tensile tests on specimens from two perpendicular orientation indicated that the material was initially isotropic in the plane. Whereas from cyclic loading test, the evolution of the Young's modulus indicating the existence of two competing phenomena: deformation-induced fiber re-orientation and deformation-induced fiber damage. Moreover, cyclic loading test with increasing maximum strain promoted strain hardening on the structure as the maximum strain increased. Further cyclic-relaxation test signified the time-dependent response of the structure through the analysis on stress-time curve. Finally, multiple-relaxation test provided further insight on the time-dependent response of the electrospun PVDF membranes. On the investigation of Poisson's ratio, the in-plane Poisson's ratio showed values that range from 1.9812 to 2.201, while the out-of-plane Poisson's ratio possessed values in the range of -1.084 to -1.5992. Meanwhile, the experimental results related to the fiber orientation distribution and the component of fiber orientation tensor (A_{11}) indicated that fibers re-orientated towards the direction of applied strain and the degree of fiber realignment increased as the induced strain increased.

3. To propose a phenomenological model to capture the observed mechanical response of electrospun nanofibrous membranes.

For the constitutive modeling of electrospun nanofibrous membranes, a simple phenomenological model with reduced number of material parameters was proposed to capture the macroscopic mechanical response of the randomly oriented electrospun nanofibrous membranes. Motivated by the experimental observations of electrospun

PVDF nanofibrous membrane, the description of material response was proposed at fiber-scale in order to describe individual fiber response and irreversible inter-fiber interactions using hyperelastic and large strain elasto-plastic frameworks respectively. However, the time-dependent response was ignored in the modeling part for the simplicity of the proposed phenomenological model. The macroscopic response of the membranes was subsequently obtained by integrating the fiber responses in all possible fiber orientations. By fitting the proposed model with the experimental results of cyclic loading test, six material parameters were identified where considerably good agreement was shown in the fitting. Subsequently, the proposed model was validated through the comparison of simulated monotonic uniaxial tensile loading with the experimental curves. Furthermore, biaxial stress states such as equibiaxial extension and pure shear were successfully simulated through the proposed model. Finally, by assuming an affine motion, the effect of biaxiality on the fiber re-orientation was explored, where it was shown that fibers reoriented more rapidly in the case of uniaxial extension as compared to pure shear, while no fiber re-orientation was observed for the case of equibiaxial extension.

6.2 Suggestions for future works

From the experimental point of view, further mechanical characterization such as fatigue testing can be investigated in the near future to provide greater insight into the mechanical response of electrospun nanofibrous membranes. Besides, the present work focuses on the investigation of electrospun nanofibrous membranes with randomly oriented fibers, fabricated through the use of stationary collector where structures were assumed to be initially isotropic in the plane. Thus, further mechanical characterizations can be conducted to probe the deformation-induced anisotropy of randomly oriented electrospun nanofibrous membranes, as well as to investigate the mechanical response of electrospun

nanofibrous membranes with aligned fibers, by fabricating through the use of rotating collector. Moreover, an experimental setup that consists of a tensile tester within a SEM can be developed to monitor the motion of fibers under tensile loading.

Meanwhile for the modeling part, the proposed constitutive model is based on the assumption of affine motion for simplicity. Thus, the relevance of non-affine motion can be investigated for further evaluation of the assumption. Moreover, the predictive capability of the present model is limited to time-independent responses. Therefore, further improvement on the model can be made by considering the time-dependent effect of the structure, as observed in the cyclic-relaxation and multiple-relaxation tests. The model could also be improved to account for the case of initially anisotropic materials by modifying the form of orientation distribution function. Lastly, some observed behaviors such as the non-linear hardening effect, the initial fiber curvature and the fiber buckling in compression can also be included in the future for the development of a more comprehensive model.

REFERENCES

- Advani, S. G., & Tucker, C. L. (1987). The use of tensors to describe and predict fiber orientation in short fiber composites. *Journal of Rheology*, 31(8), 751-784.
- Alagarasi, A. (2011). Introduction to nanomaterials. *National Center for Environmental Research*.
- Andriyana, A. (2006). *Définition d'une nouvelle grandeur prédictive pour la durée de vie en fatigue des matériaux élastomères* (Unpublished doctoral dissertation). École centrale de Nantes.
- Andriyana, A., Billon, N., & Silva, L. (2010). Mechanical response of a short fiber-reinforced thermoplastic: Experimental investigation and continuum mechanical modeling. *European Journal of Mechanics-A/Solids*, 29(6), 1065-1077.
- Arruda, E. M., & Boyce, M. C. (1993). A three-dimensional constitutive model for the large stretch behavior of rubber elastic materials. *Journal of the Mechanics and Physics of Solids*, 41(2), 389-412.
- Ashraf, M. R. (n.d.). Commodity polymers, engineering polymers and speciality polymers.
- Bais-Singh, S., & Goswami, B. C. (1995). Theoretical determination of the mechanical response of spun-bonded nonwovens. *Journal of the Textile Institute*, 86(2), 271-288.
- Baji, A., Mai, Y. W., Wong, S. C., Abtahi, M., & Chen, P. (2010). Electrospinning of polymer nanofibers: effects on oriented morphology, structures and tensile properties. *Composites science and technology*, 70(5), 703-718.
- Bao, L., Takatera, M., & Shinohara, A. (1997). Error evaluation on measuring the apparent poisson's ratios of textile fabrics by uniaxial tensile test. *Sen'i Gakkaishi*, 53(1), 20-26.
- Baumgarten, H. L., & Göttching, L. (1973). Triaxial deformation of paper under tensile load. *Proceedings of the 1973 The fundamental properties of paper related to its uses*.
- Beachley, V., & Wen, X. (2009). Effect of electrospinning parameters on the nanofiber diameter and length. *Materials Science and Engineering: C*, 29(3), 663-668.
- Benzinger, W. D., Parekh, B. S., & Eichelberger, J. L. (1980). High temperature ultrafiltration with kynar® poly(vinylidene fluoride) membranes. *Separation Science and Technology*, 15(4), 1193-1204.
- Boffito, M., Bernardi, E., Sartori, S., Ciardelli, G., & Sassi, M. P. (2015). A mechanical characterization of polymer scaffolds and films at the macroscale and nanoscale. *Journal of Biomedical Materials Research Part A*, 103(1), 162-169.
- Callister, W. D., & Rethwisch, D. G. (2011). *Materials science and engineering* (Vol. 5). John Wiley & Sons NY.

- Cao, G., & Wang, Y. (2004). *Nanostructures and nanomaterials: synthesis, properties, and applications*. World Scientific.
- Chalmers, J. M., & Meier, R. J. (2008). *Molecular characterization and analysis of polymers* (Vol. 53). Elsevier.
- Chanunpanich, N., Lee, B., & Byun, H. (2008). A study of electrospun pvdf on pet sheet. *Macromolecular research*, 16(3), 212-217.
- Choi, S. S., Lee, Y. S., Joo, C. W., Lee, S. G., Park, J. K., & Han, K. S. (2004). Electrospun pvdf nanofiber web as polymer electrolyte or separator. *Electrochimica Acta*, 50(2-3), 339-343.
- Choong, L. T., Mannarino, M. M., Basu, S., & Rutledge, G. C. (2013). Compressibility of electrospun fiber mats. *Journal of Materials Science*, 48(22), 7827-7836.
- Cozza, E. S., Monticelli, O., Marsano, E., & Cebe, P. (2013). On the electrospinning of pvdf: influence of the experimental conditions on the nanofiber properties. *Polymer International*, 62(1), 41-48.
- Curgul, S., Van Vliet, K. J., & Rutledge, G. C. (2007). Molecular dynamics simulation of size-dependent structural and thermal properties of polymer nanofibers. *Macromolecules*, 40(23), 8483-8489.
- Deitzel, J. M., Kleinmeyer, J., Harris, D. E. A., & Tan, N. C. B. (2001). The effect of processing variables on the morphology of electrospun nanofibers and textiles. *Polymer*, 42(1), 261-272.
- De Jong, S. (1977). An energy analysis of woven fabric mechanics by means of optimal-control theory. part ii: Pure-bending properties. *J. Textile Inst.*, 68, 362-369.
- Derch, R., Greiner, A., & Wendorff, J. H. (2004). Polymer nanofibers prepared by electrospinning. *Dekker encyclopedia of nanoscience and nanotechnology*, CRC, New York.
- De Vita, R., Leo, D. J., Woo, K. D., & Nah, C. (2006). A constitutive law for poly (butylene terephthalate) nanofibers mats. *Journal of applied polymer science*, 102(6), 5280-5283.
- Doshi, J., & Reneker, D. H. (1993). Electrospinning process and applications of electrospun fibers. In *Industry applications society annual meeting, 1993., conference record of the 1993 IEEE* (p. 1698-1703). IEEE.
- Dupaix, R. B., & Hosmer, J. E. D. (2010). Mechanical characterization and finite strain constitutive modeling of electrospun polycaprolactone under cyclic loading. *The International Journal of Structural Changes in Solids*, 2(1), 9-17.
- Ebewele, R. O. (2000). *Polymer science and technology*. CRC press.
- Ehrenstein, G. W., & Theriault, R. P. (2001). *Polymeric materials: Structure, properties. Applications*. Hanser. Cincinnati.

- Fong, H., Chun, I., & Reneker, D. H. (1999). Beaded nanofibers formed during electrospinning. *Polymer*, *40*(16), 4585-4592.
- Fried, J. R. (2014). *Polymer science and technology*. Pearson Education.
- Fung, Y. C. (1990). Biomechanical aspects of growth and tissue engineering. In *Biomechanics* (pp. 499–546). Springer.
- Gao, K., Hu, X., Dai, C., & Yi, T. (2006). Crystal structures of electrospun pvdf membranes and its separator application for rechargeable lithium metal cells. *Materials Science and Engineering: B*, *131*(1), 100-105.
- Gopal, R., Kaur, S., Ma, Z., Chan, C., Ramakrishna, S., & Matsuura, T. (2006). Electrospun nanofibrous filtration membrane. *Journal of Membrane Science*, *281*(1), 581-586.
- Greiner, A., & Wendorff, J. H. (2007). Electrospinning: a fascinating method for the preparation of ultrathin fibers. *Angewandte Chemie International Edition*, *46*(30), 5670-5703.
- Haghi, A. K., Pogliani, L., Torrens, F., Balköse, D., & Mukbaniani, O. V. (2017). *Applied chemistry and chemical engineering, volume 3: Interdisciplinary approaches to theory and modeling with applications*. CRC Press.
- He, F., Sarkar, M., Lau, S., Fan, J., & Chan, L. H. (2011). Preparation and characterization of porous poly (vinylidene fluoride-trifluoroethylene) copolymer membranes via electrospinning and further hot pressing. *Polymer Testing*, *30*(4), 436-441.
- Holzappel, G. A. (2000). *Nonlinear solid mechanics* (Vol. 24). Wiley Chichester.
- Holzwarth, J. M., & Ma, P. X. (2011). Biomimetic nanofibrous scaffolds for bone tissue engineering. *Biomaterials*, *32*(36), 9622-9629.
- Hu, J. J. (2015). Constitutive modeling of an electrospun tubular scaffold used for vascular tissue engineering. *Biomechanics and modeling in mechanobiology*, *14*(4), 897–913.
- Huang, Z. M., Zhang, Y. Z., Ramakrishna, S., & Lim, C. T. (2004). Electrospinning and mechanical characterization of gelatin nanofibers. *Polymer*, *45*(15), 5361-5368.
- Hwang, K., Kwon, B., & Byun, H. (2011). Preparation of pvdf nanofiber membranes by electrospinning and their use as secondary battery separators. *Journal of Membrane Science*, *378*(1–2), 111-116.
- Hwang, K. Y., Kim, S. D., Kim, Y. W., & Yu, W. R. (2010). Mechanical characterization of nanofibers using a nanomanipulator and atomic force microscope cantilever in a scanning electron microscope. *Polymer Testing*, *29*(3), 375-380.
- Inai, R., Kotaki, M., & Ramakrishna, S. (2005). Structure and properties of electrospun plla single nanofibres. *Nanotechnology*, *16*(2), 208.
- Jang, W. G., Hou, J., & Byun, H. S. (2011). Preparation and characterization of pvdf nanofiber ion exchange membrane for the pemfc application. *Desalination and Water*

Treatment, 34(1-3), 315-320.

Jearanaisilawong, P. (2008). *A continuum model for needlepunched nonwoven fabrics* (Unpublished doctoral dissertation). Massachusetts Institute of Technology.

King, M. J., Jearanaisilawong, P., & Socrate, S. (2005). A continuum constitutive model for the mechanical behavior of woven fabrics. *International Journal of Solids and Structures*, 42(13), 3867-3896.

Kodolov, V. I., Zaikov, G. E., & Haghi, A. K. (2014). *Nanostructures, nanomaterials, and nanotechnologies to nanoindustry*. CRC Press.

Laiarinandrasana, L., & Hochstetter, G. (2006). Fracture mechanics on pvdf polymeric material: specimen geometry effects. In *Fracture of nano and engineering materials and structures* (pp. 1143–1144). Springer.

Lanir, Y. T. (1983). Constitutive equations for fibrous connective tissues. *Journal of biomechanics*, 16(1), 1–12.

Leaf, G. A. V., & Kandil, K. H. (1980). 1—the initial load–extension behaviour of plain-woven fabrics. *Journal of the Textile Institute*, 71(1), 1–7.

Lee, C. H., Shin, H. J., Cho, I. H., Kang, Y.-M., Kim, I. A., Park, K.-D., & Shin, J.-W. (2005). Nanofiber alignment and direction of mechanical strain affect the ecm production of human acl fibroblast. *Biomaterials*, 26(11), 1261-1270.

Lee, S., & Obendorf, S. K. (2007). Use of electrospun nanofiber web for protective textile materials as barriers to liquid penetration. *Textile Research Journal*, 77(9), 696-702.

Li, Z., & Wang, C. (2013). *One-dimensional nanostructures: Electrospinning technique and unique nanofibers*. Springer Berlin Heidelberg.

Liao, Y., Wang, R., Tian, M., Qiu, C., & Fane, A. G. (2013). Fabrication of polyvinylidene fluoride (pvdf) nanofiber membranes by electro-spinning for direct contact membrane distillation. *Journal of Membrane Science*, 425, 30-39.

Lion, A. (1996). A constitutive model for carbon black filled rubber: experimental investigations and mathematical representation. *Continuum Mechanics and Thermodynamics*, 8(3), 153-169.

Liu, F., Hashim, N. A., Liu, Y., Abed, M. R. M., & Li, K. (2011). Progress in the production and modification of pvdf membranes. *Journal of Membrane Science*, 375(1–2), 1-27.

Mannarino, M. M., & Rutledge, G. C. (2012). Mechanical and tribological properties of electrospun pa 6 (3) t fiber mats. *Polymer*, 53(14), 3017–3025.

Mathew, G., Hong, J. P., Rhee, J. M., Lee, H. S., & Nah, C. (2005). Preparation and characterization of properties of electrospun poly (butylene terephthalate) nanofibers filled with carbon nanotubes. *Polymer testing*, 24(6), 712-717.

Meechaisue, C., Dubin, R., Supaphol, P., Hoven, V. P., & Kohn, J. (2006). Electrospun mat

- of tyrosine-derived polycarbonate fibers for potential use as tissue scaffolding material. *Journal of Biomaterials Science, Polymer Edition*, 17(9), 1039-1056.
- Megelski, S., Stephens, J. S., Chase, D. B., & Rabolt, J. F. (2002). Micro- and nanostructured surface morphology on electrospun polymer fibers. *Macromolecules*, 35(22), 8456-8466.
- Molnar, K., Vas, L. M., & Czigany, T. (2012). Determination of tensile strength of electrospun single nanofibers through modeling tensile behavior of the nanofibrous mat. *Composites Part B: Engineering*, 43(1), 15-21.
- Nadler, B., Papadopoulos, P., & Steigmann, D. J. (2006). Multiscale constitutive modeling and numerical simulation of fabric material. *International Journal of Solids and Structures*, 43(2), 206-221.
- Nerurkar, N. L., Elliott, D. M., & Mauck, R. L. (2007). Mechanics of oriented electrospun nanofibrous scaffolds for annulus fibrosus tissue engineering. *Journal of Orthopaedic Research*, 25(8), 1018-1028.
- Nimmo, J. R. (2004). Porosity and pore size distribution. *Encyclopedia of Soils in the Environment*, 3, 295-303.
- Pillay, V., Dott, C., Choonara, Y. E., Tyagi, C., Tomar, L., Kumar, P., ... Ndesendo, V. M. K. (2013). A review of the effect of processing variables on the fabrication of electrospun nanofibers for drug delivery applications. *Journal of Nanomaterials*, 2013, 22.
- Planas, J., Guinea, G. V., & Elices, M. (2007). Constitutive model for fiber-reinforced materials with deformable matrices. *Physical Review E*, 76(4), 041903.
- Raina, A., & Linder, C. (2014). A homogenization approach for nonwoven materials based on fiber undulations and reorientation. *Journal of the Mechanics and Physics of Solids*, 65, 12-34.
- Rezakhaniha, R., Agianniotis, A., Schrauwen, J. T. C., Griffa, A., Sage, D., Bouten, C. V. C., ... Stergiopoulos, N. (2012). Experimental investigation of collagen waviness and orientation in the arterial adventitia using confocal laser scanning microscopy. *Biomechanics and modeling in mechanobiology*, 11(3-4), 461-473.
- Ridruejo, A., González, C., & Llorca, J. (2011). Micromechanisms of deformation and fracture of polypropylene nonwoven fabrics. *International Journal of Solids and Structures*, 48(1), 153-162.
- Ridruejo, A., González, C., & Llorca, J. (2012). A constitutive model for the in-plane mechanical behavior of nonwoven fabrics. *International Journal of Solids and Structures*, 49(17), 2215-2229.
- Rizvi, M. S., Kumar, P., Katti, D. S., & Pal, A. (2012). Mathematical model of mechanical behavior of micro/nanofibrous materials designed for extracellular matrix substitutes. *Acta biomaterialia*, 8(11), 4111-4122.

- Runesson, K., Steinmann, P., Ekh, M., & Menzel, A. (2006). Constitutive modeling of engineering materials—theory and computation. *Volume I General Concepts and Inelasticity*.
- Schulgasser, K. (1983). The in-plane poisson ratio of paper. *Fibre Science and Technology*, 19(4), 297–309.
- Shim, V. P. W., Tan, V. B. C., & Tay, T. E. (1995). Modelling deformation and damage characteristics of woven fabric under small projectile impact. *International Journal of Impact Engineering*, 16(4), 585-605.
- Silberstein, M. N., Pai, C. L., Rutledge, G. C., & Boyce, M. C. (2012). Elastic–plastic behavior of non-woven fibrous mats. *Journal of the Mechanics and Physics of Solids*, 60(2), 295-318.
- Sill, T. J., & von Recum, H. A. (2008). Electrospinning: applications in drug delivery and tissue engineering. *Biomaterials*, 29(13), 1989-2006.
- Simo, J. C., & Hughes, T. J. R. (2006). *Computational inelasticity* (Vol. 7). Springer Science & Business Media.
- Society, R., & of Engineering, R. A. (2004). *Nanoscience and nanotechnologies: opportunities and uncertainties*. Royal Society and Royal Academy of Engineering London.
- Son, W. K., Youk, J. H., Lee, T. S., & Park, W. H. (2004). The effects of solution properties and polyelectrolyte on electrospinning of ultrafine poly (ethylene oxide) fibers. *Polymer*, 45(9), 2959-2966.
- Staudinger, H. (1920). Über polymerisation. *European Journal of Inorganic Chemistry*, 53(6), 1073–1085.
- Sun, H., Pan, N., & Postle, R. (2005). On the poisson's ratios of a woven fabric. *Composite Structures*, 68(4), 505–510.
- Szewczyk, W. (2008). Determination of poisson's ratio in the plane of the paper. *Fibres & Textiles in Eastern Europe*, 4, 117–120.
- Tan, E. P. S., Goh, C. N., Sow, C. H., & Lim, C. T. (2005). Tensile test of a single nanofiber using an atomic force microscope tip. *Applied Physics Letters*, 86(7), 073115.
- Tan, E. P. S., & Lim, C. T. (2004). Physical properties of a single polymeric nanofiber. *Applied Physics Letters*, 84(9), 1603–1605.
- Tan, E. P. S., & Lim, C. T. (2005). Nanoindentation study of nanofibers. *Applied Physics Letters*, 87(12), 123106.
- Tan, E. P. S., & Lim, C. T. (2006). Mechanical characterization of nanofibers—a review. *Composites Science and Technology*, 66(9), 1102-1111.
- Tan, E. P. S., Ng, S. Y., & Lim, C. T. (2005). Tensile testing of a single ultrafine polymeric fiber. *Biomaterials*, 26(13), 1453-1456.

- Tan, S. H., Inai, R., Kotaki, M., & Ramakrishna, S. (2005). Systematic parameter study for ultra-fine fiber fabrication via electrospinning process. *Polymer*, 46(16), 6128-6134.
- Taylor, G. (1964). Disintegration of water drops in an electric field. In *Proceedings of the royal society of london a: Mathematical, physical and engineering sciences* (Vol. 280, p. 383-397). The Royal Society.
- Taylor, G. (1969). Electrically driven jets. In *Proceedings of the royal society of london a: Mathematical, physical and engineering sciences* (Vol. 313, p. 453-475). The Royal Society.
- Tripatanasuwan, S., Zhong, Z., & Reneker, D. H. (2007). Effect of evaporation and solidification of the charged jet in electrospinning of poly (ethylene oxide) aqueous solution. *Polymer*, 48(19), 5742-5746.
- Venugopal, J., & Ramakrishna, S. (2005). Applications of polymer nanofibers in biomedicine and biotechnology. *Applied biochemistry and biotechnology*, 125(3), 147-157.
- Venugopal, J., Zhang, Y. Z., & Ramakrishna, S. (2004). Electrospun nanofibres: biomedical applications. *Proceedings of the Institution of Mechanical Engineers, Part N: Journal of Nanoengineering and Nanosystems*, 218(1), 35-45.
- Verron, E. (2015). Questioning numerical integration methods for microsphere (and microplane) constitutive equations. *Mechanics of Materials*, 89, 216-228.
- Wan, L. Y., Wang, H., Gao, W., & Ko, F. (2015). An analysis of the tensile properties of nanofiber mats. *Polymer*, 73, 62-67.
- Wang, M., Jin, H. J., Kaplan, D. L., & Rutledge, G. C. (2004). Mechanical properties of electrospun silk fibers. *Macromolecules*, 37(18), 6856-6864.
- Wong, S. C., Baji, A., & Leng, S. (2008). Effect of fiber diameter on tensile properties of electrospun poly (ϵ -caprolactone). *Polymer*, 49(21), 4713-4722.
- Yang, Q., Li, Z., Hong, Y., Zhao, Y., Qiu, S., Wang, C. E., & Wei, Y. (2004). Influence of solvents on the formation of ultrathin uniform poly (vinyl pyrrolidone) nanofibers with electrospinning. *Journal of Polymer Science Part B: Polymer Physics*, 42(20), 3721-3726.
- Yu, M. F., Lourie, O., Dyer, M. J., Moloni, K., Kelly, T. F., & Ruoff, R. S. (2000). Strength and breaking mechanism of multiwalled carbon nanotubes under tensile load. *Science*, 287(5453), 637-640.
- Yuan, B., Liu, Q. F., Lin, C., & Chen, X. F. (2011). Modeling the elasticity of oriented electrospun nano-fibrous scaffold. In *Key engineering materials* (Vol. 467, pp. 1241-1244).
- Yuan, X., Zhang, Y., Dong, C., & Sheng, J. (2004). Morphology of ultrafine polysulfone fibers prepared by electrospinning. *Polymer International*, 53(11), 1704-1710.

Zhao, Z., Li, J., Yuan, X., Li, X., Zhang, Y., & Sheng, J. (2005). Preparation and properties of electrospun poly(vinylidene fluoride) membranes. *Journal of Applied Polymer Science*, 97(2), 466-474.

Zong, X., Kim, K., Fang, D., Ran, S., Hsiao, B. S., & Chu, B. (2002). Structure and process relationship of electrospun bioabsorbable nanofiber membranes. *Polymer*, 43(16), 4403-4412.

University of Malaya

LIST OF PUBLICATIONS AND PAPERS PRESENTED

Academic Journals

1. Wong, D., Andriyana, A., Ang, B. C., & Verron, E. (2016). Surface morphology and mechanical response of randomly oriented electrospun nanofibrous membrane. *Polymer Testing*, 53, 108-115.
2. Wong, D., Andriyana, A., Ang, B. C., Chan, Y. R., Lee, J. J. L., Afifi, A. M., & Verron, E. (2016). Surface morphology analysis and mechanical characterization of electrospun nanofibrous structure. In *Key Engineering Materials* (Vol. 701, pp. 89-93). Trans Tech Publications.
3. Wong, D., Verron, E., Andriyana, A., & Ang, B. C. (2018). Constitutive modeling of randomly oriented electrospun nanofibrous membranes. *Continuum Mechanics and Thermodynamics*. (Submitted for Publication).
4. Wong, D., Andriyana, A., Ang, B. C., Lee, J. J. L., Verron, E., & Elma, M. (2018). Poisson's ratio and volume change accompanying deformation of randomly oriented electrospun nanofibrous membranes. *Mechanics of Advanced Materials and Structures*. (Submitted for Publication).

Conferences

1. Wong, D., Andriyana, A., Ang, B. C., Afifi, A. M. & Verron, E. (2015) Characterization of the mechanical response of electrospun nanofibrous PVDF membrane. *4th International Nanofibers Symposium*. 15-16 October 2015. Tokyo, Japan.
2. Wong, D., Andriyana, A., Ang, B. C., Chan, Y. R., Lee, J. J. L., Afifi, A. M., & Verron, E. (2015). Surface morphology analysis and mechanical characterization of electrospun nanofibrous structure. Proceedings of *International Conference on the Science and Engineering of Materials (ICoSEM)*. 16-18 November 2015. Kuala Lumpur, Malaysia.
3. Wong, D., Andriyana, A., Ang, B. C., Afifi, A. M., & Verron, E. (2016). Electrospinning and mechanical response of randomly oriented polymeric nanofibrous membranes. *The 10th International Conference on the Mechanics of Time Dependent Materials (MTDM)*. 18-20 May 2016. Paris, France.
4. Wong, D., Andriyana, A., Ang, B. C., & Verron, E. (2016). Mechanical response of randomly oriented electrospun nanofibrous membrane. *Elastomères 2016: 4ème Journée Thématique sur la Caractérisation Mécanique des Elastomères*. 27 May 2016. Marseille, France.
5. Wong, D., Andriyana, A., Ang, B. C. & Verron, E. (2018). Mechanical response of randomly oriented nanofibrous membranes: experimental characterization and constitutive modeling. *Electrospin2018 International Conference*. 16-18 January 2018. Stellenbosch, South Africa.